IN-02
108638

P. 63

Direct Simulation of High-Speed Mixing Layers

H. S. Mukunda,
B. Sekar,
M. H. Carpenter,
J. Philip Drummond,
and Ajay Kumar

NASA

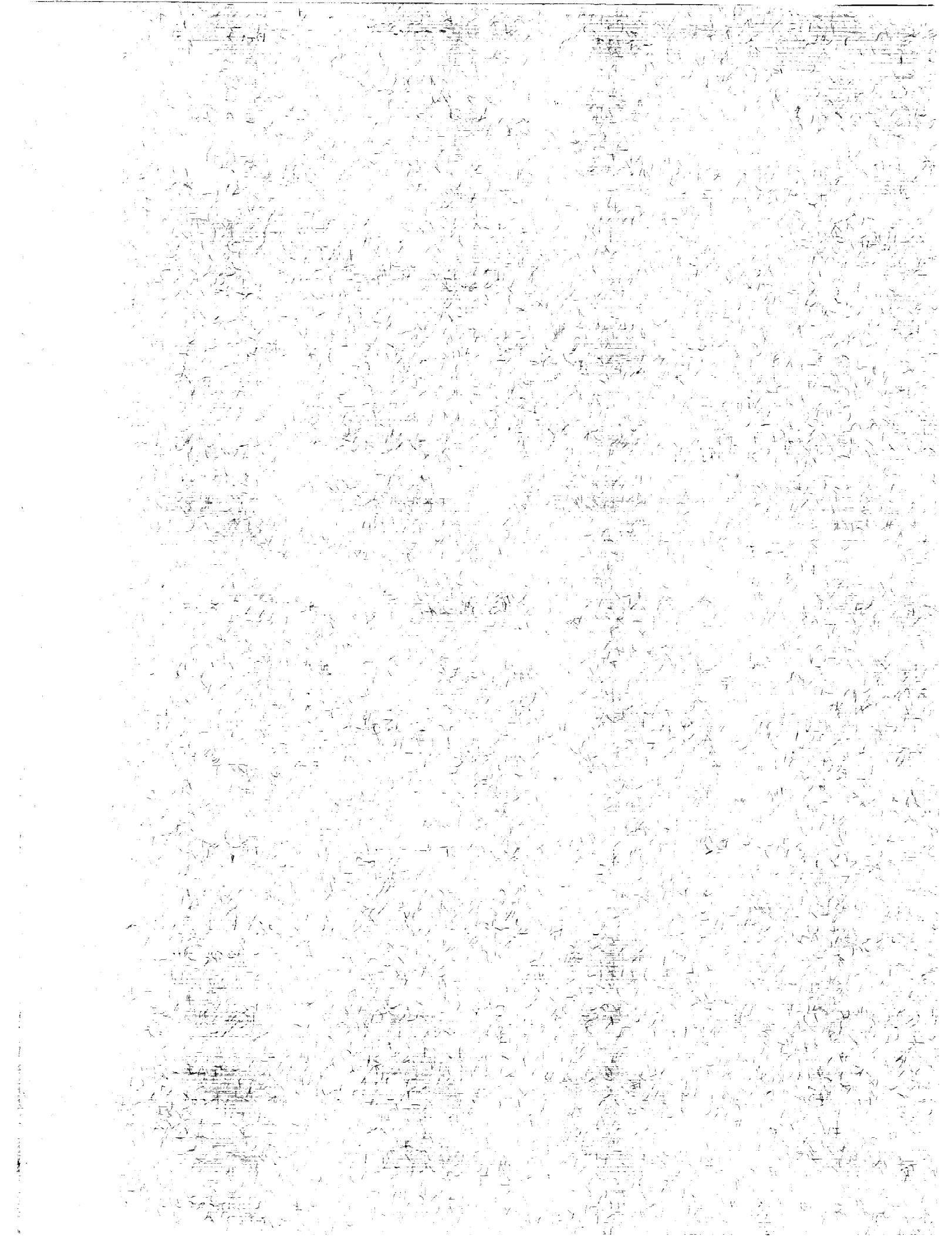# Direct Simulation of High-Speed Mixing Layers

H. S. Mukunda
Langley Research Center
Hampton, Virginia

B. Sekar
General Electric Research Center
Cincinnati, Ohio

M. H. Carpenter,
J. Philip Drummond,
and Ajay Kumar
Langley Research Center
Hampton, Virginia

Summary

This computational study is an exploration of nonreacting high-speed mixing layers. The computations are made with a code based on an accurate higher order algorithm and with sufficient grid points to resolve all relevant scales. In each case, the free-stream disturbance is introduced, and the calculations are run until a statistical steady state is reached (2 or 3 sweeps, based on axial distance and convective speed). Then, 400 to 600 time samples of the flow, at equal time intervals, are generated to obtain statistical properties of the flow.

The studies are conducted at two convective Mach numbers, three free-stream turbulence intensities, three Reynolds numbers, and two types of initial profiles—hyperbolic tangent (tanh) and boundary layer. These profiles are used to interpret the effects of corresponding parameters.

The boundary-layer profile leads to predictions of transition processes much better than the tanh profile at disturbance intensities comparable to those in wind tunnels. The transition Reynolds number predicted is about 0.18×10^6 and compares well with experimental data. The spacing between the vortical structure normalized by the boundary-layer thickness is about 3.5 (boundary-layer case) and 10 (tanh case), whereas the observed values range from 1.5 to 2.5. The deduction of the growth-rate data from the plots of growth versus the streamwise coordinate is, in part, affected by the nature of free-stream disturbance introduced and the regions of slight negative growth. Nevertheless, careful extraction of the growth-rate information and comparison with the experimental data of Papamoschou show that this comparison is moderately good. The study of the location of the disturbance shows that the growth of the layer is suppressed if the shear-layer region is excluded from the disturbance field. Calculations with the boundary-layer case with no imposed disturbance show that the shear layer selectively amplifies the noise at a Strouhal number (based on momentum thickness) of 0.007. This result can be used in practice to excite the shear layer toward early transition. Studies of dependence on Reynolds number show that the effects are negligible, and this may be caused by the dominant inviscid structure of the flow field.

Introduction

High-speed mixing layers have received significant attention in the past 5 years because of the potential applications in hypersonic plane scramjet combustors, where the combustion process is supersonic.

Recent experimental results (ref. 1) indicate that the growth rates of high-speed layers in relation to those of incompressible shear layers are much smaller—by a factor of 4 to 5. This reduction implies that much longer lengths are needed to achieve the same level of mixing and combustion efficiency. This longer length is obviously undesirable from a technological point of view. Consequently, considerable attention is being paid to the mixing phenomenon in supersonic mixing layers—both nonreacting and chemically reacting.

Studies of stability of mixing layers (refs. 2 and 3) and direct simulation of temporally and spatially developing mixing layers (refs. 4 and 5) are the theoretical and computational approaches made to understanding the behavior of the mixing layers. Experimental studies of the high-speed mixing layers are difficult, and there are not many such studies. These mixing layers have not been sufficiently explored for the distribution of mean and fluctuating quantities with nonintrusive diagnostic tools. The only reliable sources of information available are the growth rates measured from pitot traverses, Schlieren pictures, and mean velocity measurements. Some efforts at modeling the mixing process have been made, but a more precise understanding of the flow must be obtained before the modeling efforts are considered valid.

In light of this scenario, direct numerical simulation of the shear layers becomes an important tool for understanding the mixing process. The classical question of resolution of scales at high Reynolds numbers limits the exploration to relatively low Reynolds numbers ($\approx 1 \times 10^4$) based on shear-layer thickness and mean velocity at the inflow plane). But this range is not much below the range of practical relevance or importance. Thus, it should be possible to perform these calculations and to make deductions of relevance and some importance to the behavior of mixing layers. Initially, studies will be limited to two-dimensional simulations. While there is the capability to make three-dimensional simulations, it is important to understand two-dimensional simulations before embarking on three-dimensional calculations. In recent times, a few groups (refs. 4 and 6) have made direct numerical simulations of shear layers, and much has been uncovered. The present contribution is complementary in some aspects and presents new results on many aspects.

Symbols

a	speed of sound
b.l.	boundary layer
c	constant

f_i	mass fraction of species i
h	enthalpy
k	turbulent kinetic energy
M	Mach number
M_c	convective Mach number
p	pressure
R	Reynolds number
R_T	transition Reynolds number
rms	root mean square
St	Strouhal number
T	temperature
t	time
tanh	hyperbolic tangent
U_p, U_∞	primary stream velocity
U_s, U_∞	secondary stream velocity
u	streamwise velocity
u_c	convective velocity
u_d	disturbance in streamwise direction
u_m	streamwise mean velocity
v	transverse velocity
v_d	disturbance in cross-stream direction
x	streamwise coordinate
x_m	maximum extent of x field
x_T	transition distance
y	transverse coordinate
y_m	maximum extent of y field
γ	ratio of specific heats
δ	mixing-layer thickness
δ'	growth rate
η	Kolmogorov scale
θ	momentum defect thickness
μ	laminar viscosity
ρ	density
Ω	vorticity

Subscripts:

p	primary
s	secondary

Previous Studies

Experimental

Table 1 contains a list of references and some brief details of the experimental work discussed in them. This table has been constructed to determine which experiments can be used for comparison with the results of the simulation. Figure 1 shows the experimental design used by these authors to obtain their results.

Reference 7 is a critical summary of the data of many early studies on both subsonic and supersonic shear layers. The data of references 8 and 9 and their nondimensional growth rate as a function of Mach number are important. The growth rate is normalized by that under incompressible conditions. It is apparent from reference 10 that the incompressible mixing-layer growth rate is uncertain to a significant extent (a factor of 1.8). Therefore, the quality of the results of nondimensional growth rate versus M is not assured, even though the primary result that mixing-layer growth rate decreases with convective Mach number M_c is unquestioned.

Experiments have been conducted on mixing layers (ref. 11) by using a splitter-plate configuration (fig. 1(a)). Measurements of mean velocity profile and transition have been made for two configurations at $M_c = 0.325$ and 0.515 (table 1), and the pressures across the mixing layer are not the same. In one case, they are different by a factor of 1.3. Transition is measured in the following ways: (1) point of change in slope of the plot of growth versus distance, (2) examination of Schlieren pictures, and (3) point of decay of the spectral intensity of the dominant frequencies in the free shear layer as measured by a hot-film probe. The transition locations, as measured by these criteria, are not necessarily the same—they vary by about 35 to 45 mm. The transition distance normalized by initial momentum thickness is about 165 to 300θ, depending on the flow conditions and the transition Reynolds number based on mean properties (and mean velocity), which is about $2.0 \times 10^5 \pm 0.3 \times 10^5$.

The experiments of reference 12 are instructive in many ways. Though the study is limited to a single speed and the geometry used is not pertinent to the two-stream mixing considered here, it gives an appreciation of the free-stream turbulence and the peak turbulence intensity inside the shear layer. The measured free-stream turbulence is about 0.2 percent for velocity fluctuations and 0.1 percent for pressure fluctuations. The peak turbulence intensity increases to 6 percent in the downstream region of the shear layer. This study also presents the velocity spectra

that can be used for detailed comparison. The apparatus used by these spectra is shown in figure 1(c). The injection from the bottom wall helps balance the pressure across the shear layer.

Papamoschou's work (refs. 1 and 13 to 15) is by far the most referenced work, essentially because of a systematic effort to evolve appropriate parameters for compressibility effects and to determine the effect of compressibility on mixing (growth rate of the mixing layer). There were previous studies (both experimental and linear stability) on the subject, but the status of understanding was not consolidated until his work clarified issues and reinforced the implications of previous work on stability (ref. 2). The principal result he obtained was the variation of the nondimensional growth rate with convective Mach number. Following the work of Roshko and others, the dynamics of the mixing layer is argued to be affected by the speed of large-scale structures relative to the speed of one of the streams. The ratio of this speed to the average acoustic speed is the convective Mach number M_c. The growth rate normalized by that for incompressible conditions decreases by a factor of about 4 to 5 when M_c increases to 2. In these experiments, Papamoschou used nitrogen, argon, and helium as test gases in a splitter-plate configuration (fig. 1(b)). Understandably, the test durations were short, typically 1 to 2 sec, and the measurements consisted of pitot surveys across the mixing layer. The free-stream turbulence effects are only indirectly inferred from wall pressure measurements. One of the other details measured, but not published, is the difference in the static pressure of the two streams. This difference may well be small, but it adds to the wave processes and, in a disturbed environment, may affect transition.

Some preliminary measurements of a shear layer of a single fluid with two streams across a splitter plate are reported in reference 16. A single measurement of growth rate and velocity profile has been reported, as well as a mean turbulence velocity of 5 percent in the mixing layer. Reference 16 also indicates from the measurement of laser doppler velocimetry (LDV) that the wave reflections from the walls can cause fluctuations of flow velocities as high as 4 percent.

Some experiments of supersonic shear layer have been presented in reference 17. In this setup, the shear layer begins from a backward-facing step, and the flow structure in the downstream zone is altered by inserting a ramp (fig. 1(d)). The ramp provides a recirculation zone at near-zero speeds and helps to maintain a smooth shear layer. The growth rates from these experiments, with the incoming stream

deliberately made turbulent, are plotted along with the previous data to reinstate the conclusion regarding the reduced growth rate at supersonic conditions (in terms of M_c). Transition experiments have been conducted recently on a similar setup (ref. 18), but the test section was made disturbance free to a large extent. Measurements of transition Reynolds number show values from 3.63×10^5 to 5.3×10^5.

It is clear from the preceding discussion that (1) the various experimenters have used different apparatus for creating a mixing layer, (2) the measurements of the quality of the incoming stream are not complete in most cases, and (3) the mixing layers are subject to disturbance, acoustic and otherwise, at a magnitude upward of 0.2 percent, and a pressure differential across the layer of 1 to 1.3 in some instances. Yet, the growth rates of the layer from the work of most investigators, possibly in the turbulent range, are put on the same plot, and evidence of these being nearly the same qualitatively and quantitatively is presented (ref. 13). If these are true, then the asymptotic growth rate is relatively independent of tunnel characteristics and the disturbance environment. This aspect needs confirmation through systematic experimental study in which the incoming disturbance field is measured along with the features related to growth rate.

Computational

The efforts to model the flow, particularly to explain the reduced growth rate, are recent. These efforts have been related to stability, direct simulation, and a correlation of both. References 3 and 5 show that, at high speeds, the peak amplitudes of the unstable waves decrease with increasing M_c. Also, at high values of M_c, the three-dimensional oblique disturbances tend to grow more than the two-dimensional waves. This reduced amplification of the disturbances may be responsible for the delayed growth (in terms of distance from the edge of the splitter plate) and, in general, the inability of the flow to sustain the growth of disturbances.

Direct simulation of mixing layers has been conducted in reference 6 for supersonic mixing layers and in reference 19 for incompressible mixing layers. A high-order finite-difference scheme is coupled with fine-resolution grids to capture the important scales of the transport within the mixing layer in reference 6. The computations are aimed at establishing the importance of M_c and elucidating the causes for reduced mixing at high Mach numbers. The computations use tanh profiles and sufficiently large disturbances on the cross-stream velocity at the inflow station. The inflow disturbance magnitude is as high

3

as 5 percent. While some conclusions are not affected by this unnaturally large forcing, others are. For instance, the mixing-layer thickness versus axial distance shows a linear growth that tends, asymptotically, to zero growth. This result has no parallel in reality and is left unexplained. It is concluded from the present simulation, as well as from reference 19, that this result could be one of the effects of forcing.

The results for large Mach numbers indicate the presence of thin shocks called eddy shocklets. The reduced mixing at high Mach numbers has been related to the change in balance of terms involving baroclinic and compressibility terms in the velocity equation. Arguments of this nature were made in the temporal simulations of reference 20; these arguments indicate that baroclinic torque resulting from compressibility causes distribution of vorticity; the diffusion of the vorticity over a wider region results in weaker vortex roll-up and slower growth.

Reference 19 contains numerical simulations on incompressible mixing layers. The spread rate has nonmonotonic behavior with distance for specific cases, and this is related to the phase relationships between forcing and the pairing processes. This behavior is also related to the change in sign of the Reynolds number stress. Specifically, in regions where the spread rate decreases or remains nearly constant with distance, the energy is transferred from large-scale structures to the mean flow.

Reference 10, a review of free shear-layer mixing, addresses several relevant issues. Many aspects of this paper are for subsonic flows. The incompressible shear-layer growth rate is expressed as

$$\frac{\delta_0}{x} = \delta_0' = c_\delta \left(\frac{1 - r}{1 + r} \right) \tag{1}$$

where c_δ is a constant, possibly independent of velocity ratio r and/or the density ratio s. Based on cumulative experimental evidence, it is concluded that c_δ varies between 0.25 and 0.45. The large difference is still unaccounted for. Experimental evidence from incompressible flows is presented to indicate that the growth rate is a strong function of Reynolds number in a mixing layer.

The growth-rate dependence on Reynolds number seems to be a subject of some controversy. Papamoschou discusses this question in reference 13; he does not take a firm position, but indicates that he ignores the effect of Reynolds number. The reason that the large dependence on Reynolds number appears difficult to accept is that the mixing-layer phenomenon, particularly in the early part, is largely

inviscid. Hence, one would expect weak Reynolds number dependence at best.

The present work addresses the question of Reynolds number dependence by changing the Reynolds number through alterations of pressure rather than velocity. This approach has been discussed by Dimotakis (ref. 10), and it is one of the cleanest ways of changing the Reynolds number without altering other aspects of the flow. For example, changes of velocity also alter the initial boundary-layer profiles and have influences which have not been evaluated until now. One of the aims of this work is to treat this aspect as well.

Outline of Present Work

The present work is a direct simulation of mixing layers with different reactive fluids in the two adjoining streams. They are chosen so as to form a set for reactive studies as well. The first part of the work discusses the methodology for analyzing and interpreting the results of computation. The questions concerning grid resolution and boundary effects are discussed subsequently. The results of effects of free-stream disturbance on the growth of the shear layer at two different values of M_c are then brought out; both tanh and boundary layer, like initial profiles, are discussed. The various aspects—growth rates of vorticity, velocity, mass fraction, and density; vorticity plots and variation of turbulence quantities through the flow field; and time and space spectra of the fluctuations—are examined to obtain insight into the behavior of the mixing layer. The cases considered in the present work are shown in table 2. The choice of the two cases is aimed at making calculations, one at low M_c and another at a relatively high value. For the two cases considered, $M_c = 0.38$ and 0.76. A fuel and oxidizer system was chosen instead of single fluid system to enable computations with reaction as well (not reported herein). The temperature of both streams is held the same, so as not to additionally introduce a parameter through temperature. The temperature for the present test is 2000 K, as it is representative of inflow conditions in a supersonic combustor of a hypersonic cruise vehicle. Table 2 shows that the specific-heat ratio γ is nearly the same for both streams, $\frac{\gamma_{fuel}}{\gamma_{air}} = 1.0133$. This similarity is because of the high temperature of the stream and because the molecules involved are diatomic in nature.

The inflow-plane pressure is the same on both sides of the mixing layer at 0.101325 MPa (1 atm). Changes in Reynolds number are made by changing the pressure above and below the nominal value by a factor of 2. The convective properties are calculated

from

$$M_c = \frac{\left(M_p - M_s\sqrt{\frac{\rho_p\gamma_s}{\rho_s\gamma_p}}\right)}{\left(\frac{\gamma_s}{\gamma_p}\right)^{\frac{1}{4}}\left(1 + \sqrt{\frac{\rho_p}{\rho_s}}\right)} \quad (2)$$

and

$$U_c = \frac{\sqrt{\rho_p}U_p + \sqrt{\rho_s}U_s}{\left(\sqrt{\rho_p} + \sqrt{\rho_s}\right)} \quad (3)$$

These are the definitions presented in reference 14. They use the geometric average of the values of M_c on the primary p and secondary s sides. The primary side is defined as the one with the higher Mach number, no matter what the speed. In equation (2), γ has little impact. If we ignore the γ terms, then equation (2) reduces to

$$M_c = \frac{\sqrt{\rho_s}M_p - \sqrt{\rho_p}M_s}{\sqrt{\rho_p} + \sqrt{\rho_s}} \quad (4)$$

As discussed previously, Papamoschou's definition of M_c (ref. 13) is

$$M_c = \frac{U_p - U_s}{a_p + a_s} \quad (5)$$

Equation (2) reduces to the above result if we recognize that $a = \sqrt{\gamma p/\rho}$, and p and γ are the same for the two streams. The initial profiles are chosen as a tanh profile as follows:

$$u_m = \frac{1}{2}\left[(U_\infty + U_{-\infty}) + (U_\infty - U_{-\infty})\tanh ky\right] \quad (6)$$

The constant k is chosen as 1800 m^{-1}, so that the effective boundary-layer thickness, based on a 99-percent free-stream velocity criterion, is about 2 mm. For other numerical experiments, boundary-layer profiles are given by

$$u_m = U_\infty\left[1 - \exp\left(-k_1 y\right)\right] \qquad (y \geq y_m/2) \quad (7)$$

and

$$u_m = U_{-\infty}\left[1 - \exp\left(-k_1 y\right)\right] \qquad (y \leq y_m/2) \quad (8)$$

The constant k_1 is chosen as 4000 m^{-1}. The effective boundary-layer thickness on each side is about 1 mm. This profile is intended to simulate the normally obtained experimental conditions.

Table 3 shows the nondimensional parameters relevant to the cases considered. Several instructive features can be derived from tables 2 and 3. The velocity of the airstream is lower than that of the fuel for $M_c = 0.38$, but is much higher for $M_c = 0.76$. The momentum ratios shown in table 3 indicate that the momenta are balanced for $M_c = 0.38$ but are greatly in favor of the airstream for $M_c = 0.76$. The shear layer therefore remains roughly in alignment with the central axis in the first case, but bends over toward the fuel side in the second case. The implications for the computations are that the grid has to be well resolved, even in the outer regions, if the details are to be captured in the second case, or a twisted stretched grid must be used. In fact, this problem can be so serious that reactive flow computations do give considerable difficulty in the second case unless one of these strategies is adopted.

The second part of the work concerns the layer thicknesses. The thicknesses, based on 99-percent free-stream velocity, are about 1 mm on each side of the splitter plate. The momentum defect thicknesses θ for the tanh and boundary-layer profiles are very different from each other. In the tanh case, it is about 1.54 mm, and in the boundary-layer case, it is about 0.102 mm. This large difference implies that for the same streamwise grid length (e.g., 100 mm), only about 64 momentum thicknesses can be covered with the tanh profile, but about 1000 momentum thicknesses can be covered with the boundary-layer profile. For small free-stream disturbance levels consistent with experiments, no transition should be expected for the tanh case, but significant transition should be expected for the boundary-layer case. This situation can be altered if a free-stream condition of high turbulence intensity is imposed. If the transition is caused early enough, the asymptotic growth rate from this calculation would be representative of turbulent boundary-layer growth. The Reynolds number based on boundary-layer thickness is about 3.5×10^3 to 1.2×10^4 for the two Mach number cases. Based on the convective speed, momentum thickness, average density, and viscosity, then $R = 360$ to 550. If the reference speed is changed to the difference in speeds between the two streams, then $R = 250$ to 400. This last quantity is brought out because the difference in velocities is used by some workers for normalization purposes (ref. 6). These values are low enough that the direct simulation approach with the current-day computational aids is expected to lead to realistic results.

For disturbances to be introduced with the inflow profiles, several numerical experiments have been conducted. The disturbance function is chosen as

$$u_d = (U_\infty - U_{-\infty})\sum_{i=1}^{3} c_i \sin \omega_i t \quad (9)$$

5

$$v_d = (U_\infty - U_{-\infty}) \sum_{i=1}^{3} d_i \sin \omega_i t \qquad (10)$$

The velocity variation with y at $x = 0$ is then given by $u = u_m + u_d$ and $v = v_d$. In most cases, $c_2 = c_3 = 0$, $\omega_1 = 100$ kHz, $c_1 = 0.04$, $d_1 = 0.04$, $d_2 = 0.02$, $d_3 = 0.01$, $\omega_2 = 200$ kHz, and $\omega_3 = 300$ kHz.

In a few preliminary runs made with no inflow disturbance, the layer grew very little to about 100 mm. There was only a trace of growth toward the end. The time-sampled data at this plane were subjected to spectral analysis, and the frequencies, with relatively large amplitudes, were chosen and used in equations (9) and (10). The choice of the amplitudes is arbitrary and is made to ensure that the rms values of the fluctuations are of a required magnitude. The above disturbances (u_d, v_d) are introduced either into a specific region of about 4 mm or over the entire region. In some experiments, the disturbances are restricted to the fuel or oxidizer region only. These calculations were performed to observe the sensitivity of the mixing layer to the location of the disturbances.

Code and Algorithms

The code used in the present calculations is the SPARK combustion code developed at Langley Research Center over the past 4 years. It solves the Navier-Stokes equations, including energy and species conservation. The models chosen to evaluate viscosity, thermal conduction, and mass diffusion allow for a mixture of perfect gases. In the first version, the code used a second-order spatially and temporally accurate, two-step explicit MacCormack scheme. (See ref. 21.) Subsequently, it has been modified to include a variety of higher order spatial algorithms, including linear and compact algorithms (fourth and sixth order) and various upwind algorithms (third and fifth order). A brief description of the algorithms is provided in the appendix. Based on the supersonic streamwise characteristics of the mixing layer, a third-order, upwind-biased algorithm is used for the streamwise direction. A fourth-order, central-difference algorithm (ref. 22) is used in the cross-stream direction. The temporal accuracy is still second order. This choice represents a compromise between the accuracy of higher order numerical algorithms and the robustness and efficiency of lower order methods.

Boundary Conditions

The problem is cast in the x-y coordinates, such that the flow is oriented along the x-axis. The two streams extend from $y = 0$ to $y_m/2$ and $y_m/2$ to y_m, where y_m is the maximum extent of y. In the streamwise directions, the boundary conditions at $x = 0$ are the set values of u, v, p, T, and f_i, since the inflow is supersonic. The fluctuations, when introduced, are only in u and v. In a few experiments, fluctuations in p are also set. At the supersonic outflow plane $x = x_m$, first-order extrapolation of the primitive variables is used.

At $y = 0$ and y_m, the gradient $\frac{\partial(\text{property})}{\partial y} = 0$ is set. To ensure that the boundaries are far enough for this condition to be valid, the outer regions are chosen as 15 times the initial boundary-layer thickness. Therefore, $y_m = 30$ mm. A few numerical studies have been conducted with $y_m = 50$ mm. In one case at $M_c = 0.76$, doubts were raised as to whether the results were affected by the boundary. In this case, the boundary line is set at $y_m = 100$ mm. In all cases, the results obtained at $y_m = 30$ mm were reproducible and, to this extent, seem satisfactory.

Choice of Grids

It is intended that most scales of importance be captured in the calculations. Numerical resolution of the large-scale vortical structures presents no problem. However, the relatively fine scales at which dissipation through viscosity occurs need fine grids for capture. The Kolmogorov scale, which describes the fine scales, is related to the large scale (integral scale) as follows:

$$\frac{\eta}{\delta} = CR^{-\frac{3}{4}} \qquad (11)$$

where R is the Reynolds number based on a characteristic thickness. The Reynolds number of the flow with the initial boundary-layer thickness as the relevant scale varies from 3.5×10^3 to 1.2×10^4 for the problems treated. In the downstream region, where the shear-layer thickness is larger, Reynolds number goes up to 1.5×10^4. The constant C is to be estimated. The balance of dissipation and production is used in reference 23 to estimate the constant as typically 2.5 for incompressible flows. Recognizing the fact that in compressible flows the disturbances tend to have much lower growth rates—typically 2 to 3 times smaller than in incompressible flows—and that the asymptotic structure retains this effect, the constant is between 5 and 7. For a typical extent of growth estimated from known data—$\delta = 10$ mm and $R = 1.0 \times 10^4$—$\eta = 0.056$ mm. The smallest size of the computational domain is 0.025 mm. The stretching of the grid makes the grid size increase to 0.4 mm at a distance of 10 mm from the central line. This increase does not ensure that all the scales will be captured, as calculated in reference 17, but it

6

does ensure that most scales of importance are captured. Since this is an important issue, the justification for the choice of the step size is not limited to this argument. The spectra obtained from two different fine grids are compared to provide the necessary justification.

The number of grid points used in the y direction varies from 101 to 176. Many results obtained here are for 151 grid points over a region of 30 mm. A grid compression factor of 10.0 allows the region of 10 mm to be covered with about 95 grid points. The x direction is typically embedded with 0.5-mm equispaced grids. Some numerical experiments with a grid-point spacing of 0.25 mm were also obtained to ensure that the results are grid-independent for a large number of fluctuating parameters that are examined. The total number of grid points is 201, 251, or 301, depending on the region examined— 50, 100, or 125 mm, respectively. In one case, a 200-mm region was treated, because the growth of vortical structures was virtually absent up to 125 mm. The minimum step size chosen should, again, be able to capture the scales. The vortical scales in the axial direction are 3δ to 4δ. These scales are covered by 60 to 80 points, which is good in most cases where the flow is in the transitioning stage, but marginal in the boundary-layer case in a zone where turbulence has set in significantly.

Methodology and Tools of Examination

It is important to understand the flow behavior in each of the cases computed. Since there is a variation of the flow behavior in both space and time, there is a need to analyze both. The spatial variation is understood largely by contour plots of vorticity, pressure, and fuel mass fraction. The presence of shocks is best understood in terms of a quantity called the "shock function based on pressure." Other plots, including the v velocity—the divergence of velocity—are usually less revealing with regard to the presence of sharp changes of pressure in the flow. However, this presentation is restricted to the contour plots of pressure.

The speed of vortical structures (expected to be near the convective speed) is obtained from pressure versus x plots at some value of y near the center. These plots are made at a few times that are sufficiently spaced apart. The rate of movement of the point of peak pressure along the x-axis is the convective speed.

To determine a statistical time behavior, it is necessary to time sample the flow, preferably at equal time intervals. The SPARK2D code calculates the

time step based on a numerical stability criterion (CFL). It varies significantly in the early part of the calculation but settles down to a value with a fluctuation of about 5 percent. To take these features into account and the fact that the flow must attain a statistical steady state before sampling is performed, the code is run for each case for a duration of about three convective sweeps of the flow. Each sweep takes a time given by x_m/U_c; this is about 50 msec for the $M_c = 0.38$ case and 30 msec for the $M_c = 0.76$ case. The time step is typically 0.005 μsec; therefore, it takes 20 000 to 30 000 time steps before statistical steady state is achieved. A total of 400 to 600 time samples of the flow field involving p, u, v, T, ρ, f_i, and vorticity, in the most important y region and at specific x stations, are stored at equal time intervals. These samples are subsequently analyzed by a separate statistical package specifically developed for this purpose. The results from this package include several quantities: the mean and root mean square of fluctuations of all the parameters, Reynolds stress and other correlations of velocity with temperature, mass fractions and pressure, average thickness estimated by various means, probability density function of the passive scaler (mass fraction of H_2) and other parameters as needed, time spectra, and x spectra (wave-number plot) for the variables desired. The intention was to obtain the spectra in the y direction, but this objective was impeded by the problem of calculating the error-free integrals of the variables known at specific points (unequal intervals in y) with harmonic functions. These calculations produced a significant amount of high-frequency noise, even though a simple quadrature rule was used. The x spectra obtained from data of equal intervals were sufficient to draw inferences. The shear-layer thickness was obtained for u, vorticity, density, and H_2 mass fraction. Of these, only vorticity tends to zero at $y \rightarrow \pm\infty$, and the others tend to nonzero finite values. Therefore, the thicknesses are defined by

$$\delta_u = \frac{(U_\infty - U_{-\infty})}{(du_{mean}/dy)_{max}} \tag{12}$$

with similar definitions for density and mass fraction of H_2, with the velocity u replaced by the corresponding quantities. For vorticity thickness, the definition is given by

$$\delta_\Omega = \frac{\int_{-\infty}^{\infty} \Omega \, dy}{\Omega_{max}} \tag{13}$$

where Ω is vorticity.

Defining δ as in equations (12) and (13) turned out to be reasonable for several cases. However, in the case of the boundary layer and in some cases of

tanh profile, the preceding definitions gave what appeared to be inconsistent results. In the transitional regime (a regime where the vortical structures begin to interact and lead to other structures of smaller and larger sizes), the development of the profiles was such that the peak gradients of mean quantities did not possess a monotonically decreasing trend. A small kink in the profile, as can be seen in some of the plots of mean quantities described subsequently, upset the monotonicity of the gradients. As such, a spurious decrease of the growth of the layer was indicated, even though an examination of the plot of the mean profile did not show such a behavior. For this reason, a thickness based on a 98.5-percent free-stream value was obtained and presented.

Results and Discussion

Hyperbolic-Tangent Profile

Figure 2 shows a typical result of a structure superimposed on the grid and the grid distribution. The maximum size of the vertical structure is about 10 mm, the minimum grid size is 0.025 mm, and the grid size at the outer edge of the structure is 0.4 mm.

Figure 3 contains the plots of growth rates with axial distance for the nominal case ($M_c = 0.38$) along with a finer y grid and a finer x grid. All the cases are for a region 100 mm (in x) by 30 mm (in y). The nominal case is for 201 by 101 grid points. The finer y-grid case has 151 grid points. The finer x-grid case has 301 grid points. The growth rates are obtained by averaging 250 time samples. The differences in the results of figure 3 are the results of averaging and predictions of grid resolution at the levels employed for the nominal case.

Figure 4 contains similar plots to examine the influence of the boundary. The y region of 30 mm is extended to 50 mm. Again, the differences seen are simply the result of statistical averaging, and the boundary of $y = 30$ mm should be satisfactory. The question of the outer y boundary being kept at $y_m = 30$ mm (15 mm away from the center of the shear layer) becomes more serious for the $M_c = 0.76$ case, because, in this case, the changes in pressure are much larger than in the $M_c = 0.38$ case, and boundary effects on the radiation of these pressure waves could be more significant.

Figure 5 contains the contour plots of vorticity and pressure for the small domain ($y_m = 30$ mm with the mixing layer centered at 15 mm) and the extended domain ($y_m = 100$ mm with the mixing layer centered at 50 mm). These plots use the same scale and same range of vorticity at about the same time, though not identical. The fact that the vorticity plots

look identical may be misleading. Also, the fact that the pressure plots retain nearly identical behavior is a better indication that the outer-boundary set at $y_m = 30$ mm is reasonable. Other data involving means and fluctuations in the central 10 mm region show differences less than 3 percent — not very much larger than errors of statistical averaging, which are about 2 percent. The verification of grid resolution and boundary effect based on growth rates, means of flow variables, and contour plots of pressure was thought to be more complete with the examination of time and wave spectra.

Figures 6 and 7 refer to time and space spectra for u and v shown at the initial and final stations. The plot at the initial station shows the frequencies used to excite the layer in u and v. The spectrum approaches a function with a sharper peak by using a larger number of samples. The differences in spectra seen in other cases are the usual statistical differences. The spectra show more than a two-order range of frequencies from about 12 kHz to 1.5 MHz. The peak energy containing eddies have a frequency between 40 and 100 kHz. The quantity shown as amp is the root of kinetic energy of u fluctuations in the specific frequency range. The dominance of the initial disturbance at a frequency of 100 kHz is seen 50 mm downstream, but generation of both subharmonic and higher harmonic frequencies is taking place. At 100 mm downstream (60θ), the amplitude of the initial disturbance has come down from 100 to about 50 m/sec, and the other lower frequencies have increased in amplitude substantially (i.e., from about 5 m/sec to as much as 20 to 50 m/sec). Also, the higher frequency spectrum is populated.

Figure 8 contains the velocity-vector plots, contours of vorticity, and pressure and mass fraction of H_2 for the tanh profile case at $M_c = 0.38$. These results are included to illustrate the relationship between various quantities. The mass fraction of hydrogen follows the vorticity plot, which shows that mixing is related to the vortical structures. The pressure plot shows that the pressure is lowest near the center of the vortical structures and peaks between the structures.

The influence of intensity of fluctuations on the growth of vortical structures is shown in figure 9. With no inflow disturbances, the growth is negligible. The viscous entrainment in the laminar range is, indeed, extremely low. With an increased level of disturbances at 0.92, 1.84, and 3.68 percent (rms value), the instability begins at smaller distances, and the growth of vortical structures is stronger. If the growth of the structures was associated with the transition process, then it could be inferred that

the process has occurred at about 80 to 90 mm at 0.9 percent rms disturbance. For realistic transition distances of the order of 40 to 50 mm, the intensity of fluctuation needed is of the order of 3 percent. This is very large compared with the kind of free-stream disturbances expected in wind tunnels or free flight. This feature is strongly related to the nature of the initial profile.

Figures 10 and 11 contain the corresponding plots for $M_c = 0.76$. These plots are included for comparison with those for $M_c = 0.38$. The growth rate of the vortical structures for 3.6 percent fluctuation seems as large as for the $M_c = 0.38$ case.

Figure 12 shows the effect of the location of the disturbance on the growth of the shear layer. Disturbances in the free stream away from the shear layer seem to have little influence on the growth of the layer. Inclusion of the shear layer into the disturbance field makes all the difference, as seen from the third and fourth plots. Though a careful examination of these plots shows that the disturbance in the air side (lower) leads to slightly larger structures, a generalization is not possible with the limited results available. Disturbances set around a region that does not include the shear layer are not sufficient to realize the effects of the disturbance field. It is necessary to include the shear layer and a region of about four times the layer thickness to obtain the full effect of the disturbances. This result may have important practical implications in terms of mixing-enhancement techniques. To explicitly state the result, the introduction of disturbances around the shear layer in a frequency range anywhere from 50 to 150 kHz should be able to cause significant enhancement of mixing. The frequency range prescribed here has been obtained after a study of a wider range of parameters than discussed herein.

Figure 13 shows the mean profiles of u versus y as a function of axial distance for $M_c = 0.38$. The growth of the layer is shown by the dotted lines. The distinct change of growth rates with distance is noticeable. Since the first part of the growth is laminar, a similarity plot on the basis of u versus $y/\sqrt{x}$ is presented in figure 14. The laminar similarity seems to be well obeyed for this range. A plot containing data up to 100 mm showed that no laminar similarity exists in the latter portion (not shown here). The turbulent flow similarity is on a basis of u versus $(y - y_0)/(x - x_0)$. In this coordinate, y_0 is the center of the mixing layer and x_0 is the virtual origin. The value of x_0 is not known a priori. Figure 13 shows that the virtual origin x_0 lies at approximately 0.015 m. Collapsing the data in terms of this similarity variable is shown in figure 15.

Determination of convective speed is based on the speed of the structures. The movement of the vortical structures also causes a movement of the pressure versus x profiles. The plots of p versus x at a specific y station for $M_c = 0.38$ and 0.76 are shown in figures 16 and 17. Even at $M_c = 0.38$, the changes of pressure are, by no means, insignificant; they vary between 0.07 and 0.14 MPa. For $M_c = 0.76$, the pressure variation is between 0.045 and 0.17 MPa. The free-stream pressure is 0.101325 MPa; therefore, the pressure variation over the free-stream value is significant. The flow has shocks and regions of expansion. One of the interesting features of the flow is that the regions of shocks occur between structures and over them. The flow pattern seen here is different from those observed in reference 6 for air at comparable values of M_c. The shapes of the pressure x plots seem to be the same at various times, certainly at the times shown in figure 16. On the other hand, the shape of the pressure variation for $M_c = 0.76$, shown in figure 17, does not remain the same, and there are serious distortions in the shapes for much shorter times than the sweep time. Convective speeds obtained from the structures based on a procedure described previously are presented in table 4, and the results from the standard formula are also shown. There seems to be a difference of 100 m/sec in the first tanh case, where $M_c = 0.38$. There is a much smaller difference in the boundary-layer case; it may be good enough for showing the convective speeds. For the high values of M_c, the difference in the two results is even larger (≈ 250 m/sec). In one sense, this difference is understandable because of the dilatation of structures. In another sense, it reflects the possible invalidity of the formula at high values of M_c. In view of this uncertainty, a calculation was made for a composition with 30 percent H_2 by mass in the fuel stream and with the convective speed evaluated. In this case, the density ratio (≈ 5.1) was intended to verify the nature of the previous results. However, even in this case, the difference between the speed of the structure and the result from the formula seems different by about 100 m/sec. Perhaps the expected accuracy of the formula can be no better than 3 to 4 percent. In the case of $M_c = 0.76$, the result for u_c is different by 7 percent, and the basic issue of dilatation of structures affecting the result remains. Hence, the use of M_c, in a manner other than designating the condition, needs to be examined carefully.

Figures 18 and 19 show the growth of the layer computed from formulas described previously for u, ρ, and H_2 mass fraction. The thicknesses seem to decrease after some growth. The fact that growth decreases, is, by itself, not very surprising. Forced

shear layers show such trends (ref. 19), but typically at less than 10 percent. The dips in some quantities in figures 18 and 19, particularly the latter, are more than this magnitude. Careful examination showed that these dips are related to the way that mean profiles of various quantities behave during transition. A small kink in the transitioning mean profile can cause the presence of a local gradient smaller than in the downstream location. This difference causes a slightly larger growth rate. It may likewise turn out downstream that, although the growth rate is larger, there is a lower estimate of the growth. The combination of these events produces curves of the shapes seen in figures 18 and 19. The growth rates that can be extracted from these plots are discussed subsequently, along with results of the boundary-layer profile.

Figures 20 to 26 refer to the statistics of fluctuating quantities. Figure 20 shows the variation of the rms value of u in the field. The top portion shows the variation along x at a particular y station. Although the information contained in the top portion is embedded in the two-dimensional plot, it is explicitly brought out for a clearer appreciation. At larger intensities of fluctuation, the fluctuations decrease over a part of the flow field before the amplification process takes control. The fluctuation profile with y is not symmetric. A front is apparently created (≈ 50 mm) and is strengthened to a sharp peak on the air side. The intensity of fluctuations seems to settle down to values of about 6 to 8 percent, irrespective of the initial fluctuation intensity. This is one indication of the fact that the subsequent region of the flow is becoming independent of the initial distribution of the fluctuation.

Figure 21 shows the variation of v fluctuations. The instantaneous values of the v velocities seem very large, as large as 400 m/sec, and they have a large deviation on either side of zero. These velocities cause the flow to show up as large structures on a vorticity plot. The velocity-vector plots in figures 8 and 10, where the vector is changing directions, are also reflective of these cross-stream velocities. The changes in velocity directions in a supersonic flow result in shock waves, and these cause large pressure variations in the mixing layer. The mean velocity, however, is not large by comparison (± 15 m/sec). The peak rms value of a v fluctuation is 8 percent, which is comparable to the peak rms value of u fluctuations. This feature is also reminiscent of fully turbulent flows. The fluctuation peaks toward the air side (lower). The mean and rms density are presented on an x-y plot. The initial change of density from 0.075 to 0.175 kg/m^3 is evident from the mean

density plot. The growth of the layer from zero thickness is clearly visible. The rms value of the ρ profile acquires a top-hat profile with a maximum of 34 percent. The intensity aspect of the density profile is that the top-hat profile is acquired around the transition region; broadening of the profile is the only thing that happens farther downstream.

The mean and rms temperature variations are shown in figure 23. The temperature profile in the present calculation is, like a passive scalar and unlike H_2 mass fraction, affected by gas dynamics. There are changes in the mean temperature to the extent of 25 to 30 K, a decrease from the set initial value. The extent of the change of temperature must be understood in terms of energy exchange between random energy and ordered energy. If the inviscid global gas dynamics equation is used along stream lines as follows:

$$c_p T + \frac{V^2}{2} = \text{Constant} \qquad (14)$$

we can differentiate; then, $\Delta T \approx -V \Delta V / c_p$, where V is the magnitude of the vector velocity. For typical values ($V \approx 2250$ m/sec, $\Delta V \approx 20$ m/sec, and $c_p \approx 1800$ J/kg-K) $\Delta T \approx 25$ K, a value consistent with the change shown in the upper plot of figure 23. The fluctuation of the rms value of T seems to stabilize around 3 percent. This fluctuation is induced by the fluid mechanical effects; there are no other energy-exchange mechanisms. Figure 24 shows the plot of mean and rms values of H_2 mass-fraction profiles; rms mass fraction is not normalized. Therefore, the peak rms normalized by the mass fraction of the input fuel stream is about 0.2 percent. While the plot of the mean profile looks similar to that of density (in a reversed manner), the variation of the rms H_2 mass fraction seems quite different from that of density. The curve looks like a Gaussian distribution. The relationship between mean-density and mass-fraction profiles is expected because density changes are caused only by molecular weight changes induced by H_2 diffusion into the airstream.

Figure 25 shows the plot of vorticity and Reynolds shear-stress fields. The Reynolds shear-stress profile appears to be growing in size and magnitude at 100 mm (64θ downstream). This trend shows that the transition process is incomplete. An attempt is made to examine the validity of the Baldwin-Lomax model for turbulence. In this model, the shear stress is represented by $\overline{\rho u' v'} = \text{Constant } [\rho_m (\delta_\Omega \Omega_m^2)]$, where δ_Ω is the vorticity thickness, Ω_m is the mean vorticity, and primes denote fluctuations about the mean. The constant is calculated from the actual

values of the left- and right-hand terms and plotted in figure 26. These calculations were made for both 101 and 151 grid points to establish the validity of the results. As shown in the plot, the "constant" is constant over a region of the mixing layer but departs from it significantly, particularly in the peak shear-stress area. The fact that the flow has not developed into a fully turbulent regime may be partly responsible for this departure. If a magnitude must be used for the constant, it would be about 0.015. Furthermore, what is still not clear is what influence the assumption of constancy has on the prediction of growth rates of turbulent shear layers. These issues have to wait for calculations of modeled equations.

Boundary-Layer Profile

Figure 27 shows the plot of the vorticity contours for a range of initial disturbances from 0 to 3.68 percent. The contour plots of vorticity appear thinner than for the tanh case, because, unlike the tanh case, vorticity changes signs across the shear layer. Note the difference in the scales between the boundary-layer and tanh cases.

The plots are very informative. With no imposed fluctuations, there seems to be an onset of instability at about 80 mm from the splitter plate, and a few vortical structures have begun to develop. The spacing of the vortical structures seems much smaller than for the tanh case. The average spacing for the boundary-layer case is about 6 mm and 23 mm for the tanh case. The spacing is normalized with respect to initial-layer thickness (2 mm) and is 3.0 for the boundary-layer case and 11.5 for the tanh case. The observed spacing ratio is about 2 (ref. 13). This is the first indication that the results of the boundary-layer profile show more realistic results than the tanh profile. The point where the first vortical structure gets developed, which may be taken as indicative of the beginning of transition, moves substantially to lower x values with the imposition of small, but realistic, disturbance levels. The transition distances are 35, 27, 25, and 20 mm at progressively increasing disturbance levels.

The single large jump in the transition distance occurs from 80 mm to 35 mm for a change in disturbance level from 0 to 0.115 percent. Subsequent increases in disturbance level seem to have progressively less influence. The transition distance, normalized by momentum thickness, is 345 for a 0.115-percent disturbance level and 265 for a 0.23-percent disturbance level. The experimentally observed transition distance is 165 to 300θ (table 1). Transition distances up to 700θ are quoted for various cases in reference 13. The transition Reynolds number can be computed based on $R_T = \rho_{avg} u_c x_T / \mu_{avg}$. When $\rho_{avg} = 0.125$ kg/m^3, $u_c = 2150$ m/sec, and $x_T = 0.04$ m, R_T is 0.18×10^6. The value of u_c used here is from the standard equation and is not the value obtained from the calculations. The difference between the two values is no more than 5 percent, and this difference is quite small for the estimation of R. The transition R_T given in reference 9 is $0.2 \times 10^6 \pm 0.03 \times 10^6$. The results from reference 18 were quoted previously to be between 0.36×10^6 and 0.53×10^6. These values are based on free-stream velocity. If they are based on the convective speed of the structures, which, in this case, is half the free-stream speed, the transition Reynolds number is 0.18×10^6 to 0.26×10^6. Again, the comparison seems good between the experimental values and the predictions. Thus, the present results with boundary layer as the initial profile seem to predict realistic transitional features at realistic disturbance levels.

The transition behavior is more vividly depicted on time-spectra plots shown in figure 28 for three x and y stations. The spectra are shown for both 0- and 0.115-percent disturbance-level cases. The upper plot shows the time spectra at $x = 0$. The disturbance seen in this figure at $x = 0$ is consistent with the description of initial-disturbance structure discussed previously. The peak disturbance is about 1 to 2 m/sec in the central zone. At $x = 50$ mm downstream, the amplitudes are 10 to 20 m/sec and are 50 to 90 m/sec at $x = 100$ mm downstream. The mean velocity has also increased from near zero to as high as 1500 m/sec during this transition. The nature of the plot at the downstream stations shows that most other frequencies, both subharmonic and the higher harmonics, are excited perhaps more strongly than indicated with the tanh profiles. The plots, with respect to the case involving no disturbances, show that the flow has picked up noise that was generated numerically. Interestingly, the disturbance is selectively amplified, and peak growth occurs at about 150 kHz, which implies that the shear layer is sensitive to disturbances at this frequency. This result can be expressed in terms of a nondimensional quantity, $St = \theta f / u_c$, where f is the frequency. For $\theta = 0.102$ mm and $u_c = 2150$ m/sec, $St = 0.007$. Perhaps $St = 0.007$ as a criterion for excitation is valid over a much larger range of parameters. In reference 24, a quantity called "preferred mode" is indicated in jets and mixing layers, and the Strouhal number is between 0.002 and 0.012. It is stated in reference 24 that "mixing layers can be manipulated effectively with very low forcing levels -0.01 to 0.1 percent of the average velocity—provided the excitation

11

is applied at the proper frequency." This comment is entirely consistent with the observations of the present computations.

Figure 29 shows the plots of pressure versus x for three successive times. The extent of the pressure fluctuations is the same as in the tanh case, but, consistent with the vorticity plot, the profile has many more waves within the same range of x. The convective speed, computed from the movement of the pressure waves with time, is presented in table 4. As was also indicated previously, this value compares well with that from the formula.

Figure 30 shows the plot of the mean u profiles and the minimum u velocity versus x. A plot of minimum u with a nondimensional x defined by $x_{mn} = x/(\theta R_\theta)$ is presented in reference 11. The Reynolds number uses the average of the unit Reynolds number on both sides. The plot shows that at about $x_{mn} = 1$, the asymptotic value is reached. Substituting the values of various quantities and obtaining x, a value of x that corresponds to $x_{mn} = 1$, yields $x = 45.5$ mm. The upper plot of figure 30 shows that the asymptotic value of u seems to have been reached at $x = 40$ to 50 mm.

Figure 31 shows the plot of the rms value of u over the field. The rms value of u increases from a relatively low value of 0.1 percent, builds up to around 10 percent, and then seems to saturate at this level throughout the field after the transition process starts. A careful examination shows that the rms value of u versus y seems to have attained similarity around 90 mm (900θ). The rms value of v seems to peak and decay downstream of 600θ (fig. 32). The mean v is near zero throughout the field. The instantaneous v goes up to ±100 m/sec. The mean and rms values of density are shown in figure 33. Unlike the tanh case, the rms profiles do not seem to have the top-hat shape, and the variation with y is asymmetric. The peak rms goes up to 20 percent, and the mean-density profile appears to be approaching similarity. The temperature and H_2 mass-fraction profiles are presented in figures 34 and 35. The mean profiles are similar to those obtained for the tanh case. The rms profile shapes are slightly different, but the features—namely, the peaking of rms intensity and subsequent decay in the axial direction and magnitudes—are about the same as for the tanh case.

The growth data for the boundary layer are presented in figure 36. As explained previously, the growth was obtained by using the u profile. The results for most fluctuations show a region of small decay before the growth is established; this decay

may be due to a coupling between the inflow disturbance structure and the flow instability. For large fluctuations, the growth rate is approximately linear. In the other cases, a growth rate can be derived in the range where there is no decay or constancy. Surprisingly, the slope obtained for these cases is nearly the same. These growth-rate data are presented in table 5. The results obtained for other tanh cases are also shown in this table. The growth-rate trends for various fluctuation intensities are not the same. In all cases, the growth rates were estimated from the slopes in the latter part of the x range. The linear growth rate for the lower intensity fluctuations may not have been achieved. The growth rates based on H_2 mass fraction or density are the same for all the fluctuation intensities. The data for $M_c = 0.76$ were derived from similar considerations. Again, there are variations. An estimate of the mean value of the growth rate was obtained and is included in the table. Further, the growth rate is divided by that for the incompressible case (eq. (1)) to obtain the compressibility effects as in the results of reference 13. These data are presented in figure 37 with experimental results. While there is significant variation of the numerically obtained result, the reduction of the growth rate with M_c is unmistakable. It may well be that if the simulations are carried out for much larger values of x_m/θ, the growth-rate data would lead to a more consistent picture.

Figure 38 shows the terms of the conservation equations of u, v, and energy. The only dominant terms are the unsteady and convective terms. The pressure-gradient terms are about 25 percent of the convective terms. The viscous terms seem insignificant on the scale shown, but the flow is not necessarily inviscid. The flow is affected by fluctuations not evident in the plot of instantaneous quantities. These fluctuations lead to a stress like the viscous stress (the Reynolds stress), which is known to be important. To determine their importance, the terms must be averaged and the relative orders of magnitude must be examined. This determination shows that the Reynolds stress terms constitute up to 30 percent of the convective terms. Figure 39 confirms the validity of these results in terms of the variation of pressure; variation of pressure affects Reynolds number. Changing the Reynolds number by a factor of 4 causes little change to the vortical structures and the mean growth rates. Data for incompressible shear layers for local Reynolds number with fixed x (in the case considered 0.45 m downstream), in which a change in Reynolds number from 4.3×10^4 to 6.7×10^4 shows a visible change in growth rate, are presented in reference 10. Since the full experimental

details of this work are unpublished, the resolution of the issues involved in the experiments must await discussion at a future time.

Conclusions

This study is an exploration of the direct numerical simulation of high-speed mixing layers. After establishing the validity of the approach to resolving the mixing layer and the methods of exploring the structure of the mixing layer, the issues concerning the effects of free-stream disturbance intensity, the nature of the profiles, and the role of Reynolds number are studied. The following conclusions are drawn from the present study:

1. The calculations show that the profile of the hyperbolic tangent calls for unnaturally large disturbance levels (≈ 3 to 4 percent) to initiate transition in the flow. Boundary-layer profiles, on the other hand, show transition Reynolds numbers of about 0.18×10^6; these numbers are consistent with the experimental results at disturbance levels of the order of 0.1 percent. The transition Reynolds number does not strongly depend on disturbance intensity over a range up to 0.2 percent.

2. The asymptotic turbulence intensities attained in the shear layer for the boundary-layer case (10 percent) are larger than for the hyperbolic-tangent (tanh) profile (6 percent), and the same trend is true for Reynolds number stress.

3. Convective Mach numbers derived from the pressure versus streamwise coordinate plots show significant differences from those computed with standard formulas to a large extent at high convective Mach numbers. These differences are related to the significant changes in the shape of the vortical structures in the flow field with time. This feature makes the idea of a convective Mach number less representative in distinguishing flows of different compressibility at high convective Mach numbers.

4. The estimates of the growth rates from the latter region in growth versus streamwise coordi-
nate plots are straightforward in most cases, and the growth rates that are normalized with incompressible growth rates decrease with the convective Mach number. This decrease is consistent with known experimental results. The spread in the results is probably the result of the limited axial extent of the field explored.

5. Reynolds number has negligible effects on the growth and structure of the mixing layer for the range of Reynolds number considered. This result is not surprising in view of the dominance of inviscid effects over viscous effects.

6. The utility of the direct simulation approach in examining turbulence models is briefly demonstrated on the Baldwin-Lomax model. The constant in the relationship between the Reynolds shear stress and the mean vorticity varies significantly over the region. For a subset of the region, the constant remains about the same from a value of 0.015. These kinds of studies can be performed with the data base that is archived for this purpose.

The relative utility of tanh and boundary-layer profiles in studies of mixing layers needs to be considered. The tanh profile has the obvious advantage of leading to analytical solutions to stability problems that are vital for making generalizations. The boundary-layer profile, which is closer to reality in experiments, has the disadvantage of not being close to the solution of the steady problem; therefore, it is not amenable to classical stability treatment. If one intends to capture the transition processes and compare them with experiments, there is no alternative to the boundary-layer profile. Thus, the tanh and boundary-layer profiles both have their regions of importance in the study of mixing layers.

Appendix

Numerical Algorithm

For supersonic flows, no other algorithm has been more widely used than the method discussed in reference 25. Over the last 20 years, this method has been repeatedly compared with other codes and with experimental data. Recent efforts have been made to improve the accuracy of the method by increasing the spatial truncation error to fourth order and thus reducing some of the dispersive errors of the method. A fourth-order variant of the original MacCormack algorithm (a five-point linear stencil) has been addressed in references 22 and 26. These references show that increased resolution is obtained for a broad class of problems with the fourth-order method.

In the last decade, a wealth of upwind algorithms have been developed. These methods incorporate numerical stencils which align with the direction that information is propagating in the flow. This propagation is usually accomplished by decomposing the governing equations into a form in which each characteristic wave can be differenced in an upwind manner. Numerous implementations of these methods have shown a great deal of success in resolving supersonic problems of practical interest. In spite of the success of upwind algorithms for the Euler equations, difficulties exist for their use in supersonic chemically reacting flow problems. Specifically, the chemistry system is extremely difficult to formulate along characteristic directions, and many of the upwind methods are not easily generalizable with chemically reacting flows.

The basic characteristics of central- and upwind-difference algorithms, as well as the beneficial attributes of higher order algorithms, can be observed in a two-dimensional model problem (referred to as the color problem) designed to demonstrate numerical diffusion and dispersion. (See ref. 27.) Different numerical algorithms are compared with an exact solution and with each other to determine the characteristic of each. The test problem used in this study is the two-dimensional advection of a scalar field defined by the equation

$$\frac{\partial \Psi}{\partial t} + \frac{\partial (U\Psi)}{\partial x} + \frac{\partial (V\Psi)}{\partial y} = 0 \qquad (15)$$

with

$$\Psi(x, y, 0) = \Psi_o(x, y) \qquad (16)$$

and with suitable boundary conditions. The velocity vector was chosen to be a solid-body rotation defined by

$$\left. \begin{array}{l} U = -\Omega y \\ V = \Omega x \end{array} \right\} \qquad (17)$$

with $\Omega = 2\pi$, so that one complete revolution of the flow occurred in one unit of time. The domain that was used corresponded to the domain $-1 \leq x, y \leq 1$. Dirichlet or first-order extrapolations were used for the boundary conditions for flows entering or exiting the domain. The boundaries were located suitably far from the regions of interest so that the lower order treatment did not affect the quality of the results. The grid used 100 by 100 uniformly spaced points on which to solve the governing finite-difference equations. All calculations were integrated in time until the initial distribution had rotated exactly once. The distribution was then compared with the initial distribution by using two error norms: the L_∞ or maximum error norm, and the L_2 norm.

Figure 40 shows the initial distribution on the grid used in this study. The initial value of Ψ was chosen to be 1 in the interior of the "L-shaped" body and 0 elsewhere. This distribution is discontinuous and is a serious test of the dispersive properties of an algorithm. Reference 28 shows that this discontinuity seriously degrades the accuracy of the solutions and that the error (L_∞ or L_2) decays no better than first order with increasing spatial resolution, regardless of the spatial accuracy. With higher order algorithms, the error is confined to a narrower region about the discontinuity and thus contributes to a slightly better L_2 norm. This distribution was chosen to more closely approximate the discontinuous behavior of the Euler equations.

Figures 41 and 42 show the results obtained after one complete revolution of the initial distribution with the standard MacCormack and fourth-order Gottlieb-Turkel algorithms. Contours ranging from 0 to 1 are plotted in steps of 0.05 (21 contour levels). The sharp distinction between regions initially at a value of $\Psi = 1$ and the surrounding regions at $\Psi = 0$ is no longer apparent. The dispersive nature of the algorithm has distorted the solution dramatically. The regions inside the innermost contour level are at values greater than 1 and are numerical in nature. The convection of the initial discontinuity is much better accomplished with the fourth-order method. The outer boundary of the initial distribution is nearly replicated with the fourth-order schemes. The contour levels in the interior regions of the solution, where $\Psi < 1$, indicate that the numerical dispersion is present. Thus, although the fourth-order schemes track the discontinuity with much greater accuracy,

14

they still exhibit significant over and undershoots near the discontinuity.

Figure 43 shows the same test problem with the third upwind-biased algorithm. In all these calculations, the stencil was oriented in the upwind direction, and was therefore varied in each of the four quadrants of the test problem. The third-order upwind-biased algorithm produces a clean solution after one complete rotation. The location of the discontinuity is somewhat diffused at the corners relative to the fourth-order central-difference algorithms, but the two-dimensional dispersion present in the central-difference algorithms is eliminated.

When the quantitative features of the upwind algorithms are compared with the central-difference algorithms, it is apparent that the fourth-order scheme tracks the discontinuities more accurately than does the upwind algorithm, but it has far more two-dimensional overshoots and undershoots than the upwind algorithm. Except for the diffused corners of the discontinuity, the third-order upwind algorithm provides a very accurate solution. The algorithms of at least third-order accuracy provide significant improvement over the second-order central-difference algorithms.

To quantify some of these observations, the error after one complete revolution of the initial distribution was calculated. Both the L_∞ norm (shown by the maximum or minimum of the solution over the entire domain) and the L_2 norm are presented. Table A1 shows all the algorithms, the maximum and minimum values of Ψ, the L_2 norm, and the CFL at which the calculations were performed. The L_{max} and L_{min} norms for the upwind case are reduced by the higher order algorithms, especially for the upwind algorithms. Also, the L_2 norm for the third-order upwind and the fourth-order schemes is nearly the same. These observations are characteristic of the comparison between upwind and centered schemes. With higher order schemes, the efficiency and robustness achieved in solving realistic problems decrease. The third-order upwind-difference and fourth-order central-difference schemes represent truncation levels that compromise the extremes of accuracy versus efficiency.

The SPARK2D code used in the present study incorporates a combination of upwind- and central-difference schemes. The numerical simulation of the supersonic mixing layer is ideally suited for the use of upwind-biased algorithms in the streamwise direction. Because the flow is supersonic, all the eigenvalues are oriented in the same direction. The equations can be differenced in an upwind manner without a

characteristic decomposition. A third-order upwind-biased algorithm has been chosen as the numerical algorithm for the streamwise direction. It shows low phase errors and acceptable levels of numerical dissipation, with extremely good characteristics for capturing discontinuity.

Table A1. Error Norms From Different Schemes

Scheme	Order	L_{max}	L_{min}	L_2	CFL
MacCormack (ref. 25)	$\Delta t^2, \Delta x^2, \Delta y^2$	1.429	-0.378	7.76×10^{-4}	1
Gottlieb-Turkel (ref. 22)	$\Delta t^2, \Delta x^4, \Delta y^4$	1.337	$-.239$	5.19	2/3
Third upwind	$\Delta t^3, \Delta x^3, \Delta y^3$	1.148	$-.108$	5.29	1

Extremely strong gradients exist in the cross-stream direction. A higher order numerical algorithm is ideally suited for this direction. Since the flow in this direction is always subsonic, central-difference methods are ideally suited. The fourth-order method of reference 22 is used in the cross-stream (and normal for the three-dimensional case) direction. The numerical algorithm in two spatial dimensions can be described by the model equation $U_t + F_x + G_y = 0$ as

$$
\begin{aligned}
\overline{U}_{i,j} &= U_{i,j}^n - \frac{\Delta t}{6\Delta x}\left(2F_{i+1,j} + 3F_{i,j} - 6F_{i-1,j} + F_{i-2,j}\right) \\
&\quad - \frac{\Delta t}{6\Delta y}\left(-G_{i,j+2} + 8G_{i,j+1} - 7G_{i,j}\right) \\
U_i^{n+1} &= \frac{1}{2}\Big[U_i^n + \overline{U}_{i,j} - \frac{\Delta t}{6\Delta x}\left(2\overline{F}_{i+1,j} + 3\overline{F}_{i,j}\right. \\
&\quad \left. -6\overline{F}_{i-1,j} + \overline{F}_{i-2,j}\right) \\
&\quad - \frac{\Delta t}{6\Delta y}\left(7\overline{G}_{i,j} - 8\overline{G}_{i,j-1} + \overline{G}_{i,j-2}\right)\Big]
\end{aligned}
\right\}
$$

$$(18)$$

The fourth-order Gottlieb-Turkel scheme is stable for CFL $\leq \frac{2}{3}$ and thus limits the maximum allowable CFL. The Gottlieb-Turkel scheme is not applicable at the grid point next to the boundary and must rely on a standard MacCormack difference formula at that point. Similarly, the upwind scheme is not defined at the first and second axial grid points and relies on a first-order upwind scheme at that point. Explicit numerical damping, which is often added to codes for engineering calculations, was not used here for reasons of accuracy. The only numerical dissipation present was that generated by the algorithm itself.

Code Validation

The first step in validating the code was to determine if the numerical methods used in the SPARK2D code are capable of resolving the linear growth of the two-dimensional mixing layer. It is essential that all the aspects of the linear regime of the mixing layer be well resolved for grids comparable to those used in this study before addressing the far more difficult nonlinear problem of vortex roll-up and chemical reaction. Linear stability theory predicts that the temporally developing compressible two-dimensional mixing layer (air into air) is unstable for a velocity profile that is initially specified as a hyperbolic-tangent axial-velocity distribution. In the initial stages of the instability (the linear regime), the growth of the unstable modes is exponential. For these calculations, accurate eigenmodes are provided from a spectral linear stability code developed in reference 3. From these eigenmodes, nondimensional growth rates and characteristic frequencies were calculated. This nondimensional growth rate provided a reliable measure of the accuracy of the finite-difference algorithm being tested.

The temporal growth of the two-dimensional mixing layer is simulated by assuming the flow to be periodic in the streamwise direction. The period corresponds to a wavelength of $x = 0.6283$ mm (the mode that grows most rapidly, as determined from the linear analysis). The initial velocity distribution is specified as $U(x, y, 0) = u_\infty \tanh\left(\frac{y}{\delta}\right)$, $V(x, y, 0) = 0.0$, $T(x, y, 0) = 293$ K, and $P(x, y, 0) = 1$ atm. Source terms were added to the Navier-Stokes equations, so that the momentum and energy equations would preserve the free stream. The resulting Reynolds number of the flow is 0.187×10^3, based on the layer thickness, where $U_\infty = 100$ m/sec. The Mach number is 0.30. The width of the half-layer D is 2.5×10^{-2} mm, and the half-width of the domain is 100 times the layer thickness. The grid in the streamwise direction is uniform, while the grid in the cross-stream direction is highly stretched. The transformation of the grid ensures that about half of all the y grid points are located within the initial mixing-layer width.

For these studies, the unstable modes in the layer were allowed to grow from the numerical instabilities

produced by the machine round-off errors. Exponential growth of these modes was seen in all cases after an initial transient period. The "linear" regime was characterized by the growth period, during which the product of perturbation quantities was still negligible. For these tests, that period was arbitrarily between 2.5×10^{-5} and 2.75×10^{-5} sec and corresponded to disturbance amplitudes three to five orders of magnitude larger than machine round-off errors. A grid convergence history of the numerical method was used to determine its formal accuracy and to ascertain the grids necessary to resolve this fundamental phenomenon.

The most unstable mode in this problem grows at an exponential rate, with an exponent determined from linear stability theory to be 0.140000 in nondimensional units. This rate was used as the "exact" growth rate for these conditions. A series of four grids were then defined, each with a grid density that was a constant multiple of the previous grid. Three algorithms —MacCormack (ref. 25) at CFL = 1.0, Gottlieb-Turkel (ref. 22) at CFL = 0.5, and DCPS (ref. 27) at CFL = 0.5— were then run on identical grids, and the nondimensional amplification rate was determined from an integration of the energy spectrum. (The integral of the fundamental mode over the entire domain was monitored in time. The change, with respect to time, yields the amplification rate.)

In figure 44, the amplification rates of the three methods are plotted against $\left(\frac{N_{max}}{N}\right)^4$ to show quartic accuracy. The symbols N and N_{max} are the number of grid points and the maximum number of grid points used in the study, respectively. Here, the fourth-order spatial accuracy of the spatial derivative from each method is indicated by the linear convergence of the solution to the predetermined amplification rate. The Gottlieb-Turkel scheme and the DCPS algorithm both converge with fourth-order accuracy. It is apparent from these results that, even for coarse grids (10 grid points per wavelength), the fundamental features of the linear growth of the mixing layer are resolved. There should be no question that the grids used in these studies are sufficient to resolve the linear regime of the two-dimensional mixing layer.

References

1. Papamoschou, Dimitri; and Roshko, Anatol: The Compressible Turbulent Shear Layer: An Experimental Study. *J. Fluid Mech.*, vol. 197, Dec. 1988, pp. 453–477.

2. Gropengiesser, Hans: *Study on the Stability of Boundary Layers and Compressible Fluids.* NASA TT F-12,786, 1970.

3. Macaraeg, Michéle G.; Streett, Craig L.; and Hussaini, M. Y.: *A Spectral Collocation Solution to the Compressible Stability Eigenvalue Problem.* NASA TP-2858, 1988.

4. Riley, James J.; Metcalfe, Ralph W.; and Orszag, Steven A.: Direct Numerical Simulations of Chemically Reacting Turbulent Mixing Layers. *Phys. Fluids*, vol. 29, no. 2, Feb. 1986, pp. 406–422.

5. Sandham, N. D.; and Reynolds, W. C.: The Compressible Mixing Layer: Linear Theory and Direct Simulation. AIAA-89-0371, Jan. 1989.

6. Lele, Sanjiva K.: Direct Numerical Simulation of Compressible Free Shear Flows. AIAA-89-0374, Jan. 1989.

7. Birch, Stanley F.; and Eggers, James M.: A Critical Review of the Experimental Data for Developed Free Turbulent Shear Layers. *Free Turbulent Shear Flows, Volume I—Conference Proceedings*, NASA SP-321, 1973, pp. 11–40.

8. Maydew, R. C.; and Reed, J. F.: Turbulent Mixing of Compressible Free Jets. *AIAA J.*, vol. 1, no. 6, June 1963, pp. 1443–1444.

9. Sirieix, M.; and Solignac, J. L.: Contribution a l'Etude Experimentale de la Couche de Melange Turbulent Isobare d'un Ecoulement Supersonique. *Separated Flows*, Part 1, AGARD-CP-4, Pt. 1, May 1966, pp. 241–270.

10. Dimotakis, Paul E.: Turbulent Free Shear Layer Mixing. AIAA-89-0262, Jan. 1989.

11. Brower, Timothy L.: Experiments on the Free Shear Layer Between Adjacent Supersonic Streams. M.S. Thesis, Montana State Univ., Mar. 1983.

12. Ikawa, Hideo; and Kubota, Toshi: Investigation of Supersonic Turbulent Mixing Layer With Zero Pressure Gradient. *AIAA J.*, vol. 13, no. 5, May 1975, pp. 566–572.

13. Papamoschou, D.; and Roshko, A.: Observations of Supersonic Free Shear Layers. AIAA-86-0162, Jan. 1986.

14. Papamoschou, Dimitri: Experimental Investigation of Heterogeneous Compressible Shear Layers. Ph.D. Thesis, California Inst. of Technology, 1987.

15. Papamoschou, Dimitri: Structure of the Compressible Turbulent Shear Layer. AIAA-89-0126, Jan. 1989.

16. Messersmith, N. L.; Goebel, S. G.; Frantz, W. H.; Krammer, E. A.; Renie, J. P.; Dutton, J. C.; and Krier, H.: Experimental and Analytical Investigations of Supersonic Mixing Layers. AIAA-88-0702, Jan. 1988.

17. Simpers, G.; Vas, I. E.; and Bogdonoff, S. M.: Turbulent Shear Layer Reattachment at M~3. AIAA Paper 77-43, Jan. 1977.

18. King, Rudolph A.; Creel, Theodore R., Jr.; and Bushnell, Dennis M.: Experimental Study of Free-Shear Layer Transition Above a Cavity at Mach 3.5. AIAA-89-1813, June 1989.

19. McInville, Roy M.; Gatski, T. B.; and Hassan, H. A.: Analysis of Large Vortical Structures in Shear Layers. *AIAA J.*, vol. 23, no. 7, July 1985, pp. 1165–1171.

20. Soetrisno, Moeljo; Eberhardt, Scott; Riley, James J.; and McMurtry, Patrick: A Study of Inviscid, Supersonic Mixing Layers Using a Second-Order TVD Scheme. *A Collection of Technical Papers, Part 2—AIAA/ASME/SIAM/APS 1st National Fluid Dynamics Congress*, July 1988, pp. 1087–1094. (Available as AIAA-88-3676-CP.)

21. Drummond, J. Philip: *A Two-Dimensional Numerical Simulation of a Supersonic, Chemically Reacting Mixing Layer.* NASA TM-4055, 1988.

22. Gottlieb, David; and Turkel, Eli: Dissipative Two-Four Methods for Time-Dependent Problems. *Math. Comput.*, vol. 30, no. 136, Oct. 1976, pp. 703–723.

23. Reynolds, W. C.: The Potential and Limitations of Direct and Large Eddy Simulations. *Whither Turbulence? Turbulence at the Crossroads*, J. L. Lumley, ed., *Volume 357 of Lecture Notes in Physics*, Springer-Verlag, 1990, pp. 313–343.

24. Ho, Chih-Ming; and Huerre, Patrick: Perturbed Free Shear Layers. *Annual Review of Fluid Mechanics*, Volume 16, Milton Van Dyke, J. V. Wehausen, and John L. Lumley, eds., Annual Reviews Inc., 1984, pp. 365–424.

25. MacCormack, Robert W.: The Effect of Viscosity in Hypervelocity Impact Cratering. AIAA Paper No. 69-354, Apr.–May 1969.

26. Turkel, Eli: On the Practical Use of High-Order Methods for Hyperbolic Systems. *J. Comput. Phys.*, vol. 35, no. 3, May 1980, pp. 319–340.

27. Carpenter, M. H.: A High-Order Compact Numerical Algorithm for Supersonic Flow. *Twelfth International Conference on Numerical Methods in Fluid Dynamics*, K. W. Morton, ed., *Volume 371 of Lecture Notes in Physics*, Springer-Verlag, 1990, pp. 254–258.

28. Orszag, Steven A.; and Israeli, Moshé: Numerical Simulation of Viscous Incompressible Flows. *Annual Review of Fluid Mechanics,* Volume 6, Milton Van Dyke, Walter G. Vincenti, and J. V. Wehausen, eds., Annual Reviews, Inc., 1974, pp. 281–318.

Table 1. Data and Results of Previous Investigations

Quantity	Reference 11 (case 1)	Reference 11 (case 2)	Reference 13	Reference 16
M_1/M_2	2.8/2.15	2.7/1.67	3.1/1.7 and others	1.95/1.33
U_1/U_2, m/sec	655/580	630/515	Ratio = 1.4	500/380
δ_1/δ_2, mm	2.0/2.0	1.6/1.4	0.44/0.36	2.0/2.3
θ_1/θ_2, mm	0.123/0.152	0.12/0.125	0.042/0.069	NA
p_1/p_2, Pa	2089/2294	2895/3673	NA	Nearly same
T_1/T_2, K	130/174	134/206	NA	169/220
M_c	0.325	0.515	0.6	0.31
Gases	Air/air	Air/air	N_2/N_2 and other gases	Air/air
Comments	u profile takes more than 80 mm to go near equilibrium; Transition $\approx 165\theta$; dominant frequency ≈ 93 kHz	u profile takes more than 80 mm to go near equilibrium; Transition $\approx 300\theta$; dominant frequency ≈ 130 kHz	Growth rate by pitot surveys; Transition ≈ 40 to 60 mm	Growth rates measured as 0.011

Table 2. Inflow Parameters

[$T = 2000$ K; $p = 0.101325$ MPa; θ (tanh case) $= 1.54$ mm; θ (boundary-layer case) $= 0.102$ mm]

Composition	Parameter	Case 1	Case 2
Fuel: $0.1H_2 + 0.9N_2$	ρ, kg/m^3	0.075	0.075
	u, m/sec	2670.0	2670.0
	M	2.0	2.0
	γ	1.3133	1.3133
	a, m/sec	1336.0	1336.0
	δ, mm	1.0	1.0
	μ, kg/m-sec	5.5×10^{-5}	5.5×10^{-5}
Oxidant: $0.232O_2 + 0.768N_2$	ρ, kg/m^3	0.175	0.175
	u, m/sec	1814.0	4330.0
	M	2.1	5.25
	γ	1.296	1.296
	a, m/sec	864.3	864.3
	δ, mm	1.0	1.0
	μ, kg/m-sec	6.2×10^{-5}	6.2×10^{-5}
	u_c, m/sec	2150.0	3670.0
	M_c	0.385	0.76

Table 3. Nondimensional Parameters

Parameter	Case 1	Case 2
x_m/θ	64 (100 mm, tanh) 100 (150 mm, tanh) 130 (200 mm, tanh) 1000 (100 mm, b.l.) 1500 (150 mm, b.l.)	64 (100 mm, tanh) 100 (150 mm, tanh) 130 (200 mm, tanh) 1000 (100 mm, b.l.) 1500 (150 mm, b.l.)
Temperature ratio (fuel/oxidant) Pressure ratio (fuel/oxidant) Density ratio (fuel/oxidant) Velocity ratio (fuel/oxidant) Momentum ratio (fuel/oxidant)	1.0 1.0 0.429 1.45 0.90	1.0 1.0 0.429 0.616 0.163
$R_{\delta,\text{fuel}}$ $R_{\delta,\text{air}}$	3640 5120	3640 12220
$R_\theta = \rho_a u_c \theta/\mu, \text{tanh}$ $R_\theta = \rho_a u_c \theta/\mu, \text{b.l.}$	5518 360	11100 630

Table 4. Convective Speeds

M_c	Composition	u_c, m/sec from formula	u_c, m/sec from vortical structures
0.38 tanh	$0.1H_2 + 0.9N_2$	2150	2260 ± 50
0.38, b.l.	$0.1H_2 + 0.9N_2$	2150	2190 ± 30
0.76, tanh	$0.1H_2 + 0.9N_2$	3670	3400 ± 150
0.38, tanh	$0.3H_2 + 0.7N_2$	2543	2648 ± 50

Table 5. Growth Rates

M_c	Fluctuation, percent	$\delta'_u, \delta'_\Omega$	$\delta'_{H_2}, \delta'_\rho$	Mean δ'	δ'/δ'_0
0.38, tanh	3.68 1.84 .92	0.03 ± 0.003 $.05 \pm 0.002$ $.06 \pm 0.020$	0.05 ± 0.002 $.05 \pm 0.002$ $.05 \pm 0.002$	0.05	0.77 to 0.83
0.76, tanh	3.68 1.84 .92	0.075 ± 0.005 $.04 \pm 0.003$ $.04 \pm 0.002$	0.07 ± 0.005 $.04 \pm 0.003$ $.04 \pm 0.005$	0.04	0.45 to 0.50
0.38, b.l.	3.68 .92 .46 .115	0.055 ± 0.002 $.055 \pm 0.005$ $.055 \pm 0.005$ $.055 \pm 0.005$		0.055	0.84 to 0.91

(a) Splitter plate.

[H$_2$, N$_2$, Ar]

(b) Reference 12.

Air

Porous wall

(c) Reference 11.

Air

(d) References 15 and 16.

Figure 1. Various experimental configurations for high-speed shear-layer studies.

20
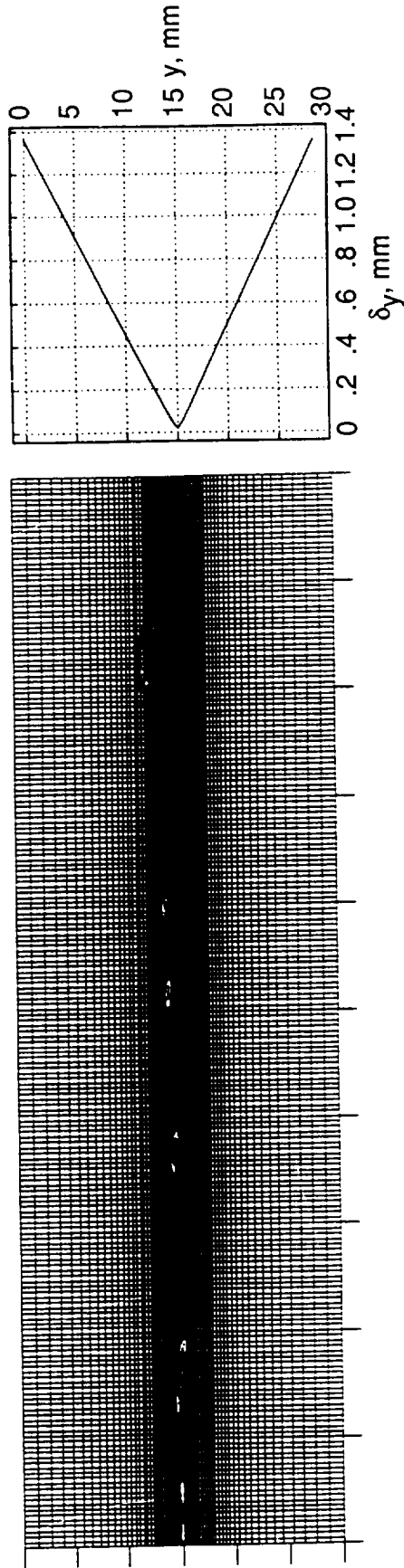
Figure 2. Typical vortical structure and grid distribution. Grid: 201 by 101.
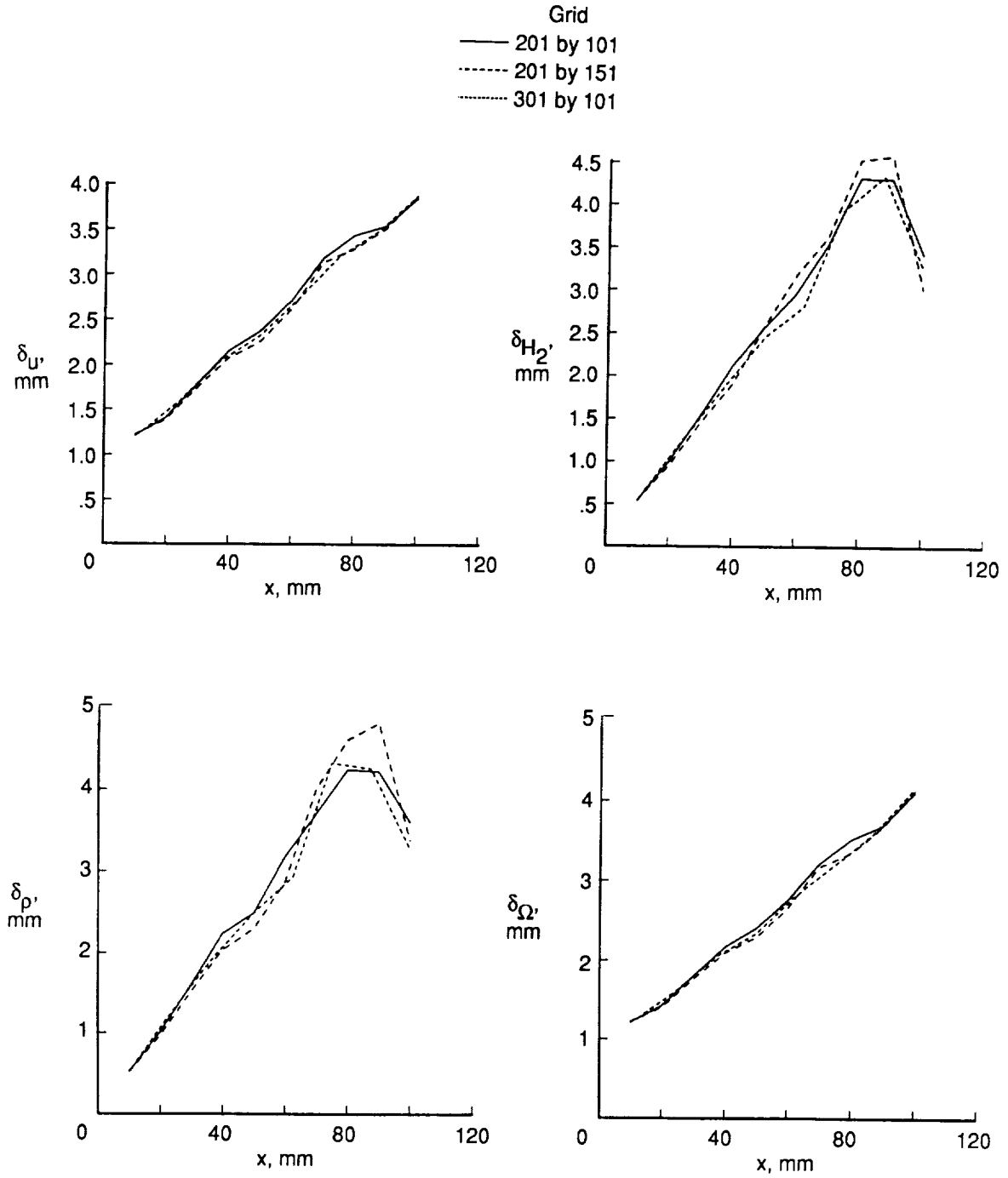
Figure 3. Shear-layer thickness versus x for control (201 by 101 grids), finer y grid, and finer x grid at 3.68 percent fluctuation and $M_c = 0.38$. Domain: 100 mm by 30 mm.
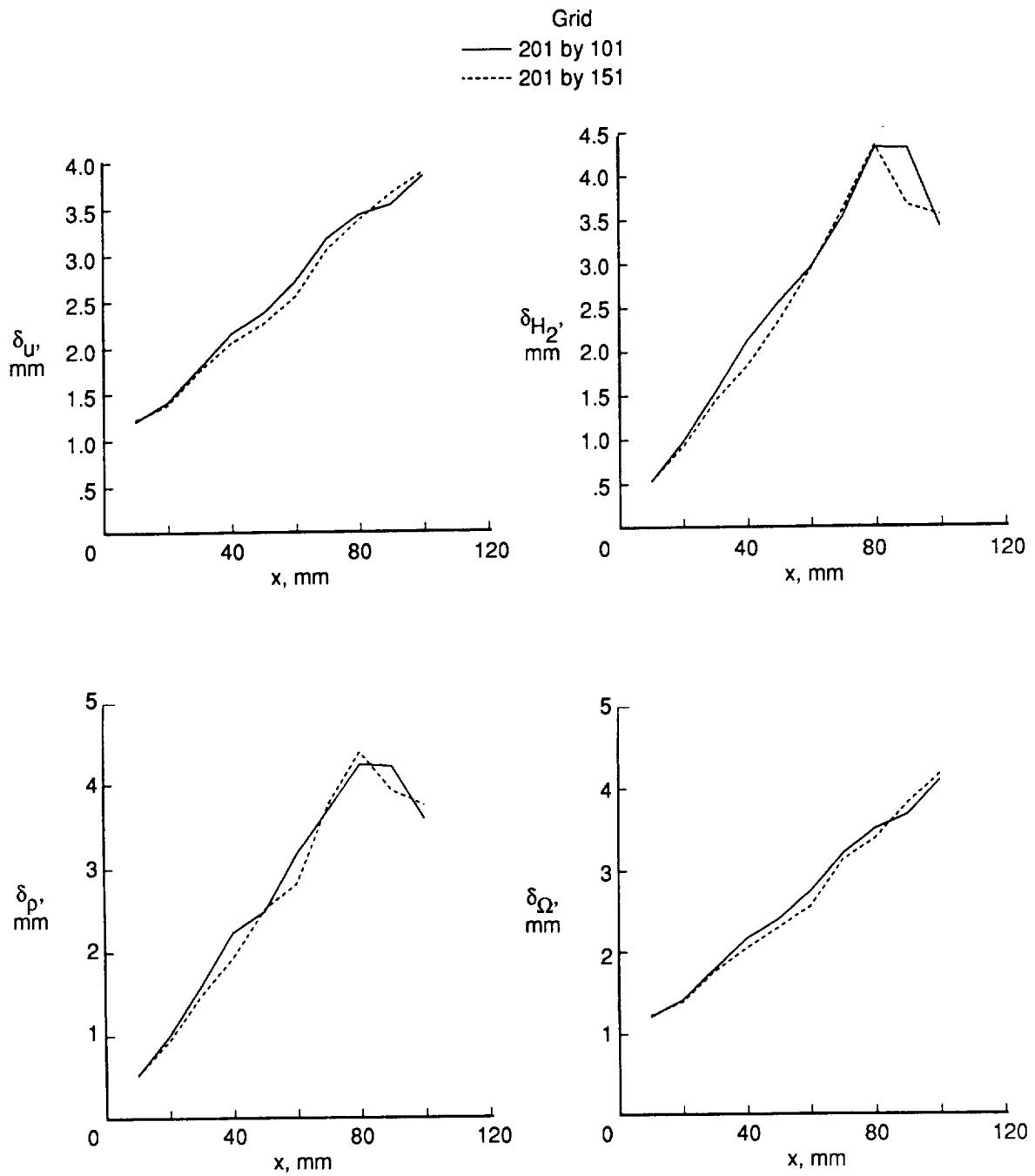
Figure 4. Shear-layer thickness versus x for control (201 by 101 grids) and finer y grid with extended domain at 3.68 percent fluctuation and $M_c = 0.38$.
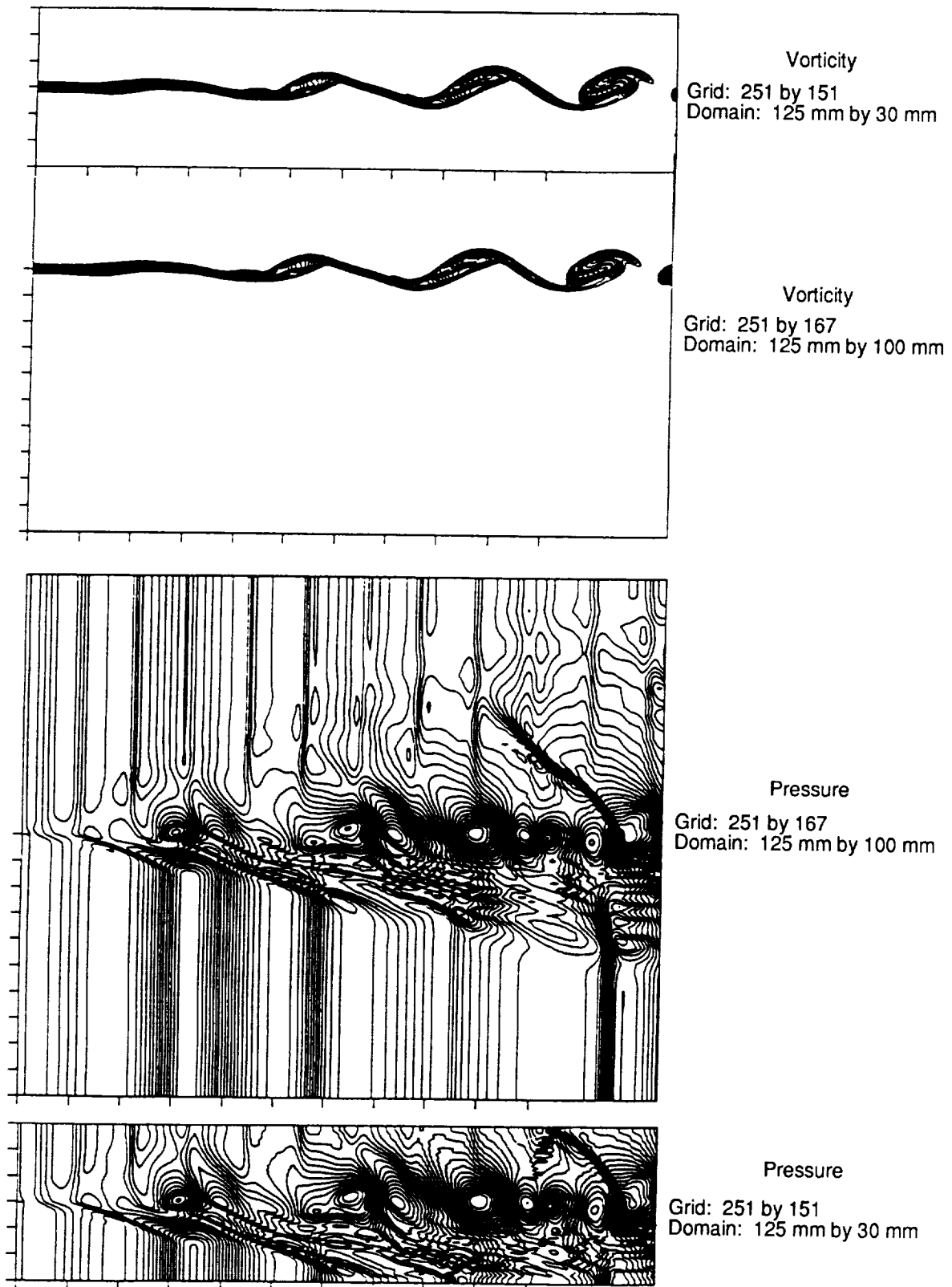
Figure 5. Vorticity and pressure contours on control and extended finer grids at 3.68 percent fluctuation and $M_c = 0.76$.
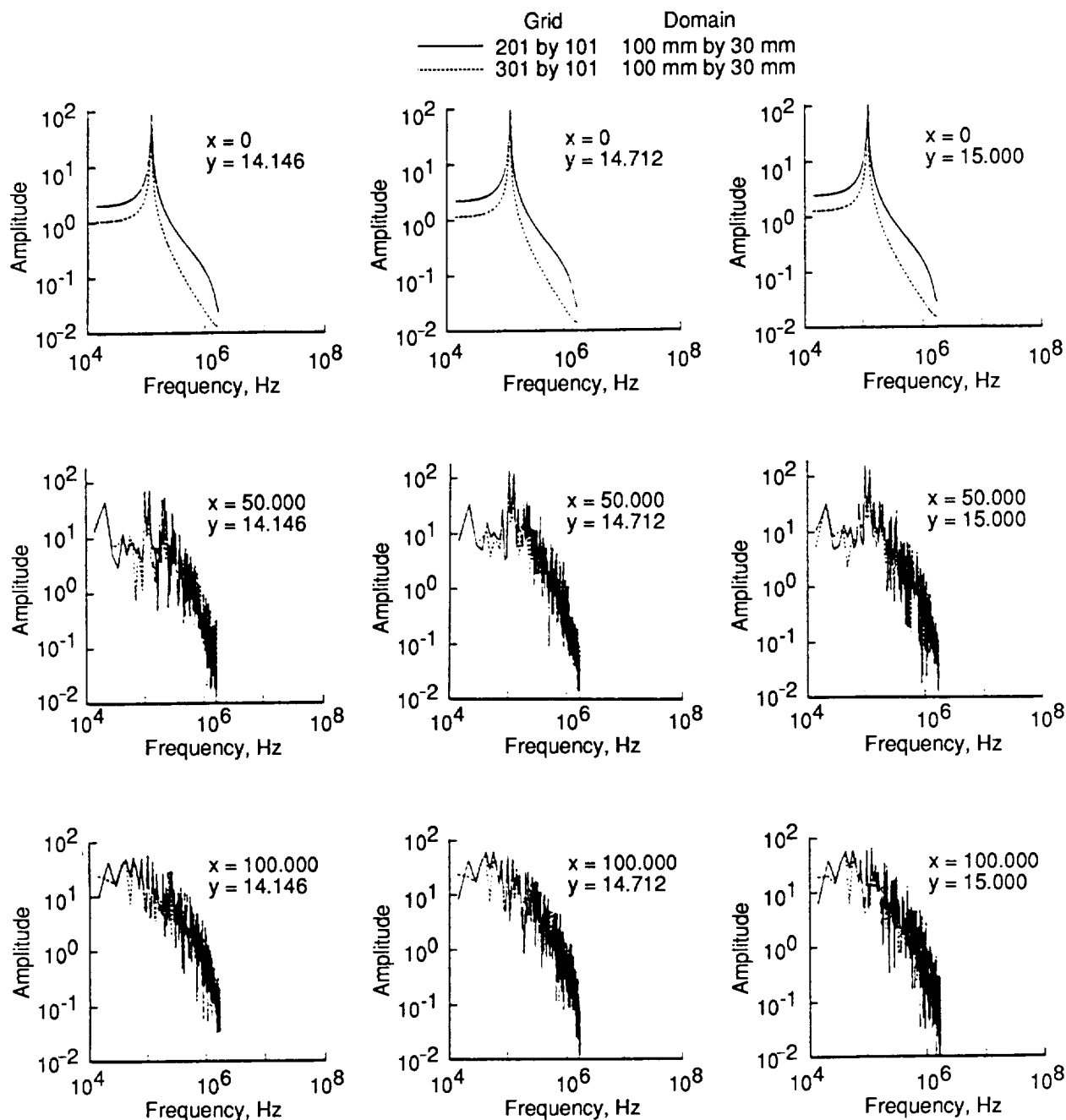
Figure 6. Plot of time spectra for u at three x and y stations for control and finer x grid cases. Amplitude is the square root of the energy of fluctuations.
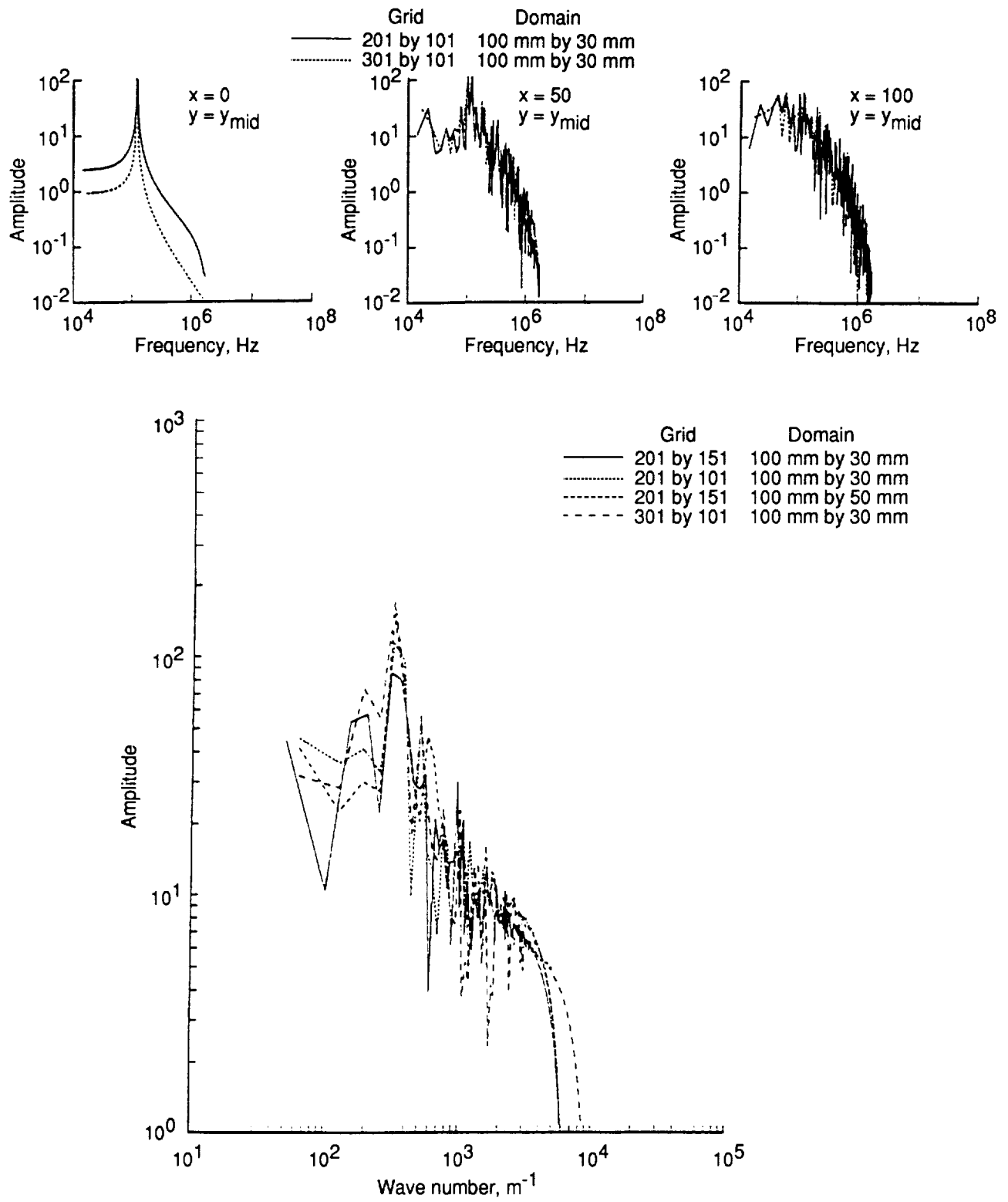
Figure 7. Plot of time spectra at three x stations for u with y grid resolution effect and space spectra for u for all cases at $y = y_{mid} = 15$ mm.
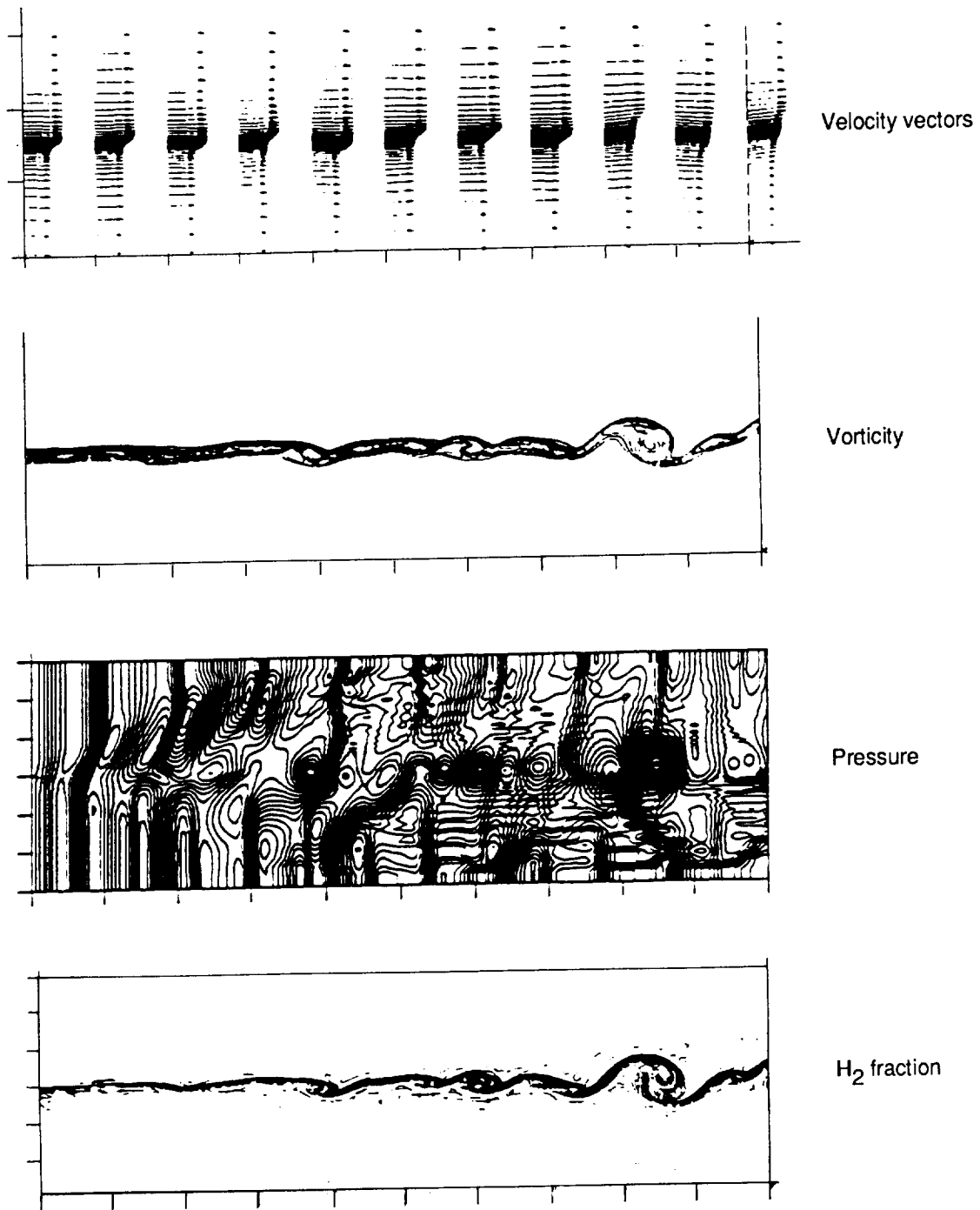
Figure 8. Vector and contour plots of velocity, vorticity, pressure, and H_2 mass fraction (tanh profile) at 3.85 percent fluctuation and $M_c = 0.38$. Grid: 201 by 101; domain: 100 mm by 30 mm.
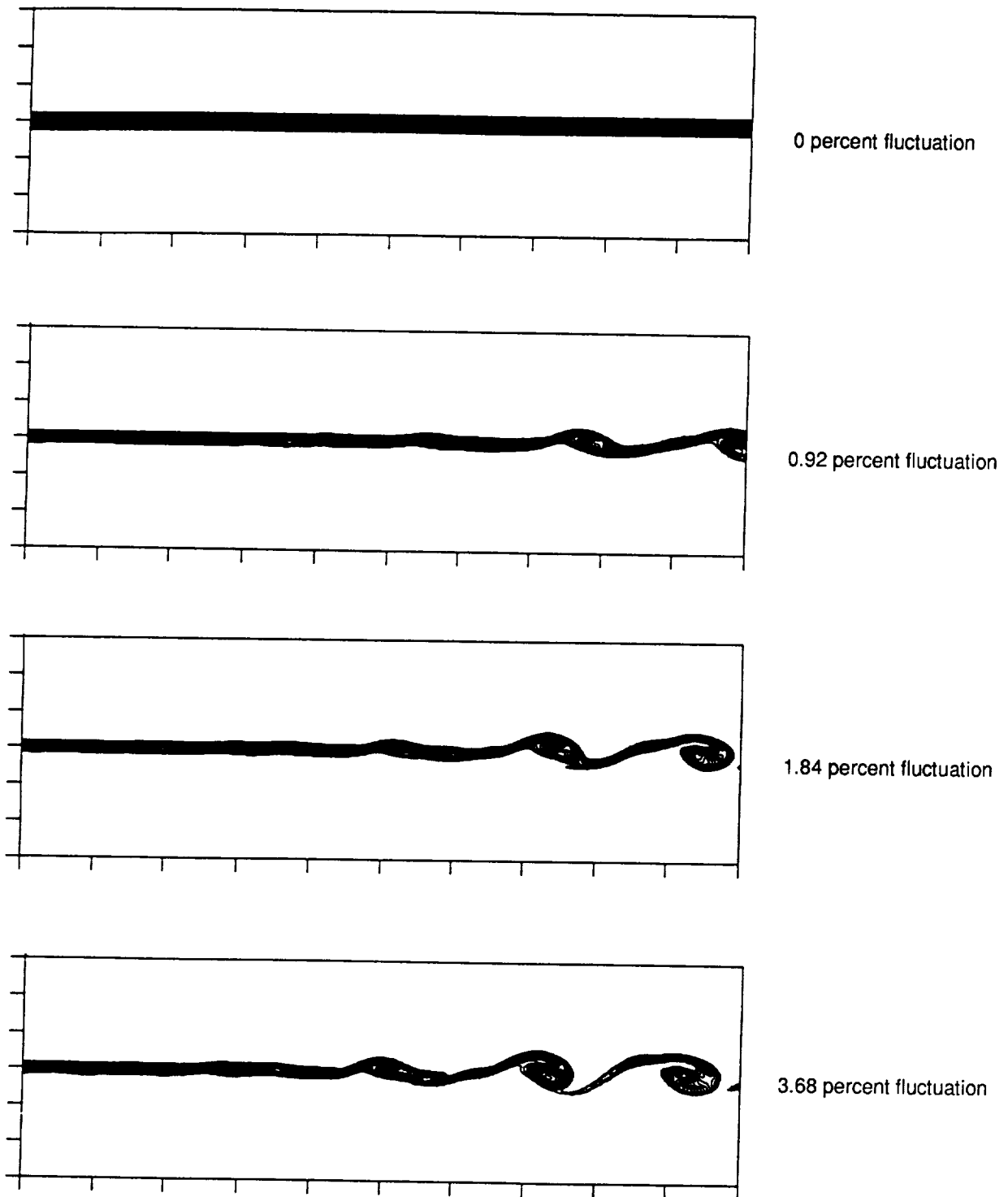
Figure 9. Contour plots of vorticity at various initial-disturbance intensities and $M_c = 0.38$. Grid: 201 by 101; domain: 100 mm by 30 mm.

Velocity vectors

Vorticity

Pressure
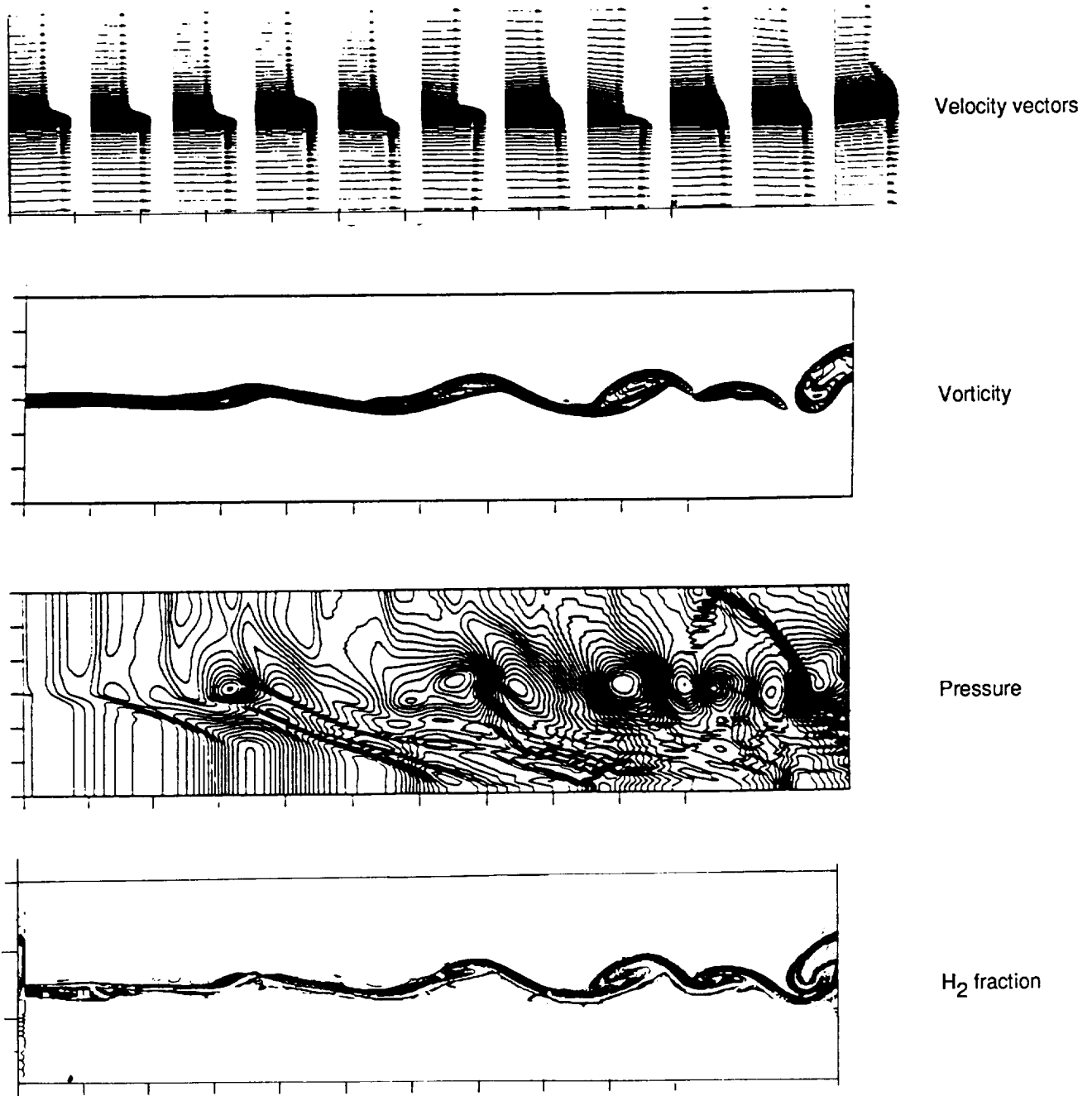
H_2 fraction

Figure 10. Vector and contour plots of velocity, vorticity, pressure, and H_2 mass fraction (tanh profile) at 3.85 percent fluctuation and $M_c = 0.76$. Grid: 251 by 101; domain: 125 mm by 30 mm.
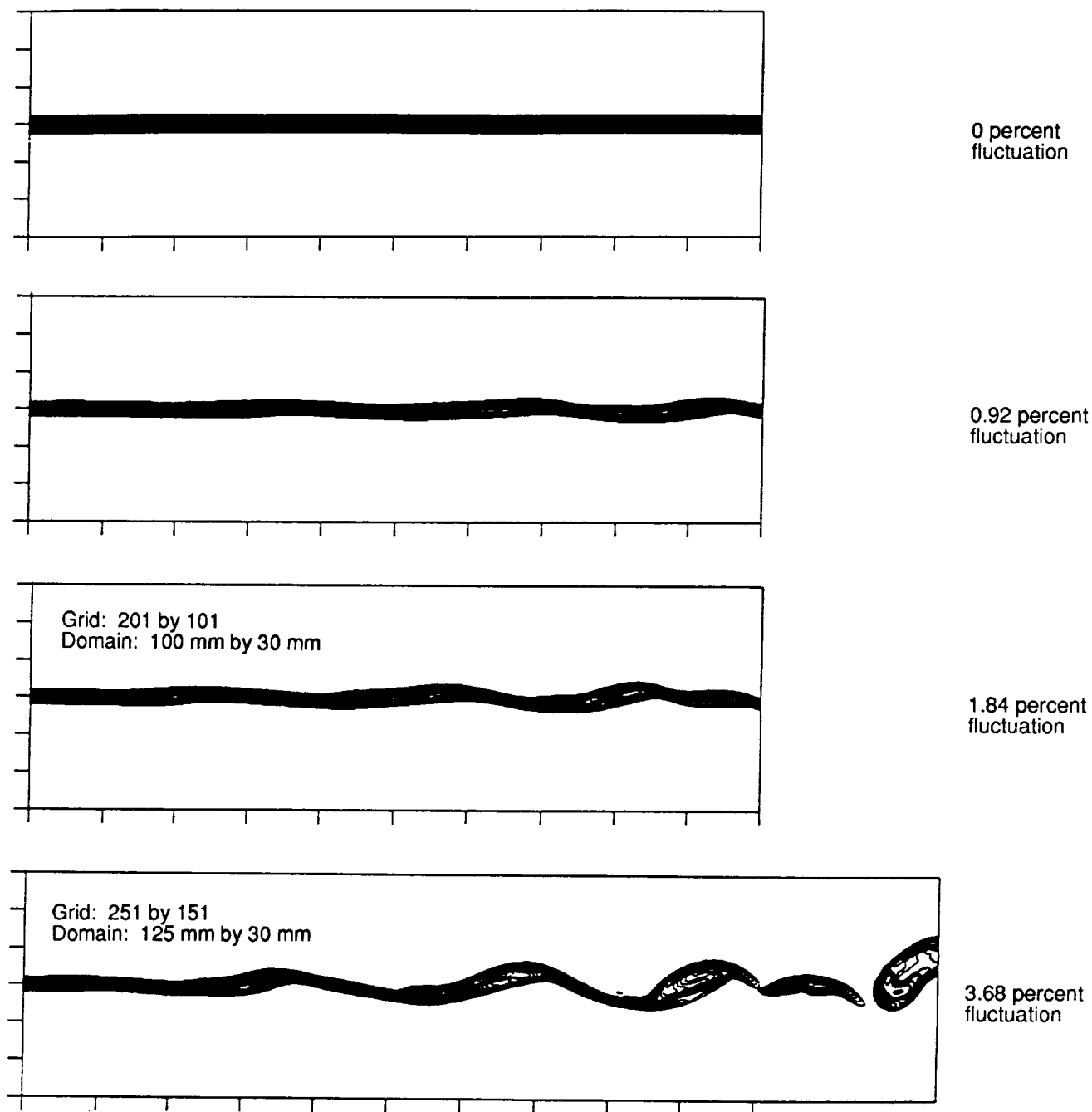
Figure 11. Contour plots of vorticity at various initial-disturbance intensities and $M_c = 0.76$.
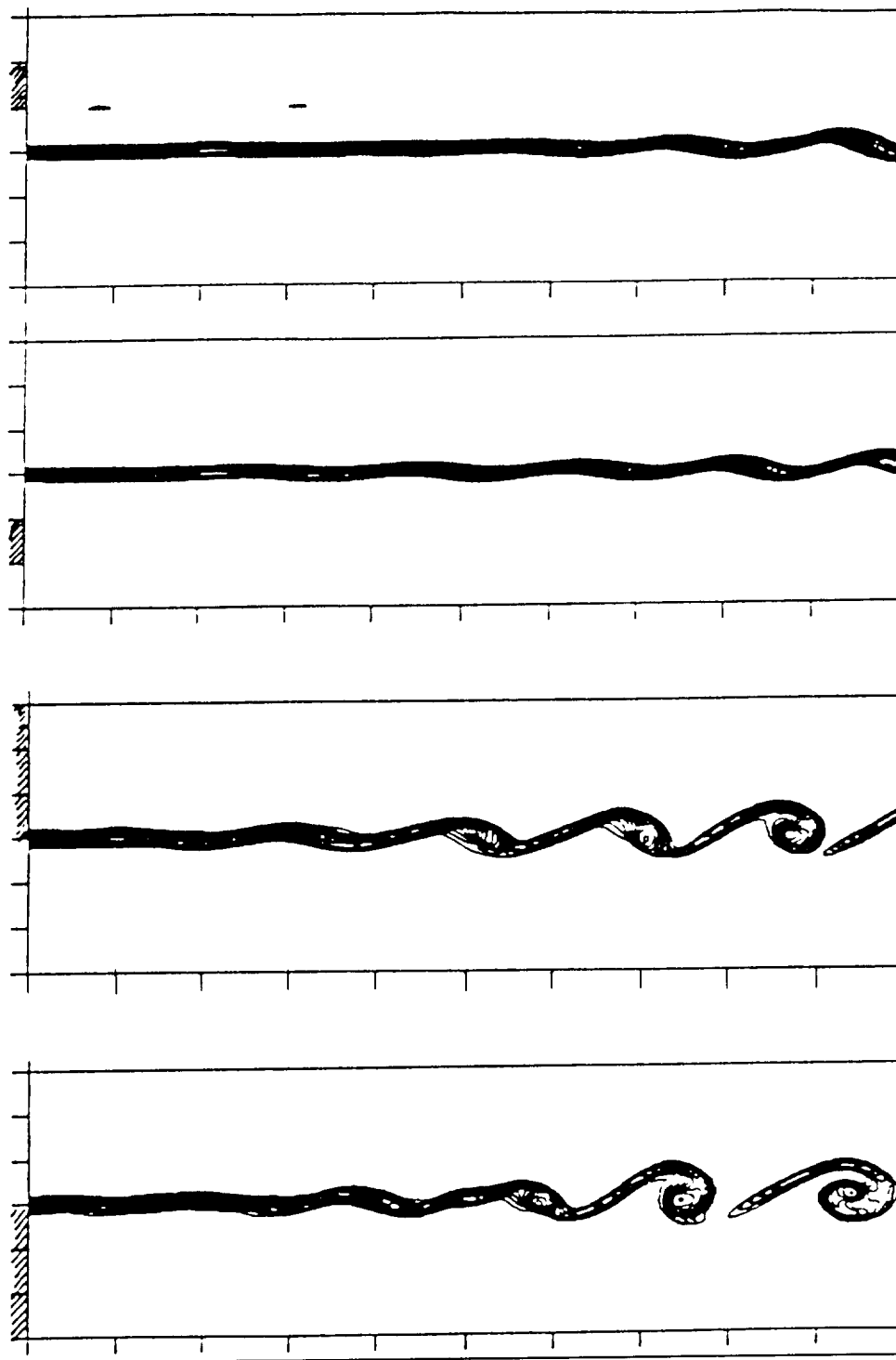
Figure 12. Effect of location of disturbances on vorticity at $x = 0$ on shear growth layer at 3.85 percent fluctuation and $M_c = 0.38$. Grid: 201 by 101; domain: 100 mm by 30 mm.
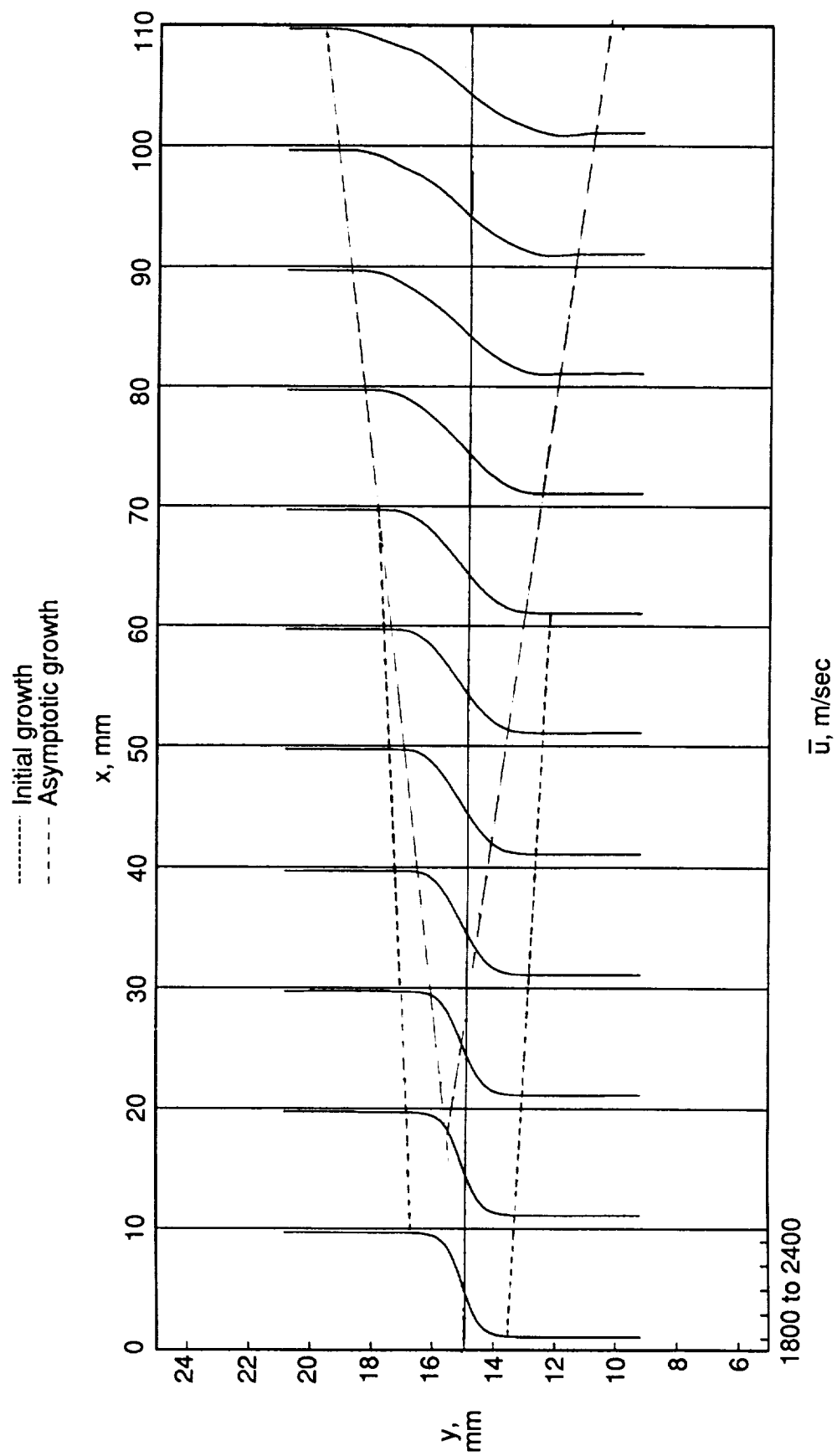
Figure 13. Mean profiles of u versus y with axial distance at $M_c = 0.38$.
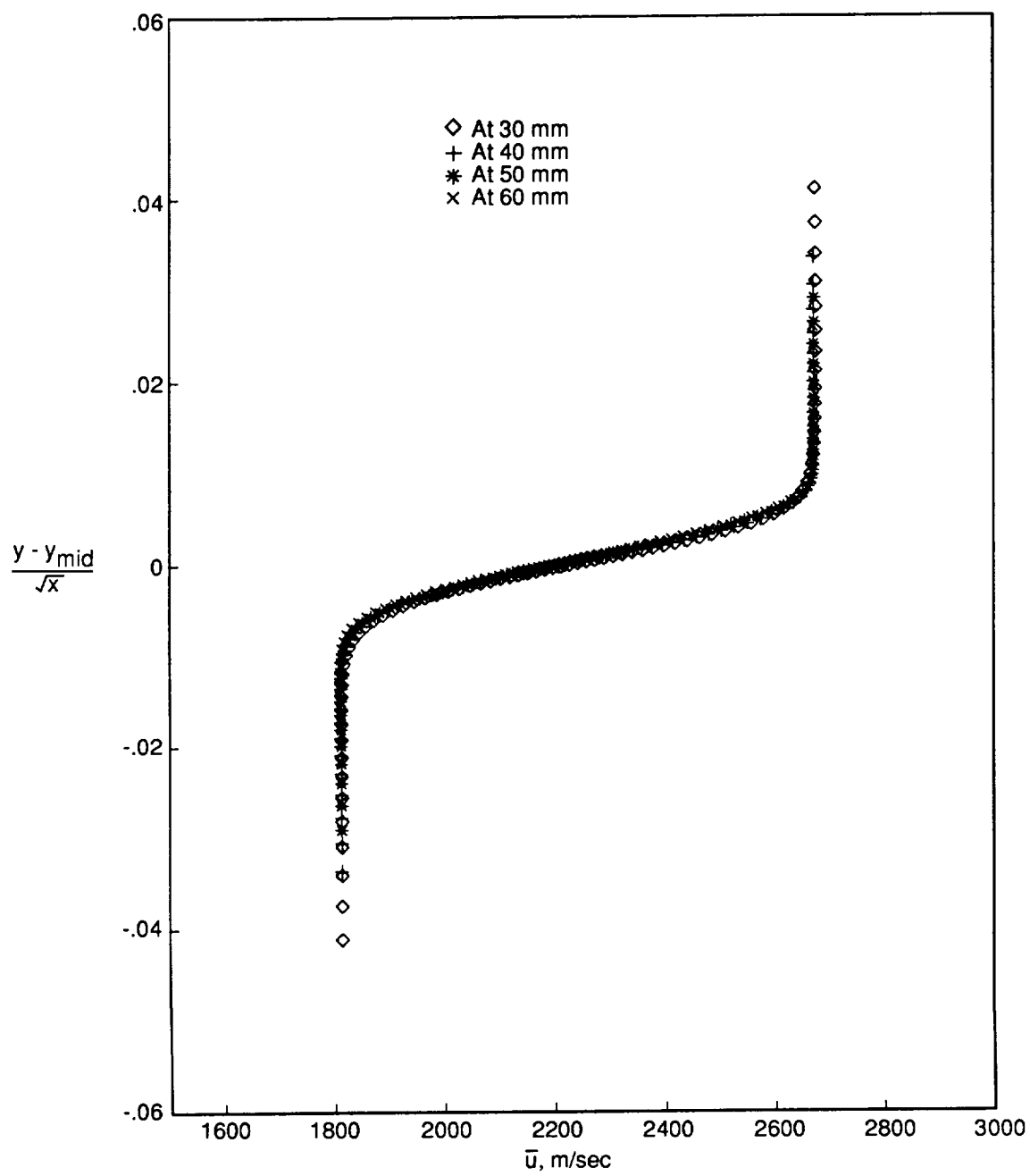
Figure 14. Profiles of figure 13 on a laminar similarity plot for $x = 30$ to 60 mm. Domain: 100 mm by 30 mm; $y_{mid} = 15$ mm.
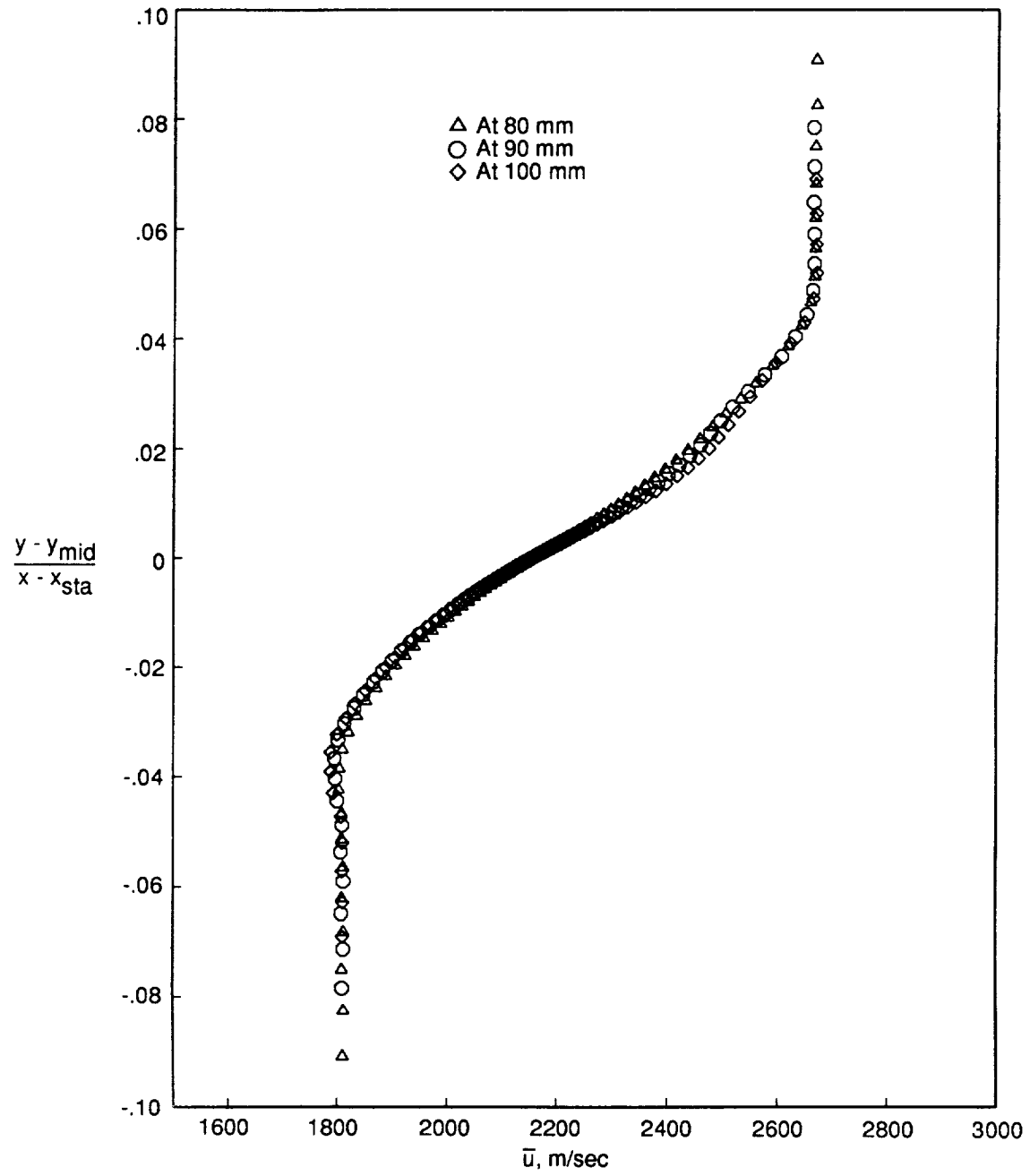
Figure 15. Profiles of figure 13 on a turbulent similarity plot for $x = 80$ to 100 mm. Domain: 100 mm by 30 mm; x station $(x_{\mathrm{sta}}) = 16$ mm; $y_{\mathrm{mid}} = 15$ mm.
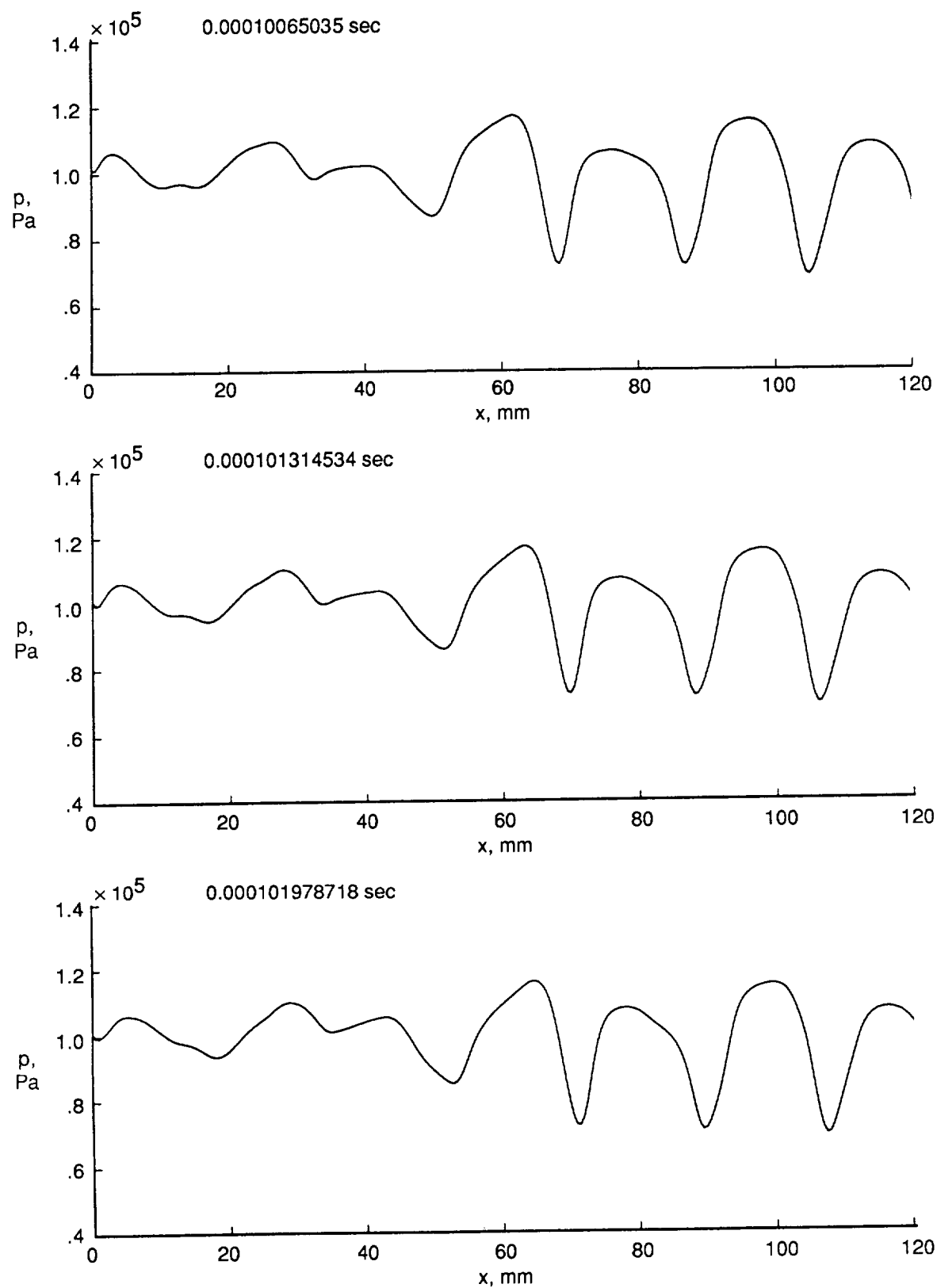
Figure 16. Plots of pressure versus x at three successive times for $M_c = 0.38$ and no fluctuation.
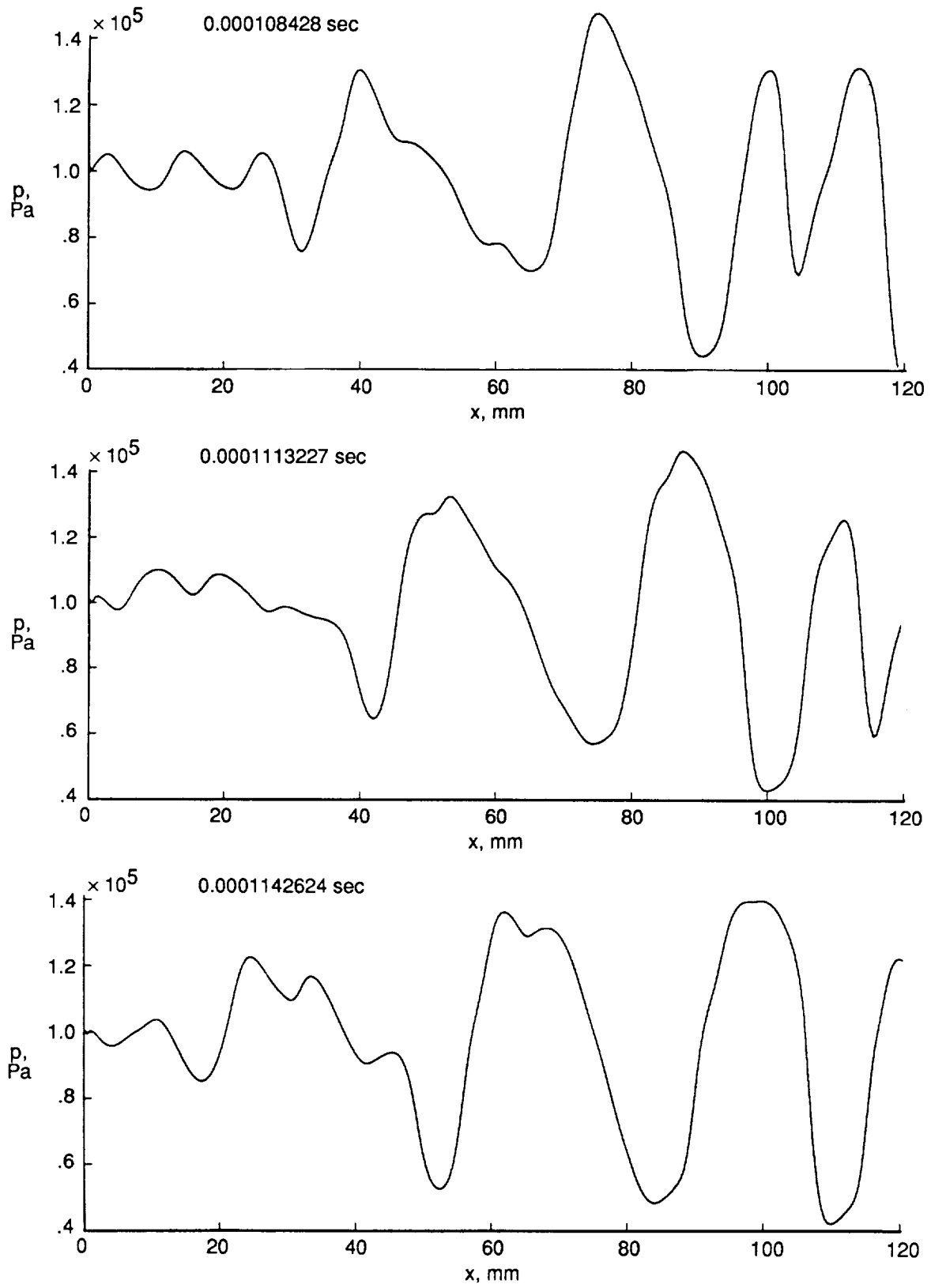
Figure 17. Plots of pressure versus x at three successive times for $M_c = 0.76$ and no fluctuation.
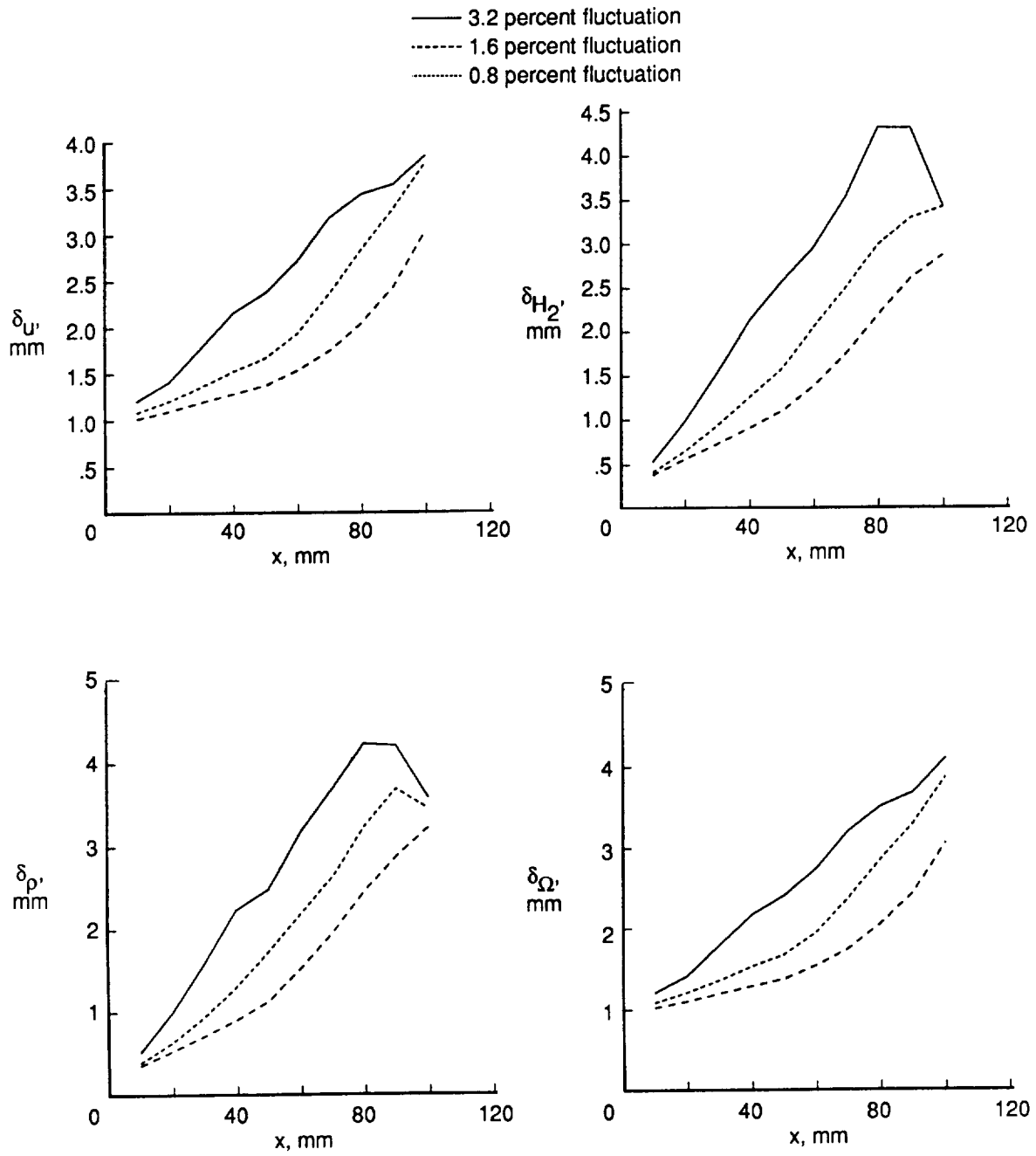
Figure 18. Shear-layer growth as a function of intensity of initial fluctuations for $M_c = 0.38$. Grid: 201 mm by 101 mm; domain: 100 mm by 30 mm.

Grid	Domain	Fluctuation, percent
201 by 151	100 mm by 30 mm	3.68
301 by 101	200 mm by 30 mm	1.84
301 by 101	200 mm by 30 mm	0.92
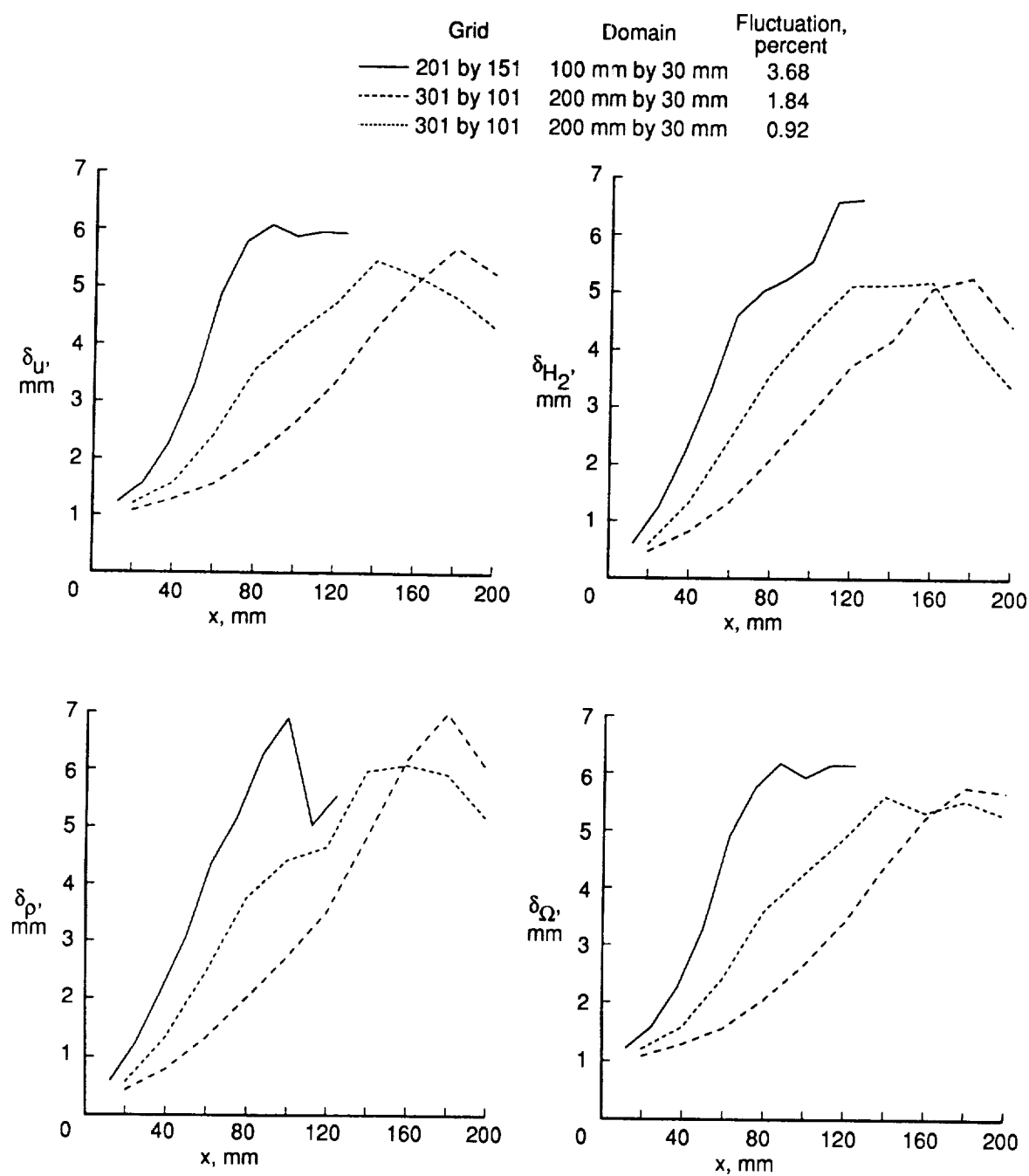
Figure 19. Shear-layer growth as a function of intensity of initial fluctuations for $M_c = 0.76$.
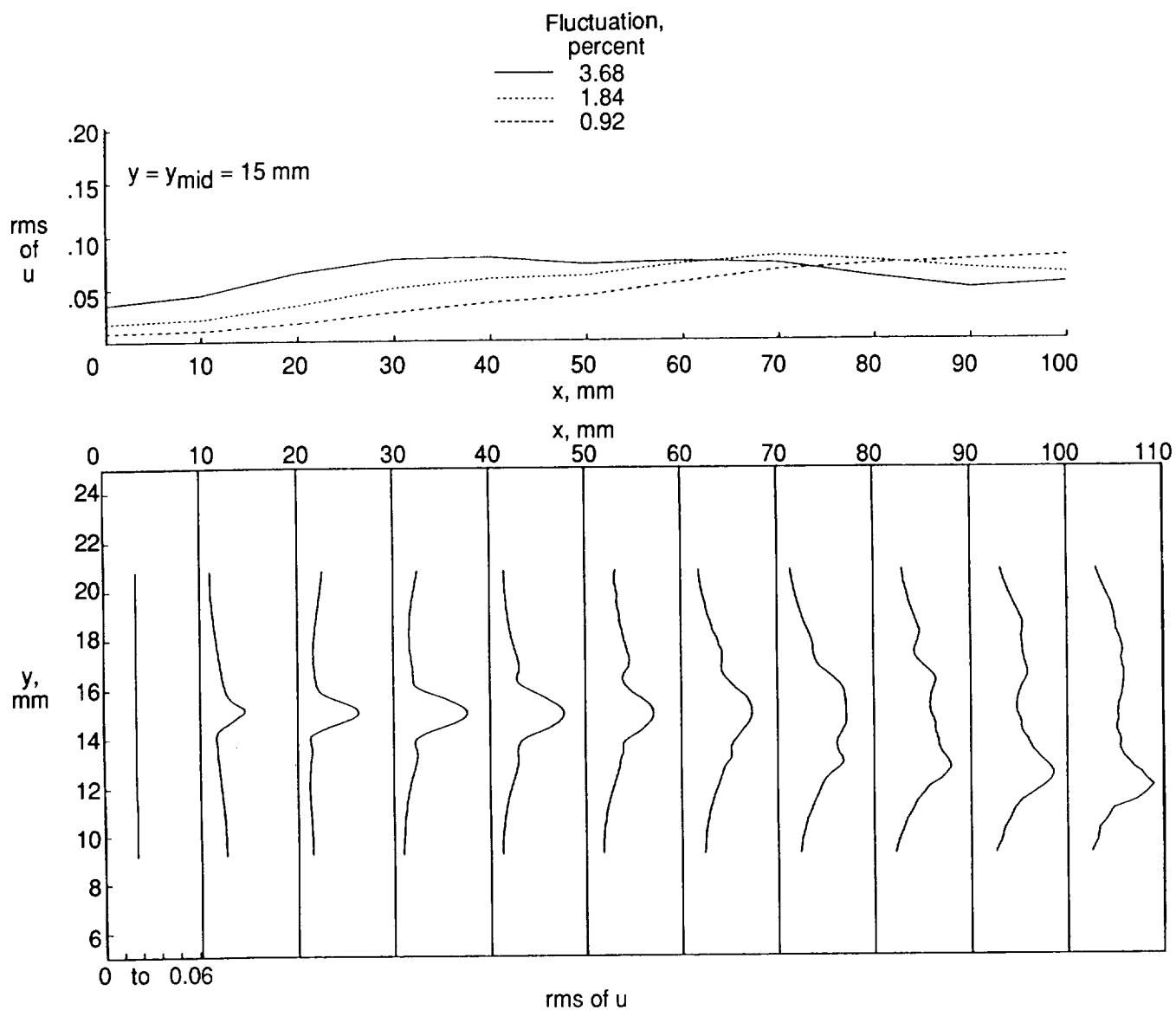
Figure 20. Distribution of rms of u as a function of x and y at $M_c = 0.38$. Grid: 201 by 101; domain: 100 mm by 30 mm; initial profile: tanh.
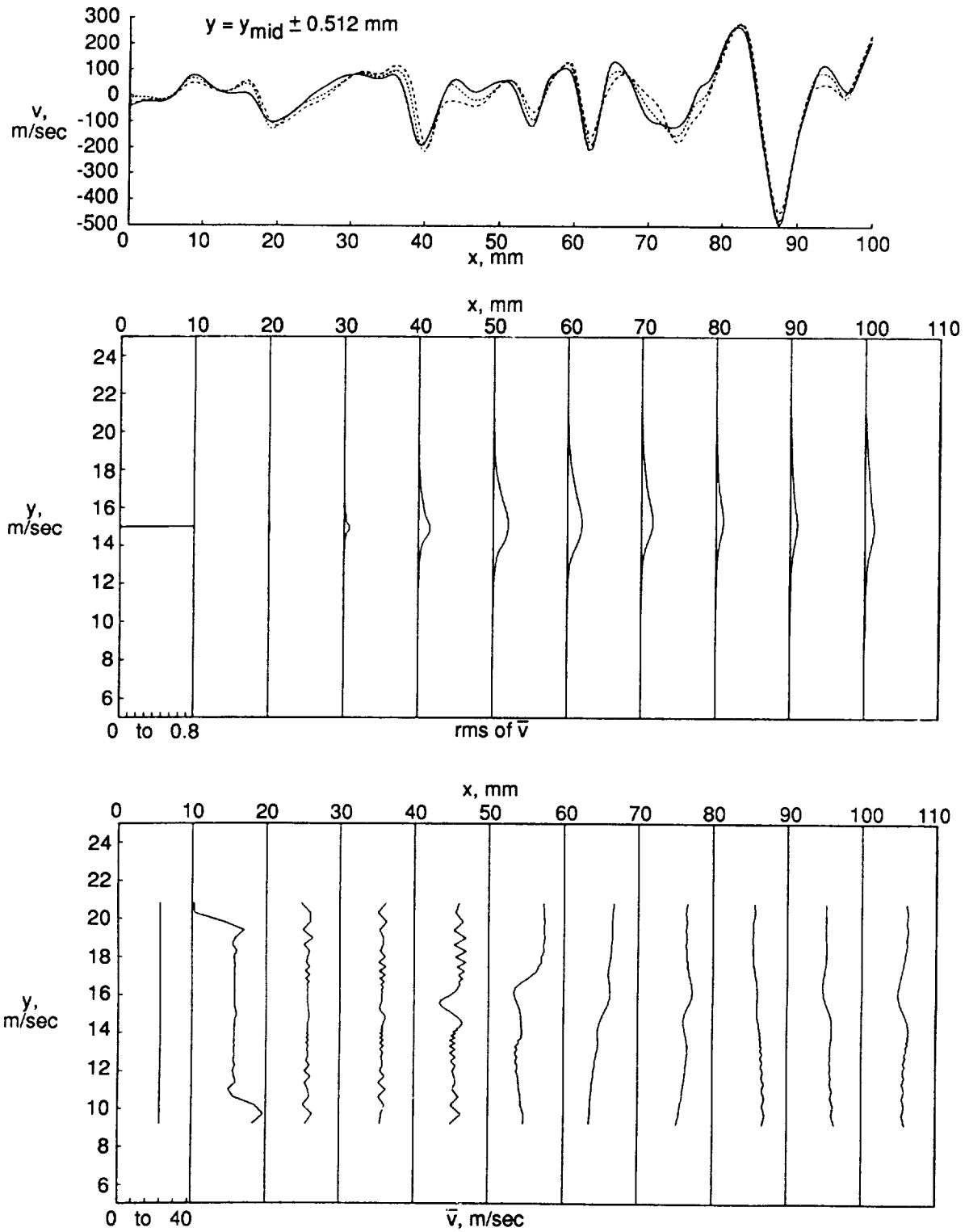
Figure 21. Instantaneous v at three fixed values of y and mean rms v as a function of x and y for 3.68 percent fluctuation and $M_c = 0.38$. Grid: 201 by 101; domain: 100 mm by 30 mm; initial profile: tanh.
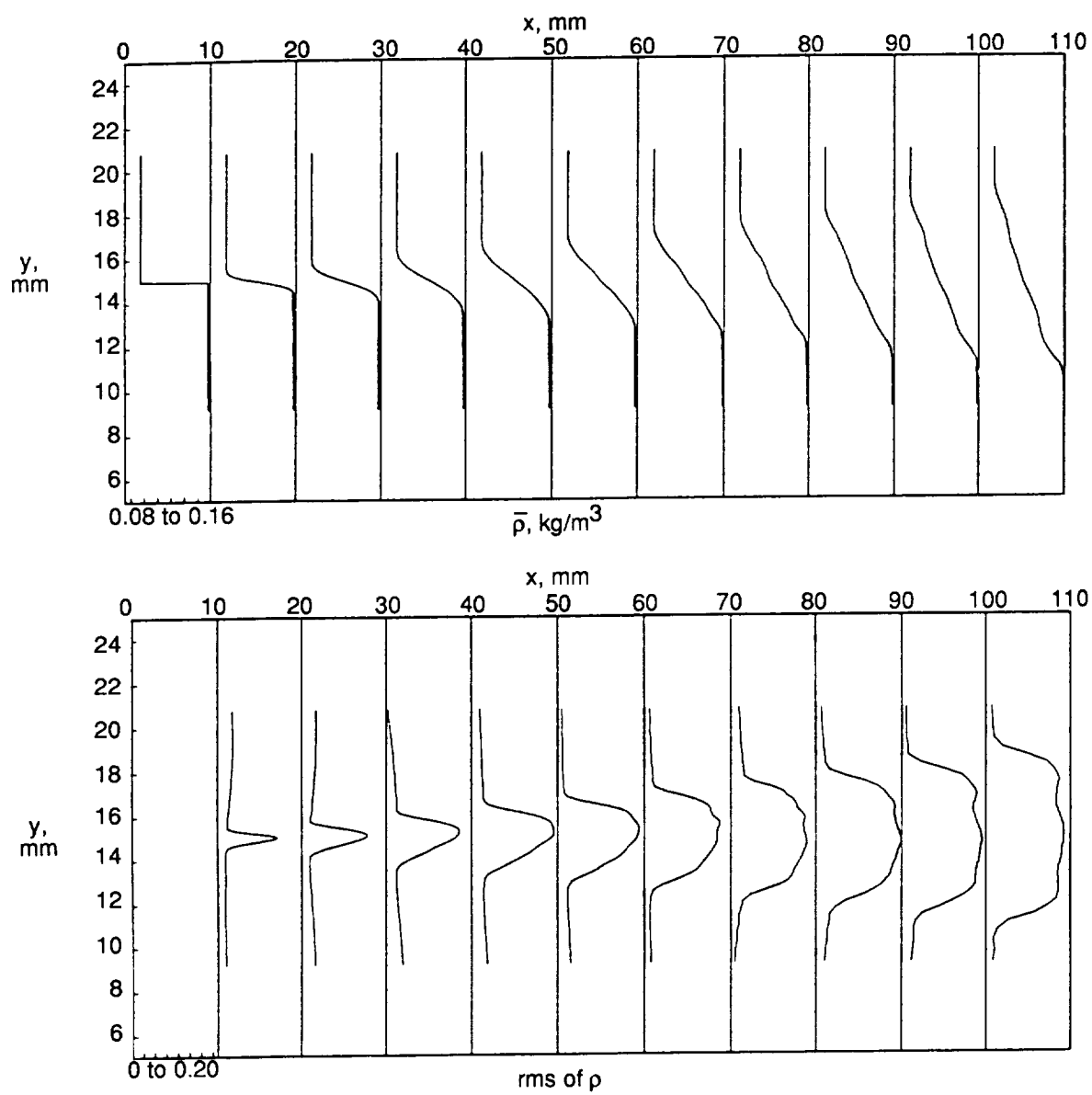
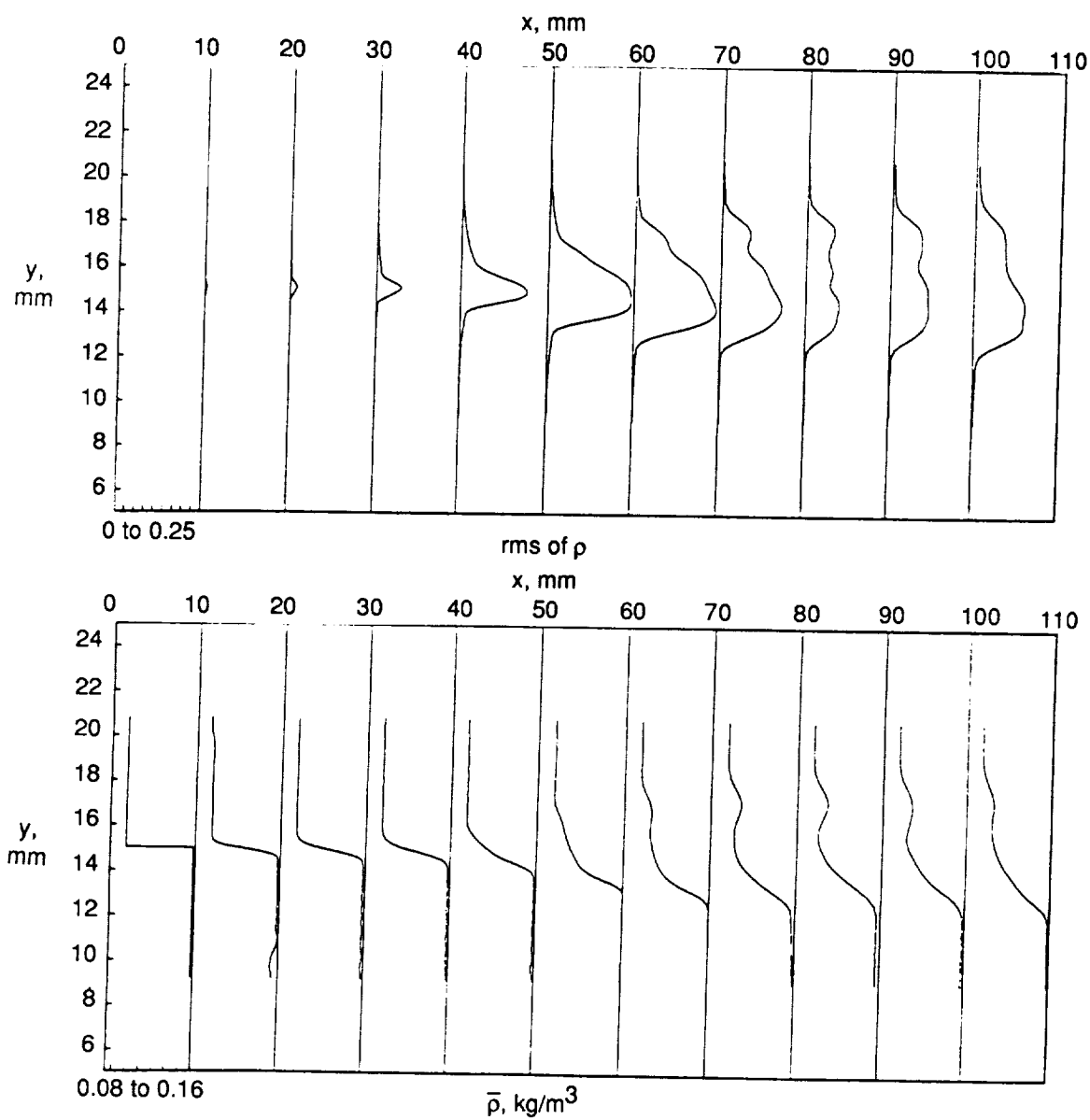Figure 22. Mean and rms values of ρ as a function of x and y for 3.68 percent fluctuation.
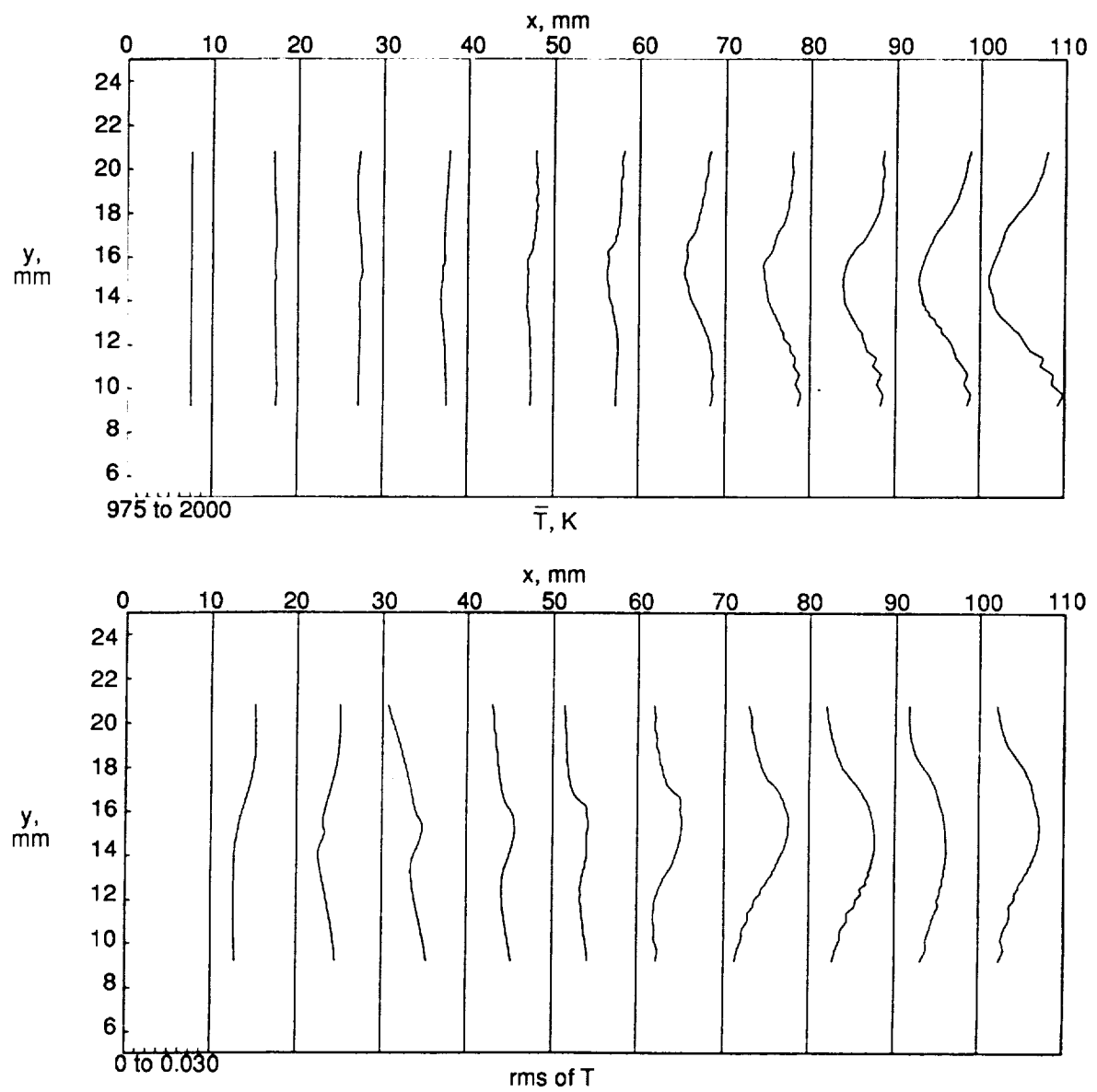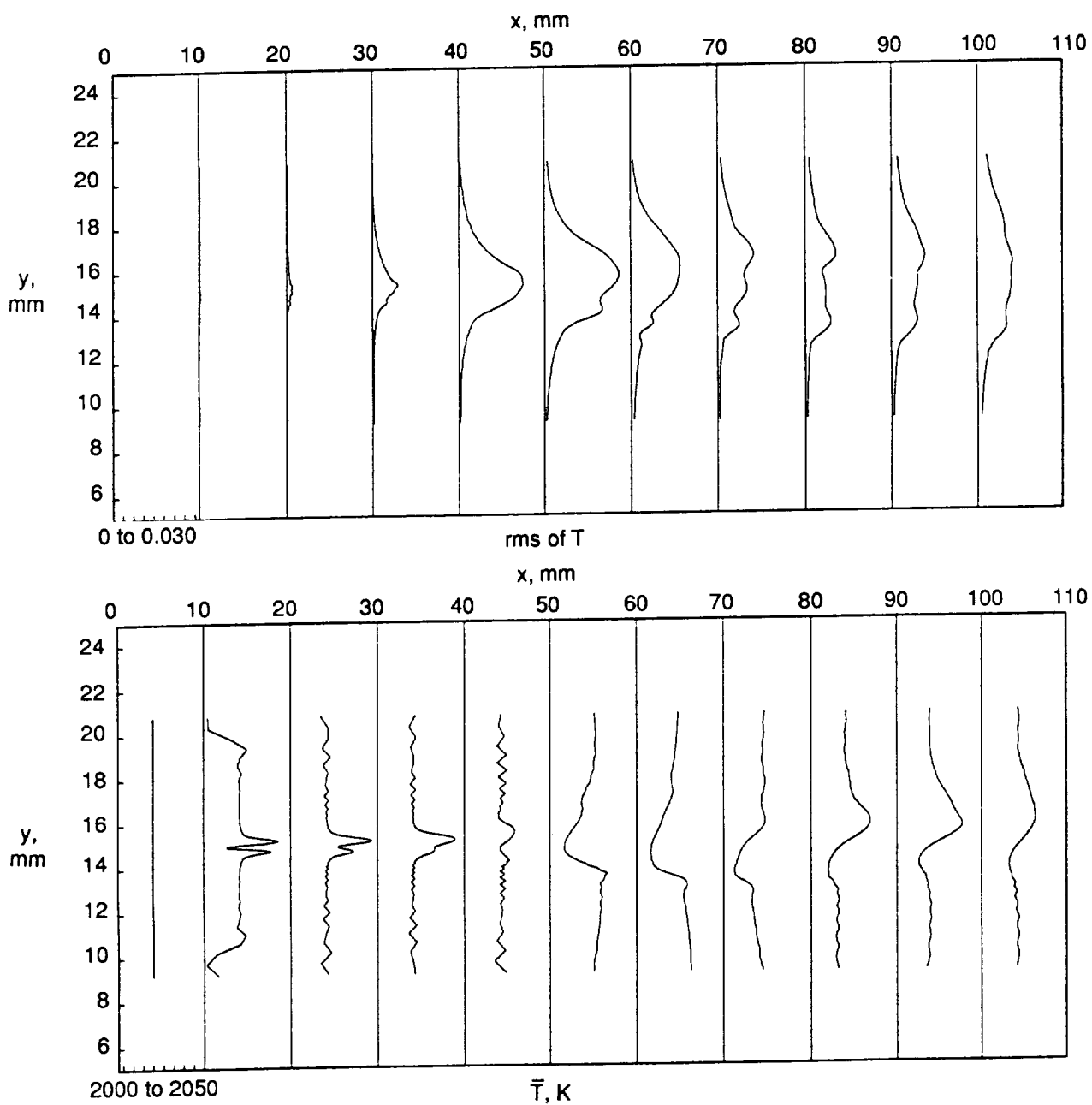
Figure 23. Mean and rms values of T as a function of x and y for 3.68 percent fluctuation.
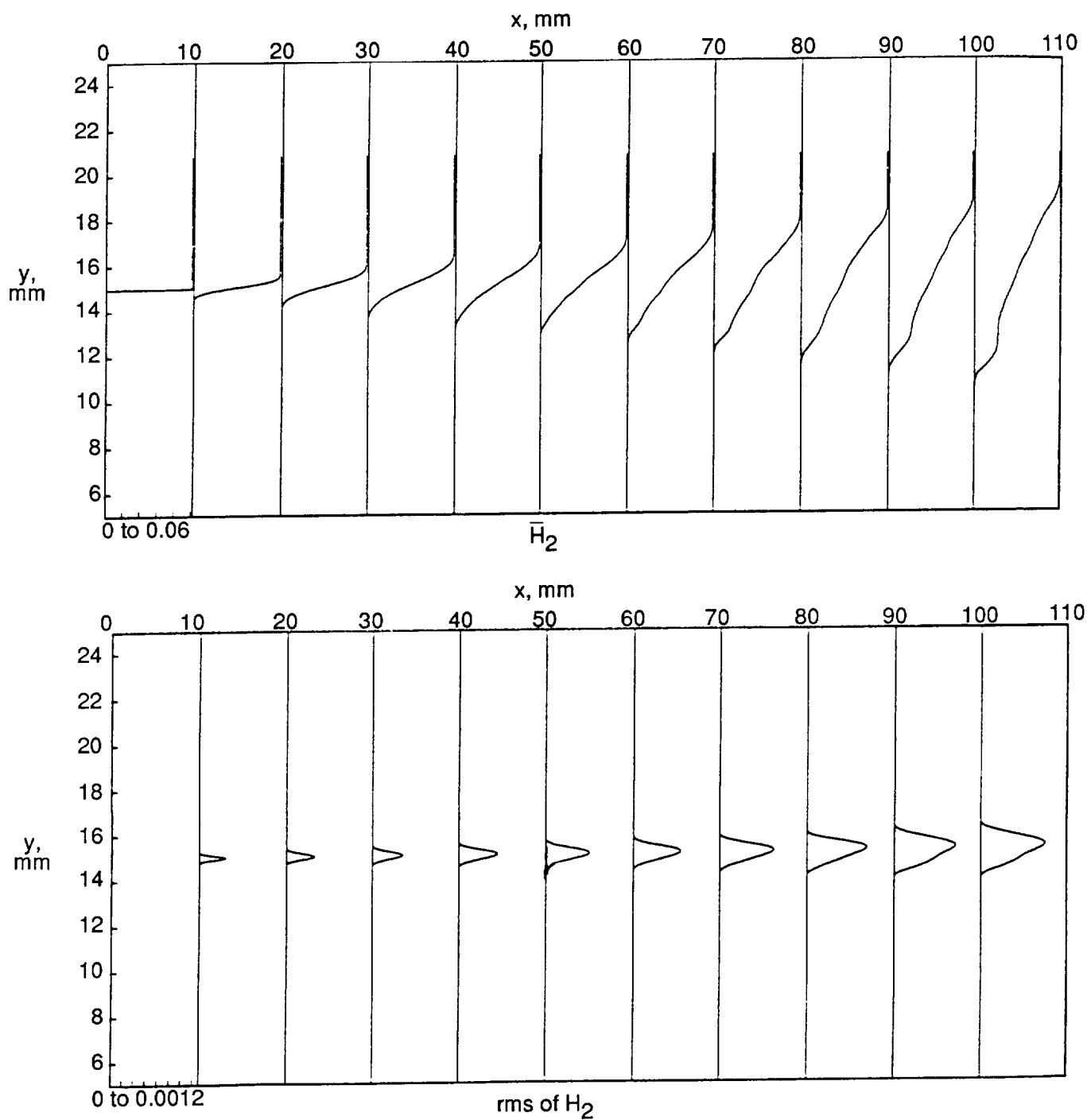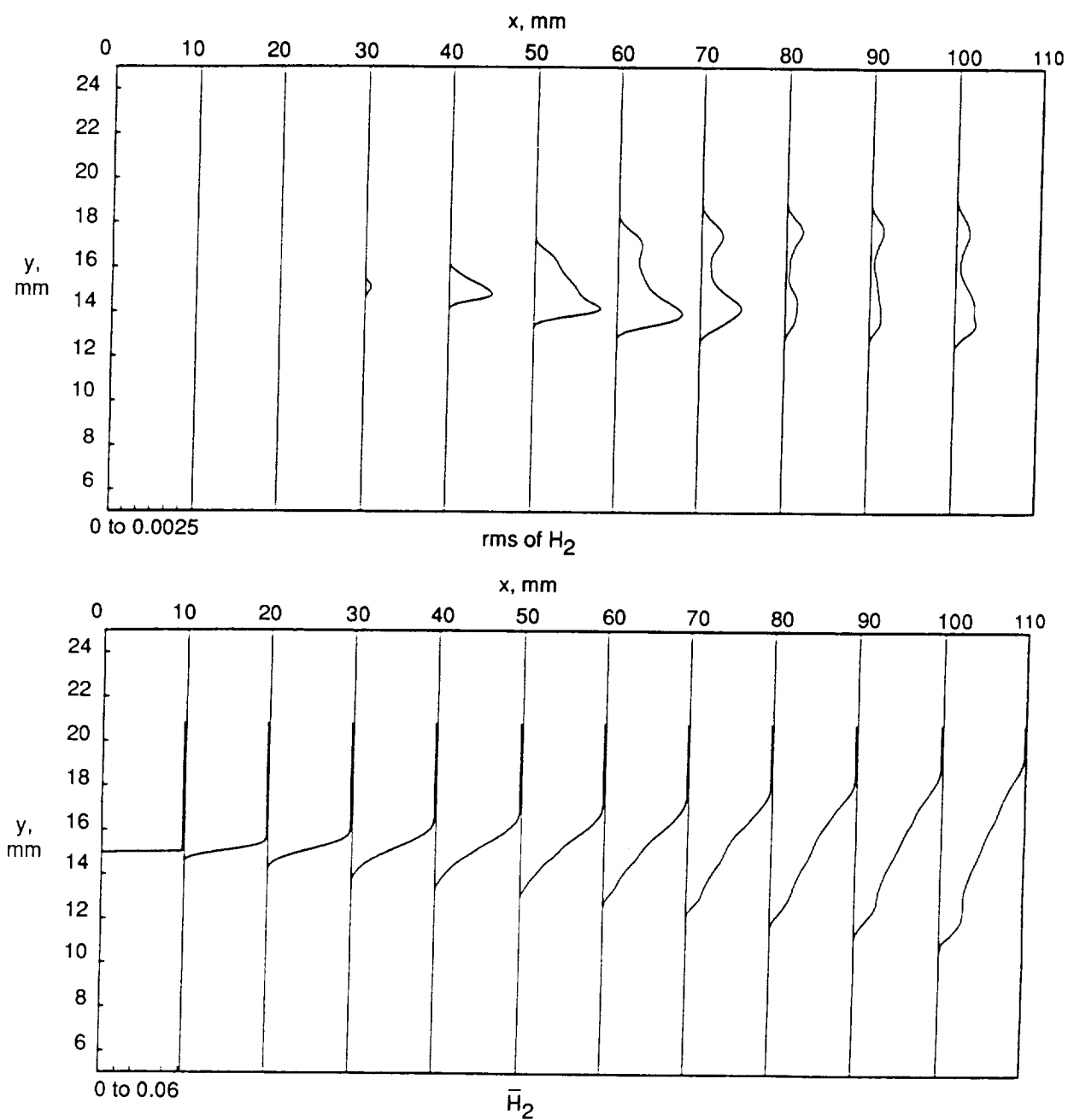
Figure 24. Mean and rms values of H_2 mass fraction as a function of x and y for 3.68 percent fluctuation.
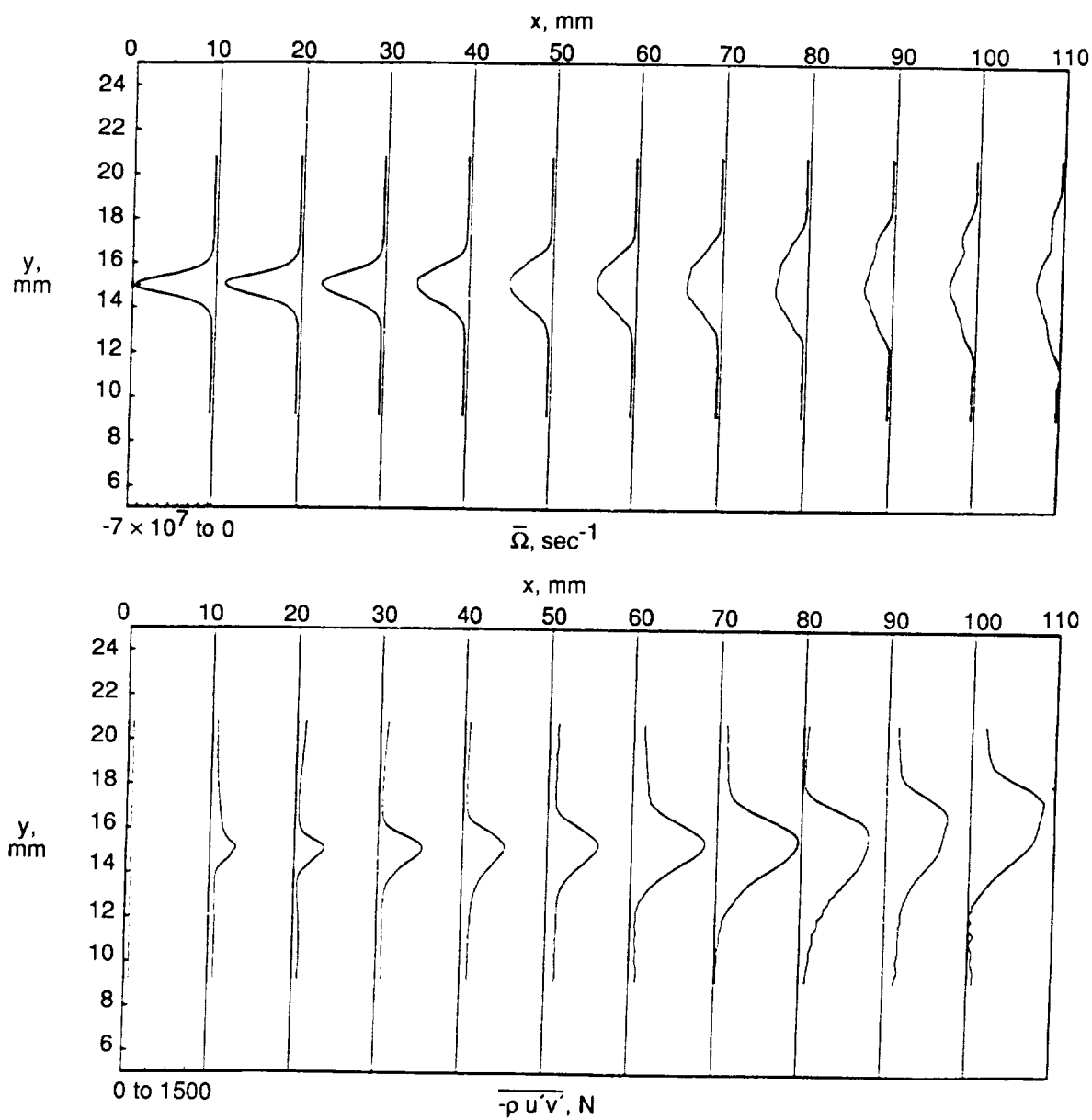
Figure 25. Mean vorticity and Reynolds shear stress as a function of x and y for 3.68 percent fluctuation.

44
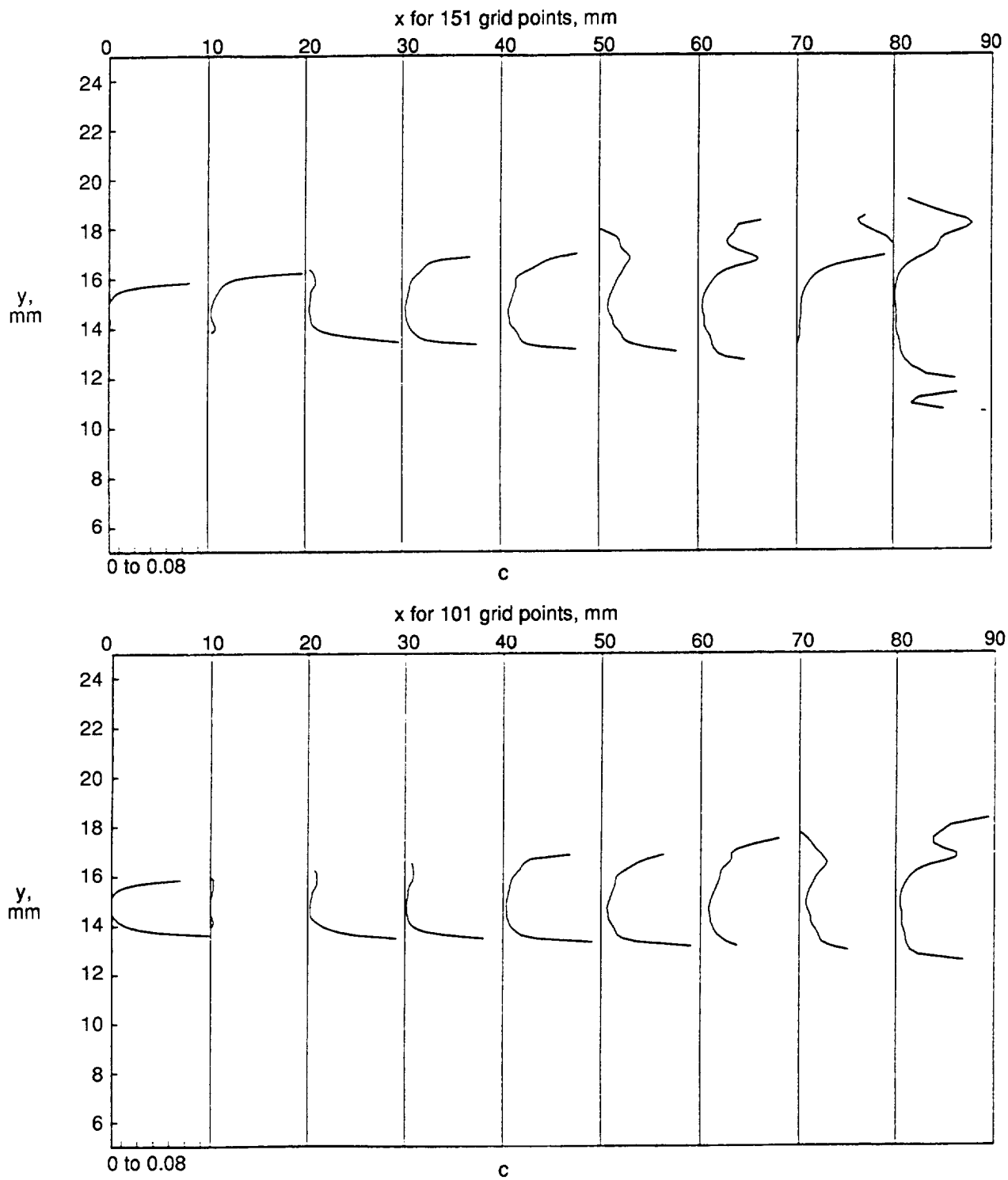
Figure 26. Plot of $c = -\overline{\rho u'v'} \big/ \left[\rho_m \left(\delta_\Omega \Omega_m^2 \right) \right]$ as a function of x and y.

0 percent fluctuation

0.115 percent fluctuation

0.46 percent fluctuation

0.92 percent fluctuation

3.68 percent fluctuation
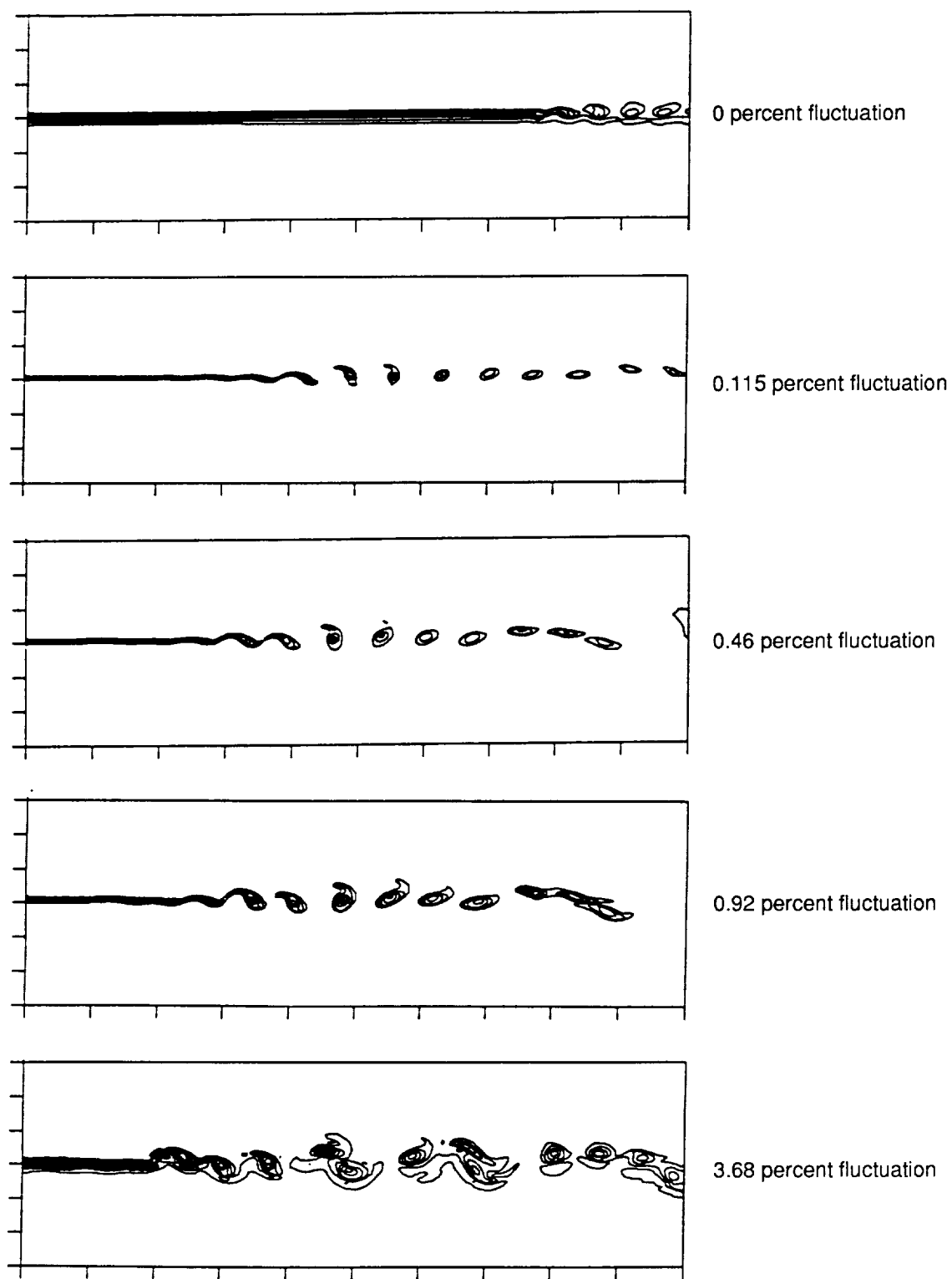
Figure 27. Vorticity contour plot for boundary-layer case at various fluctuation intensities and $M_c = 0.38$.
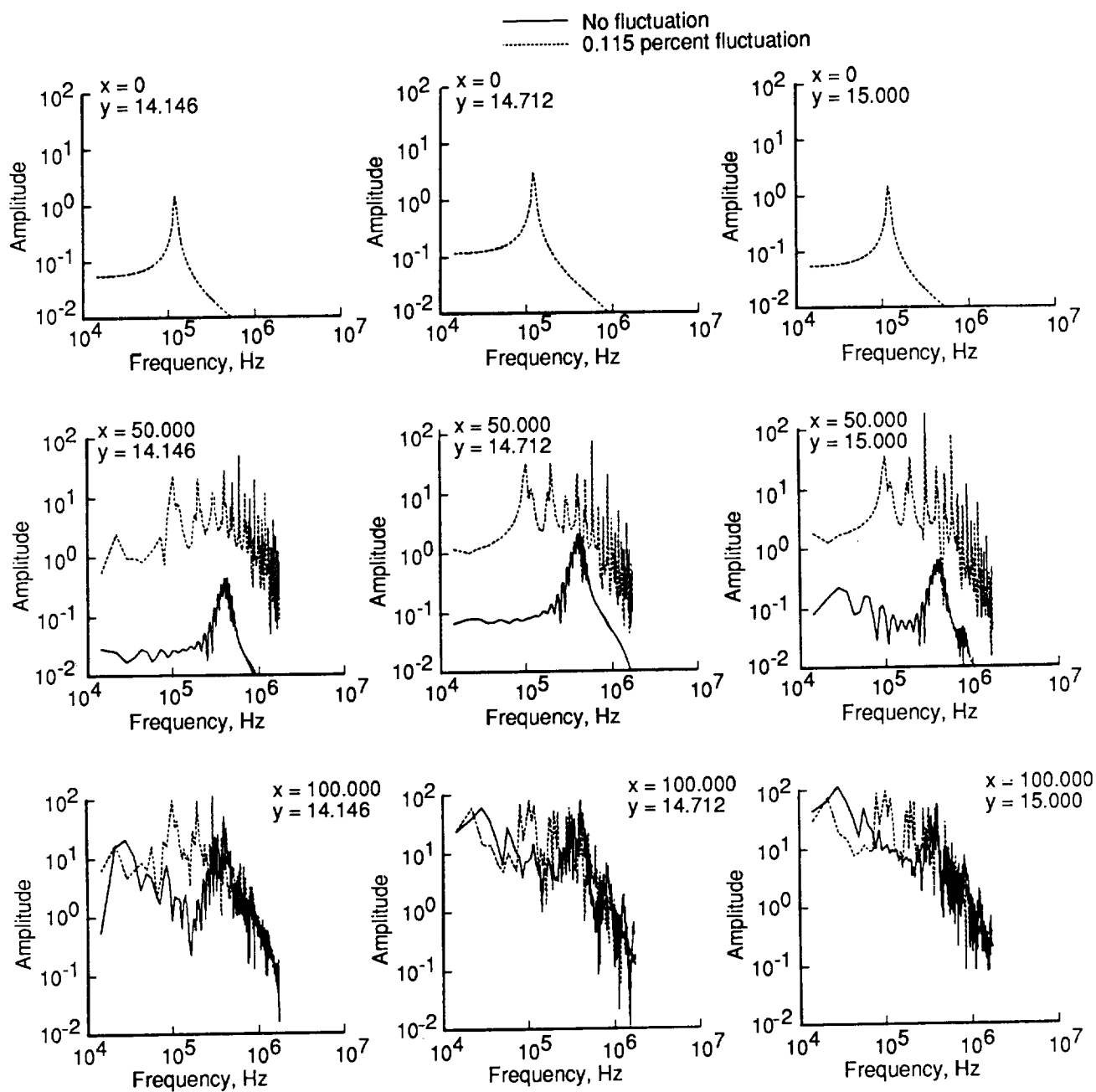
Figure 28. Plots of time spectra for u at three y stations for no fluctuation and 0.115 percent fluctuation. Grid: 201 by 101; domain: 100 mm by 30 mm; initial profile: boundary layer.
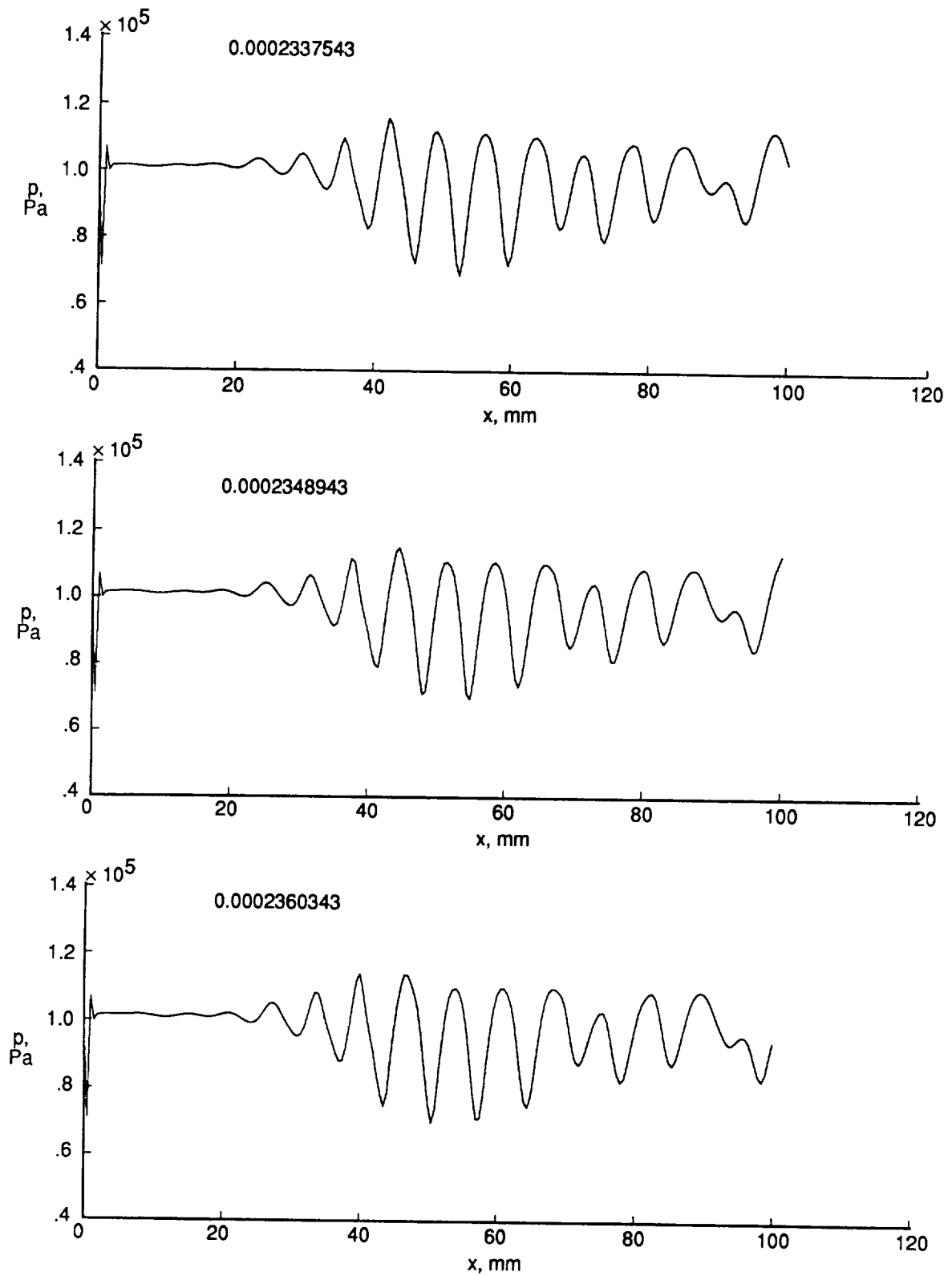
Figure 29. Plots of pressure versus x at three successive times for $M_c = 0.38$ and 0.115 percent fluctuation. Boundary-layer inflow profile.
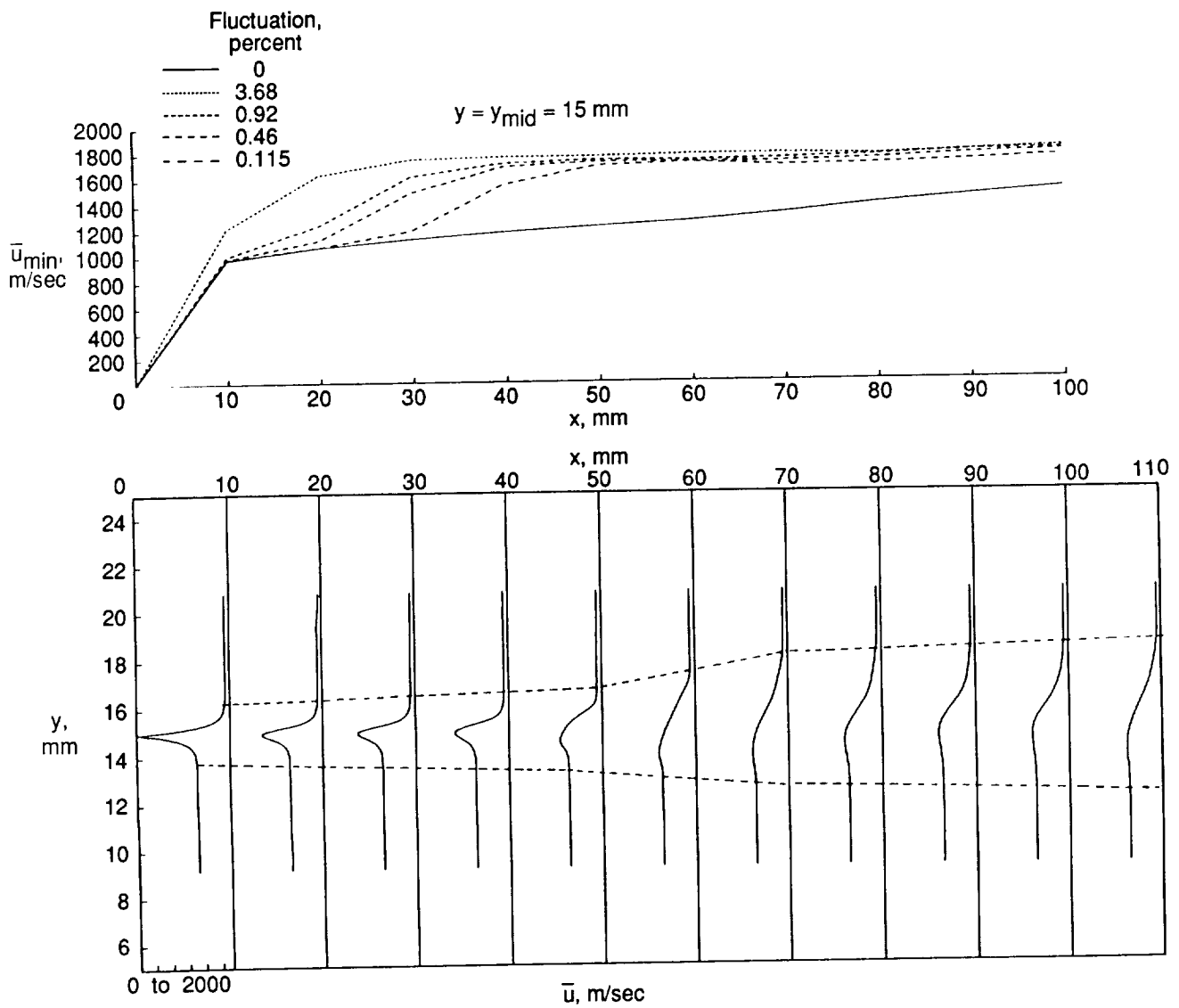
Figure 30. Minimum u versus x and mean u as a function of x and y at $M_c = 0.38$. Grid: 201 by 101; domain: 100 mm by 30 mm; initial profile: boundary layer.
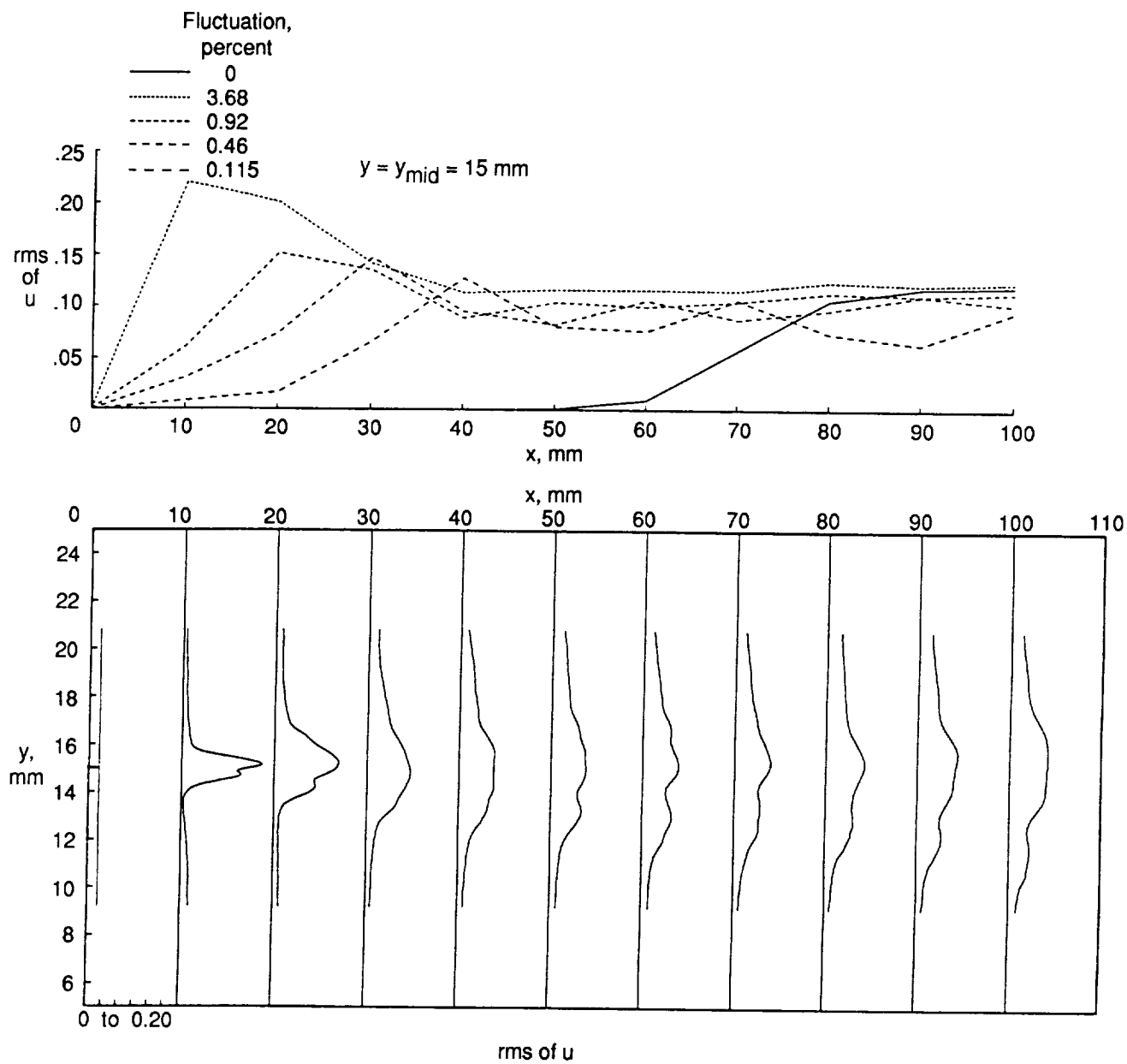
Figure 31. Distribution of rms of u as a function of x and y at $M_c = 0.38$. Grid: 201 by 101; domain: 100 mm by 30 mm; initial profile: boundary layer.
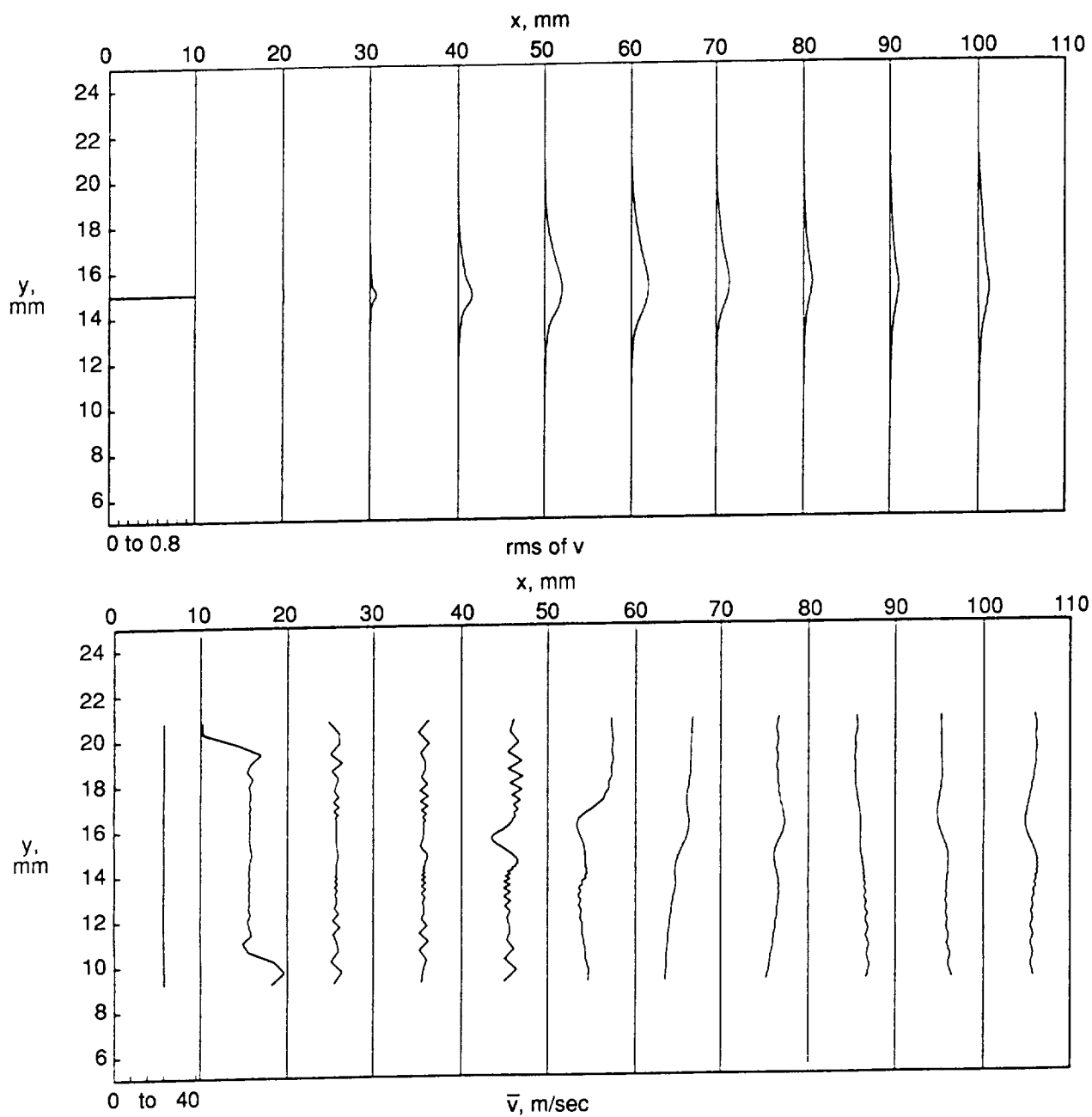
Figure 32. Mean and rms values of v as a function of x and y for 3.5 percent fluctuation.

Figure 33. Mean and rms values of ρ as a function of x and y for 0.115 percent fluctuation.

Figure 34. Mean and rms values of T as a function of x and y for 0.115 percent fluctuation.

Figure 35. Mean and rms values of H_2 mass fraction as a function of x and y for 0.115 percent fluctuation.
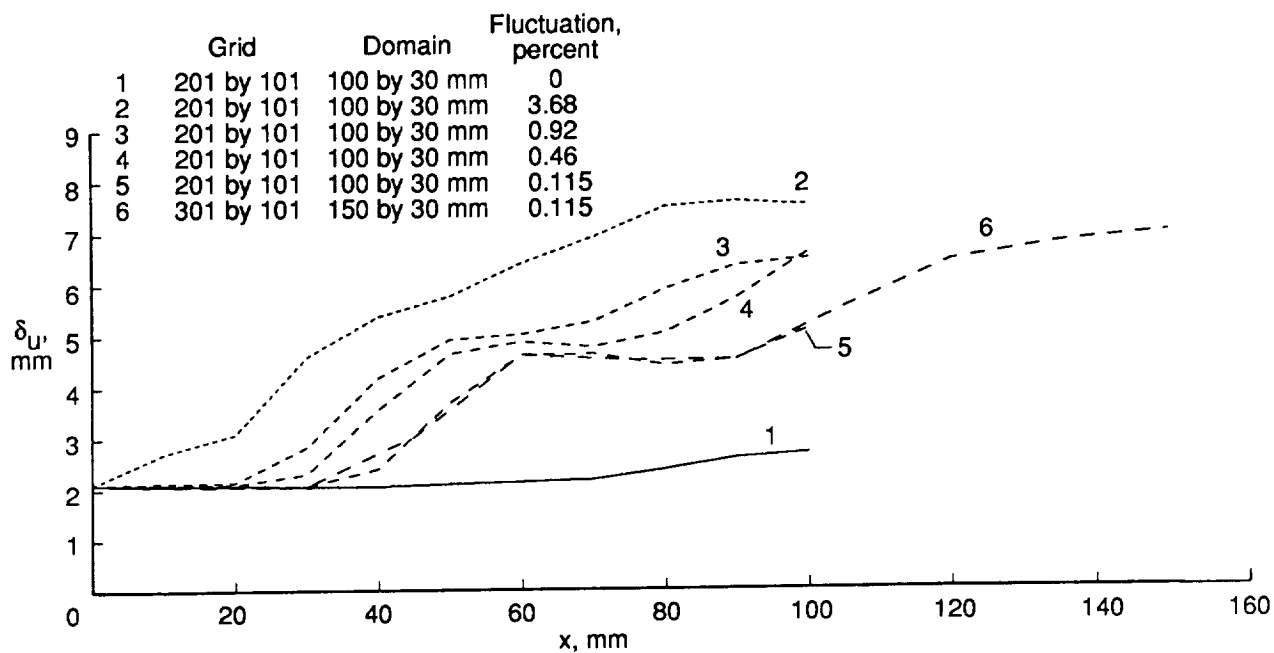
Figure 36. Plot of δ_u versus x for various fluctuation intensities at $M_c = 0.38$. Boundary-layer inflow profile.
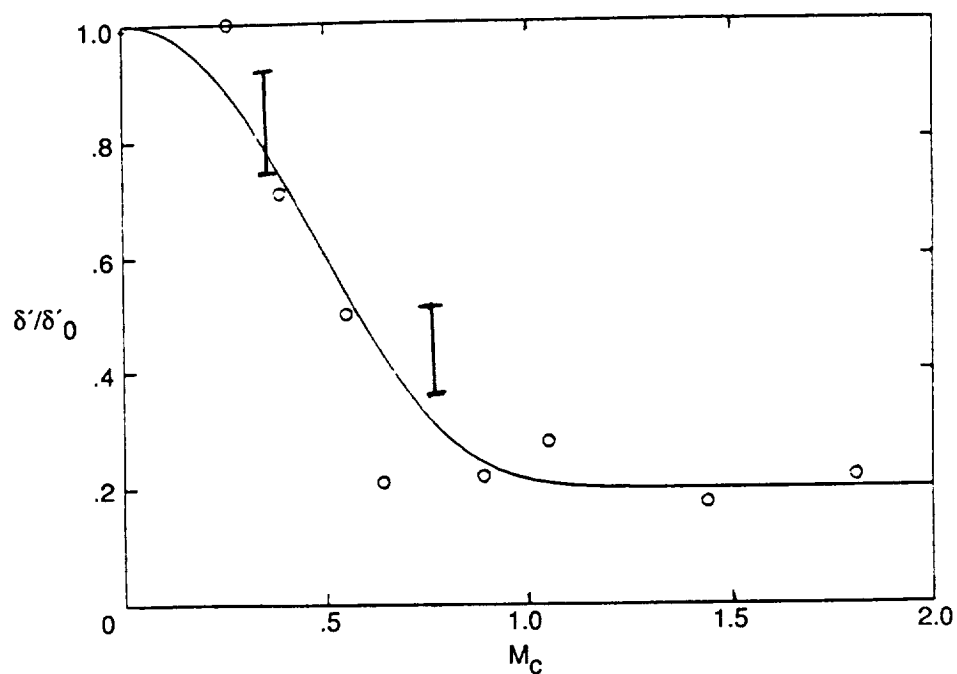
Figure 37. Growth-rate ratio as a function of convective Mach number and comparison with experimental data.
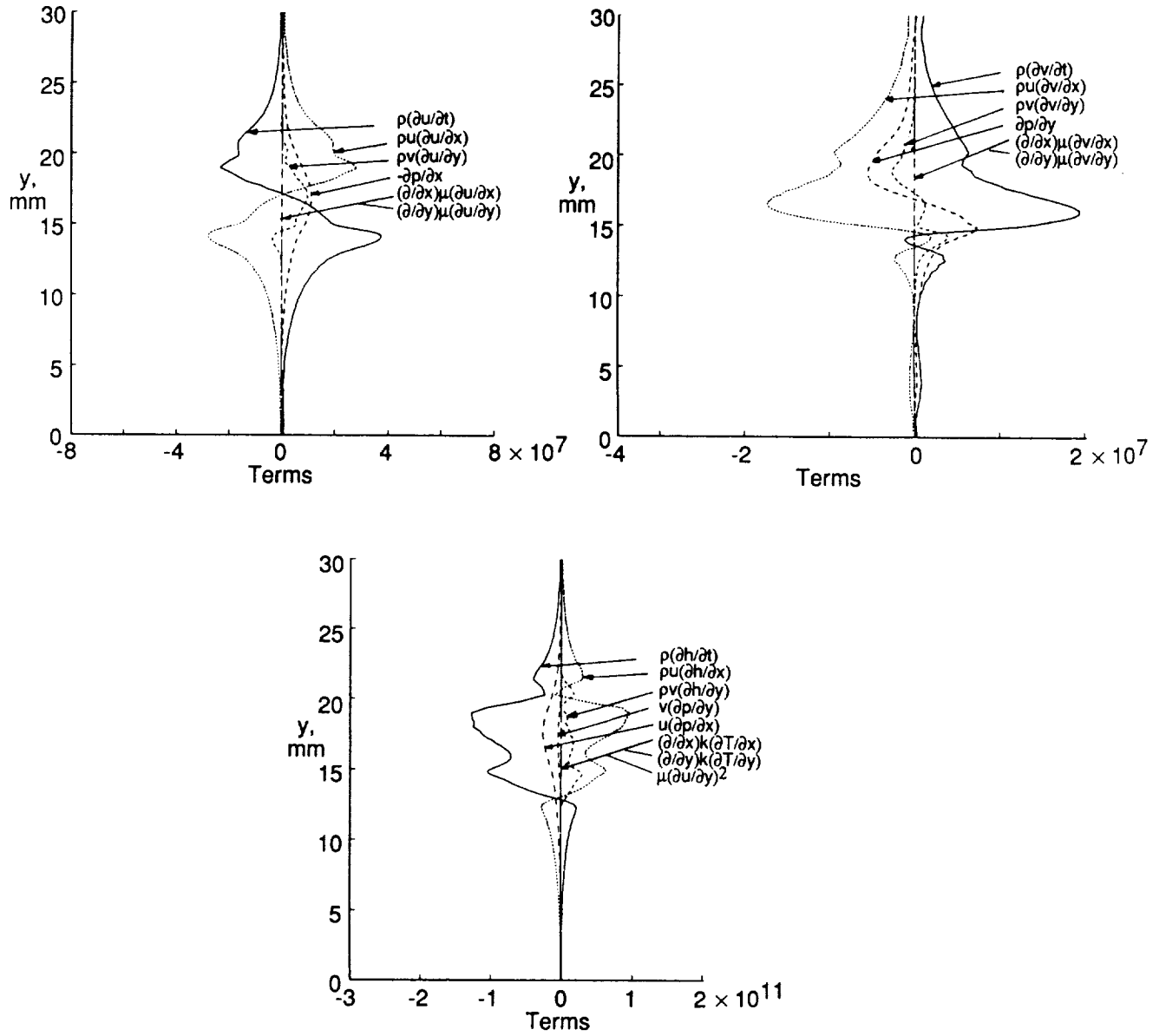
Figure 38. Magnitude of terms of u, v, and energy equations for boundary-layer case at $M_c = 0.38$. Domain: 150 mm by 30 mm; 0.115 percent fluctuation.
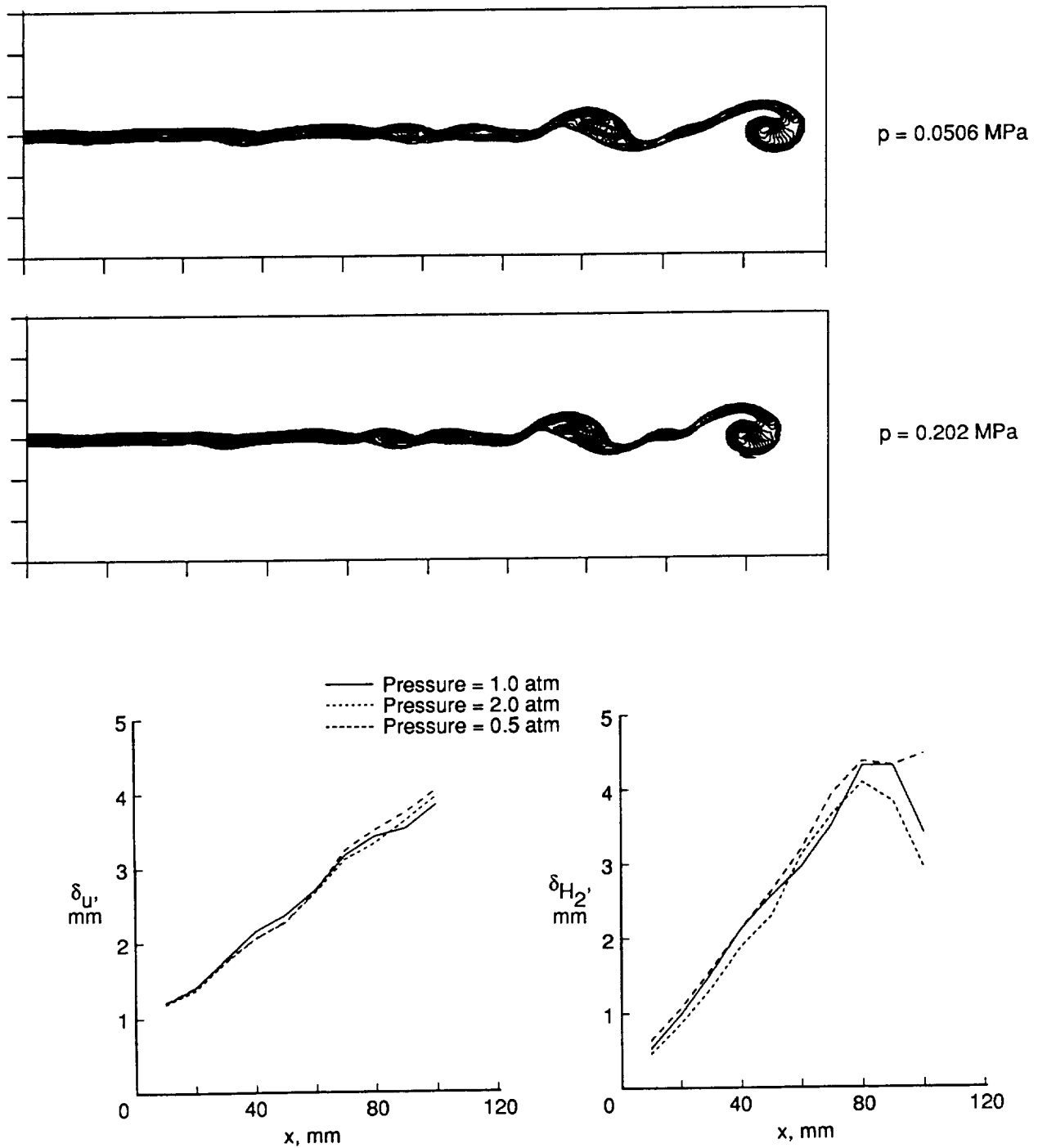
Figure 39. Vorticity contours and growth of shear layer at three pressures and $M_c = 0.38$. Grid: 201 by 101; domain: 100 mm by 30 mm.
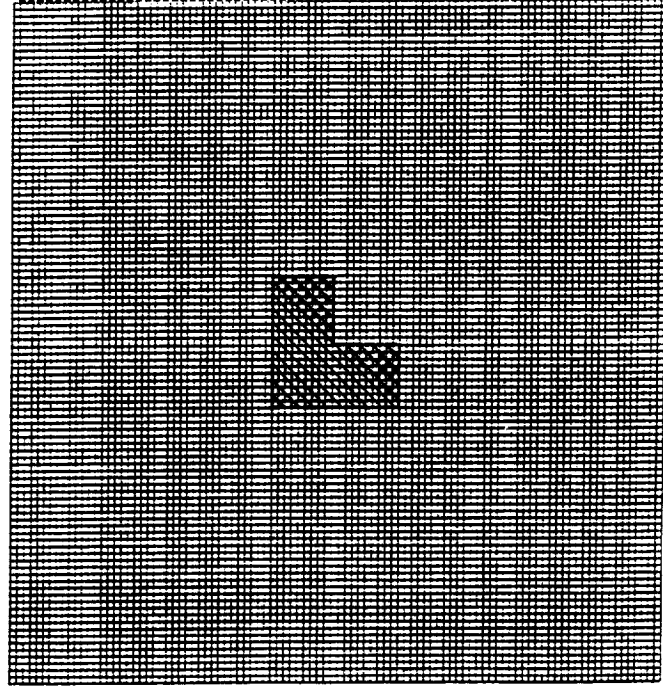
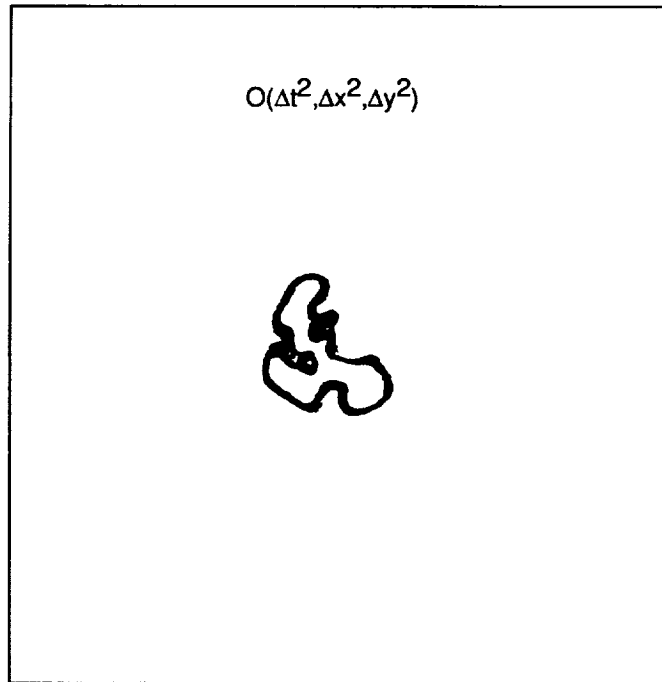Figure 40. Initial distribution for "color" problem, superimposed on grid used in study.

$$O(\Delta t^2, \Delta x^2, \Delta y^2)$$

Figure 41. Rotation of initial distribution with MacCormack (ref. 25) algorithm. Accuracy of method is second-order in time and space.
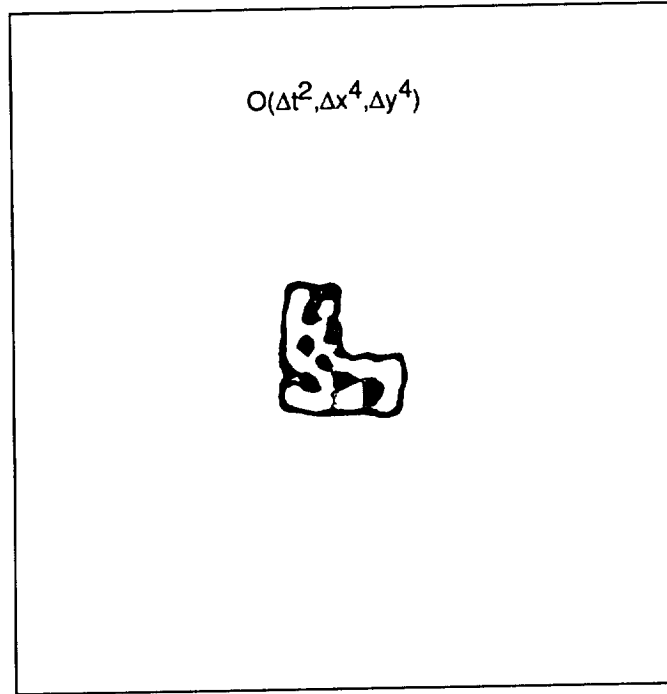
$O(\Delta t^2, \Delta x^4, \Delta y^4)$

Figure 42. Rotation of initial distribution with Gottlieb-Turkel (ref. 22) algorithm. Accuracy of method is second-order in time and fourth-order in space.

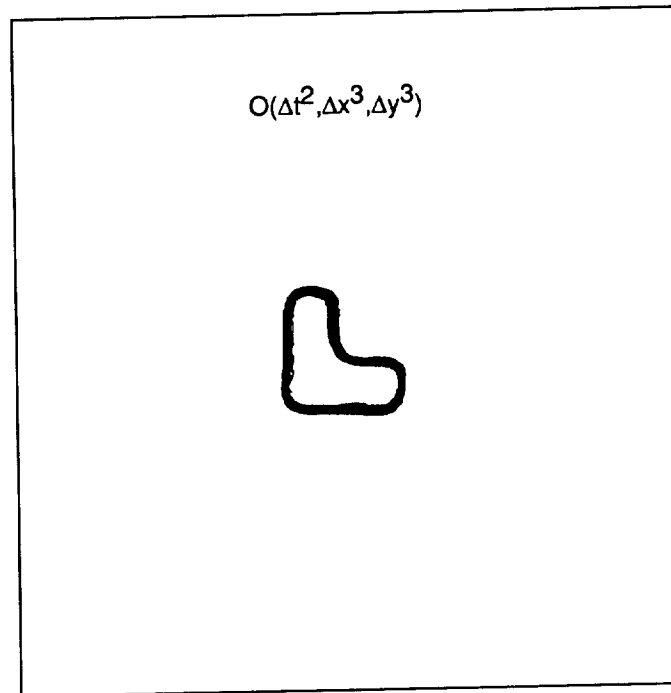$O(\Delta t^2, \Delta x^3, \Delta y^3)$

Figure 43. Rotation of initial distribution with third-order, upwind-biased algorithm. Accuracy of method is second-order in time and third-order in space.
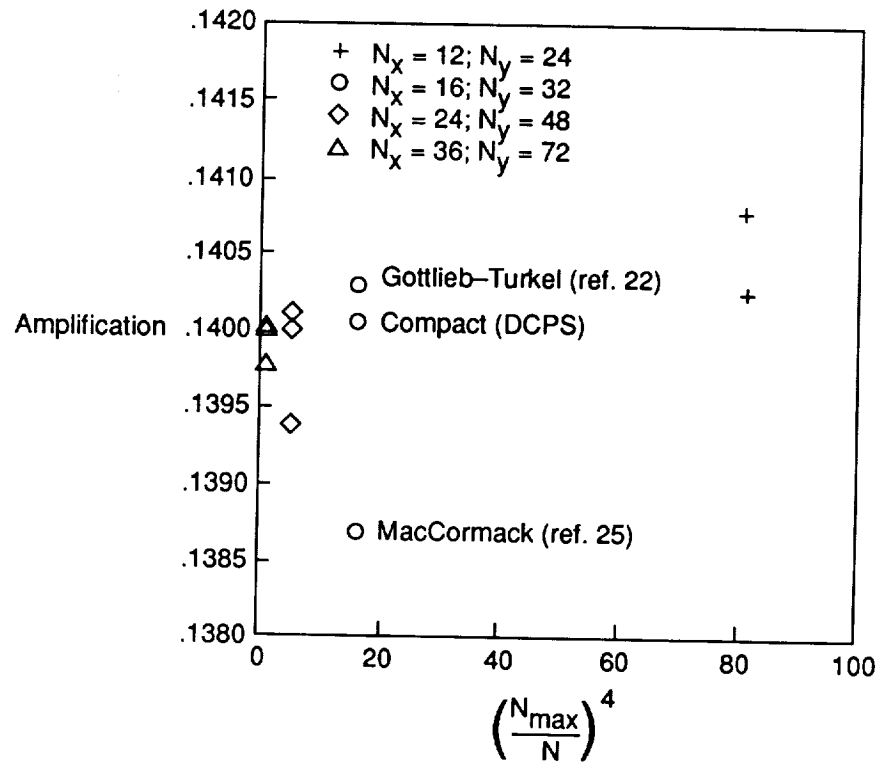
Figure 44. Comparison of higher order Gottlieb-Turkel and DCPS schemes with second-order MacCormack scheme. N_x is streamwise grid density: N_y is cross-section grid density.

REPORT DOCUMENTATION PAGE

Public reporting burden for this collection of information is estimated to average 1 hour per response, including the time for reviewing instructions, searching existing data sources, gathering and maintaining the data needed, and completing and reviewing the collection of information. Send comments regarding this burden estimate or any other aspect of this collection of information, including suggestions for reducing this burden, to Washington Headquarters Services, Directorate for Information Operations and Reports, 1215 Jefferson Davis Highway, Suite 1204, Arlington, VA 22202-4302, and to the Office of Management and Budget, Paperwork Reduction Project (0704-0188), Washington, DC 20503.

1. AGENCY USE ONLY *(Leave blank)*	2. REPORT DATE	3. REPORT TYPE AND DATES COVERED
	July 1992	Technical Paper

4. TITLE AND SUBTITLE
Direct Simulation of High-Speed Mixing Layers

5. FUNDING NUMBERS
WU 505-62-40-06

6. AUTHOR(S)
H. S. Mukunda, B. Sekar, M. H. Carpenter, J. Philip Drummond, and Ajay Kumar

7. PERFORMING ORGANIZATION NAME(S) AND ADDRESS(ES)
NASA Langley Research Center
Hampton, VA 23665-5225

8. PERFORMING ORGANIZATION REPORT NUMBER
L-16929

9. SPONSORING/MONITORING AGENCY NAME(S) AND ADDRESS(ES)
National Aeronautics and Space Administration
Washington, DC 20546-0001

10. SPONSORING/MONITORING AGENCY REPORT NUMBER
NASA TP-3186

11. SUPPLEMENTARY NOTES
Mukunda: NRC-NASA Resident Research Associate, now at Indian Institute of Science, Bangalore, India; Sekar: General Electric Research Center, Cincinnati, OH; Carpenter, Drummond, and Kumar: Langley Research Center, Hampton, VA.

12a. DISTRIBUTION/AVAILABILITY STATEMENT

Unclassified–Unlimited

Subject Category 02

12b. DISTRIBUTION CODE

13. ABSTRACT *(Maximum 200 words)*
A computational study of a nonreacting high-speed mixing layer is performed. A higher order algorithm with sufficient grid points is used to resolve all relevant scales. In all cases, a temporal free-stream disturbance is introduced. The resulting flow is time-sampled to generate a statistical cross section of the flow properties. The studies are conducted at two convective Mach numbers, three free-stream turbulence intensities, three Reynolds numbers, and two types of initial profiles—hyperbolic tangent (tanh) and boundary layer. The boundary-layer profile leads to more realistic predictions of the transition processes. The predicted transition Reynolds number of 0.18×10^6 compares well with experimental data. Normalized vortex spacings for the boundary-layer case are about 3.5 and compare favorably with the 1.5 to 2.5 found in experimental measurements. The tanh profile produces spacings of about 10. The growth rate of the layer is shown to be moderately affected by the initial disturbance field, but comparison with the experimental data of Papamoschou shows moderate agreement. For the boundary-layer case, it is shown that noise at the Strouhal number of 0.007 is selectively amplified and shows little Reynolds number dependence.

14. SUBJECT TERMS
High-speed mixing-layer transition; High-order finite difference; Shear layer

15. NUMBER OF PAGES
61

16. PRICE CODE
A04

17. SECURITY CLASSIFICATION OF REPORT	18. SECURITY CLASSIFICATION OF THIS PAGE	19. SECURITY CLASSIFICATION OF ABSTRACT	20. LIMITATION OF ABSTRACT
Unclassified	Unclassified		

National Aeronautics and
Space Administration
Code JTT
Washington, D.C.
20546-0001

NASA